Expanding the Bioanalytical Toolbox for Cell Signaling and the Environment

Tammi L. van Neel

A dissertation
submitted in partial fulfillment of the
requirements for the degree of

Doctor of Philosophy

University of Washington

2023

Reading Committee:
Ashleigh B. Theberge, Chair
Robert E. Synovec
Dustin J. Maly

Program Authorized to Offer Degree:
Chemistry

University of Washington

Abstract

Expanding the Bioanalytical Toolbox for Cell Signaling and the Environment

Tammi L. van Neel

Chair of the Supervisory Committee:
Ashleigh Theberge, Ph.D.
Department of Chemistry

This dissertation discusses the development and validation of new methodologies and their applications in studying cell signaling to understand human health and environmental exposures. Chapter 1 details different signaling modes cells use to regulate biological processes. Additionally, Chapter 1 introduces key aspects of how researchers study intercellular signaling using a combination of cell culture set ups and analytical methodologies. Chapter 2 presents a new bead-based method for the capture of a cell-secreted signal in live cell cultures. Chapter 3 highlights the use of the newly developed bead-based method to monitor signal exchange between two different cell types. Chapter 4 introduces novel cell culture platforms and models to investigate cell signaling in biomimetic structures and segregated systems. Chapter 5 presents an innovative technology for capturing airborne particles using aqueous microdroplets to study environmental impacts on human health. In summary, the work presented in this dissertation demonstrates how aspects from different disciplines can be utilized to expand the bioanalytical toolbox in monitoring changes in cell signaling and provide greater insights into environmental impacts on human health.

TABLE OF CONTENTS

LIST OF FIGURES

Appendix Figures

LIST OF TABLES

ACKNOWLEDGEMENTS

The past six years at UW have been an incredible experience in large part to the community of peers, friends, family, mentors, and advisors that I have been surrounded by. Everyone tells you that graduate school is *hard*, but you still do not fully realize just *how hard* it is until you are in it. Just as it takes a village to raise a child, it takes a network of people near and far to nurture a curious student into a confident scientist.

To the Theberge/BCME lab members both past and present, it has been an honor to grow alongside every one of you. The support and encouragement I have felt from everyone has been tremendous. I'm thankful to have overlapped with so many wonderful people and to have learned from you all. Thank you for all the writing, presentation, and project feedback; scientific input when troubleshooting projects; and welcoming environment – you have made coming into lab everyday much more enjoyable. I also want to thank all my co-authors from lab, especially Sam Berry and Ulri Lee – co-leading projects with you both has taught me so much and been an overall joy. I have valued every friendship and relationship I've made while working here.

Tianzi, Jing, and Xiaojing, thank you for your patience with me during trainings, thoughtfulness with research project questions, and general kindness. Hannah and Maia, thank you for your trust in me to be your mentor on a project that had lofty ambitions – I have appreciated working with you both and could always count on you guys for a smile and laughs during long experimental days. Yun and Jian-Wei, thank you for your passion for doing excellent science, being incredible people to work with, and for all your guidance on navigating life and science post grad school. Sam and Dostie, thank you for being the best peer mentors I could have asked for – you made the start of graduate school less scary and taught me how to be a meticulous scientist and thinker while being extremely generous with your time always. – your friendships have meant so much to me over the years. Sam, thank you for reminding me to spend time smelling the roses outside at the fountain and for all the early morning office chats when no one else was in yet.

Dostie, thank you for all the emotional support and hugs you've given me over the years and reminding me it's okay to take a break when needed. Ulri, thank you for being my other half in science; thank you for pushing me to be and do better, teaching me how to be a creative problem solver, and for always being down to get more ear piercings with me – your friendship and trust has been one of the highlights of my grad school experience.

To Ashleigh, your mentorship, advocacy, support, and faith in me has been one of the most reaffirming experiences in my path as a scientist; it has been a privilege to have been mentored by you. Thank you for always being a safe space, both personally and professionally, and for being an extraordinary example of what an excellent mentor, scientist, and leader looks like. I cannot fully (or adequately) express my gratitude to you other than to simply say *thank you*. To Erwin, thank you for always challenging me to think creatively, your sense of humor, and encouraging me to rethink what's possible. You've shown me you can do great science without sacrificing fun or uniqueness.

To my mentors and communities outside of UW, your guidance and support has been appreciated. Dr. Mike Roper, thank you for your belief and trust in me as an undergrad in your lab – without having experienced research in your group, I don't know if I would've ended up pursing grad school. Dr. John Dorsey, without your encouragement I would definitely not have considered grad school as an option for myself. Thank you for cheering me on from afar and celebrating my successes with enthusiasm. Dr. Phil Floyd, thank you for telling me the things I didn't know I needed to hear, being generous with your time, and helping me figure out what I wanted to do long term – your mentorship has been incredibly impactful. Dr. Tam'ra-Kay (TK) Francis, thank you for being my biggest cheerleader, a fierce advocate, and always looking out for me – your passion for Black students in STEM has kept me dedicated to helping the next generation find their path and to encourage other Black girls that science is for them. Thank you also to the HHMI Gilliam Fellow community and to NOBCChE for providing spaces for minorities to thrive in science.

To all my friends outside of lab, thank you for reminding me that I am not *just* a grad student. To Jada and Danielle, my best buds and found family, thank you for keeping me sane, letting me visit you in New York when I needed to escape, all the laughs, and being my most trusted council – you guys keep me true to myself and I am so proud of the lives we are building. To Zach, thank you for being a true friend and someone I can call on a whim to commiserate with. To Dostie, Lizzy, Nick, Kelsey, Eedaan, Danika, and Sarah: thank you for adopting me into the coven with open arms, letting me crash trivia nights, and always being up for grabbing a drink or popping champagne. To Paige, I couldn't have asked for a better roommate turned friend to have started grad school with. Thank you for always being down to explore Seattle, drink cider and binge watch Law and Order SVU, Grey's Anatomy, or Gilmore Girls, supporting me in more ways than one, and letting me share Angel with you; I'm so proud of you and everything you've accomplished, and I can't wait to make even more memories to cherish with you on the East Coast. To all the furry friends—Angel, Gemini, Lady Gray, Theadosia, and Buffy—thank you for letting me cuddle and pet you on the bad days. To Angel especially, your derpy face was such a joy to come home to – rest in peace little bud.

To my family, thank you for keeping me grounded and recharging my batteries when I was feeling down – I love you all. To my parents who have raised me to face all of life's challenges with grace and strength. You have always been there to provide me with wisdom and guidance when I felt uncertain and have shown me unconditional love throughout my life and academic pursuits. Thank you for reminding me to laugh, enjoy life whenever possible, and giving me a place to come home to whenever I needed. To my brothers, Carlo and Dillon, thank you for keeping me humble, giving me a good laugh, and always telling me the truth – I'm so proud of you both for following your passions. To my noodle, Alex, thank you providing me with constant love, an endless supply of laughs, and being my biggest cheerleader; I have loved the life we started building together in Seattle and I can't wait to see what the future holds for us.

DEDICATION

Aan my familie, dankie vir al die liefde en ondersteuning terwyl ek my drome gevolg het

&

to all the Black girls who love science but never felt like they belong, ***you do****.*

EPIGRAPH

It always seems impossible until it's done.

- Nelson Mandela

Chapter 1 | Introduction

1.1 Types of cellular signaling

Our bodies contain a multitude of different cell types which are the building blocks for organs, blood vessels, bones, and other components. The exchange of signals—whether mechanical, electrical, chemical, or some combination—are how cells communicate with one another; this communication is known as cell-cell signaling.[1] This dissertation focuses only on chemical cell signaling in which cytokines, chemokines, or growth factors are exchanged. Signals secreted and exchanged by cells are used to orchestrate complicated biological functions such as organ development, disease progression, homeostasis maintenance, or immune response. Cell signaling is vital to the proper function of organisms, however when signaling is not well regulated or dysregulated, harmful outcomes can occur. For example, interleukin 6 (IL-6) is a potent cytokine secreted by activated immune cells and stromal cells in response to infections or injury as part of the host defense system.[2,3] When IL-6 secretion is controlled and well-regulated it serves to swiftly contain the infection or injury site by recruiting additional immune cells to the area to resolve the problem. Once appropriate action has been taken cells typically stop the production and release of IL-6. In some cases, IL-6 production becomes dysregulated which can cause chronic inflammation and autoimmunity.[2,3]

Within chemical cell signaling, there are four categories – direct signaling across gap junctions, autocrine signaling, endocrine signaling, and paracrine signaling. Gap junctions are intercellular channel connections formed between two neighboring cells which enables direct signaling of small molecules such as Ca^{2+} ions.[4–6] In autocrine signaling a cell secretes a molecule into the surrounding environment that also binds to receptors on the same cell, effectively signaling to itself.[6] Endocrine signaling involves endocrine cells secreting a hormone molecule which travels a large distance—usually through the circulatory system—to target cells in different areas of the body.[6] Last, paracrine signaling is when a cell secretes a molecule and effects

neighboring cells in a localized manner.[6] All four of these signaling modes control cellular behavior and response, however this dissertation will focus on the role of paracrine signaling in cellular communication.

The time a signaling molecule spends in an environment informs the speed of a cellular response. Endocrine signaling is relatively slow because signals have to travel a large distance; this also means they tend to be less prone to degradation and causes the effects of the signal to last long (e.g., seconds to hours). For example, oxytocin is a hormone produced during reproductive processes like labor and delivery to stimulate uterine contractions which can take up to 48 hours to act.[7,8] In comparison, direct signaling across gap junctions and autocrine signaling occurs quickly and has immediate effects. Similarly, the effects of paracrine signaling are fast (e.g., minutes) as signals target adjacent cells.[9,10] Paracrine signals often do not last long in the surrounding microenvironment because once secreted from the cell, the signals are often immediately used and thereby removed by a neighbor cell, degraded by an enzyme in the area, or converted into a different form within milliseconds.[9]

1.2 Tools and methods for studying cell signaling

Studying cell communication via chemical cell signals has been an active area of research for decades. Many analytical methodologies have been developed to detect and quantify cell signals in order to understand how healthy states of cell behavior and function are altered during disease states. Being able to determine what signals are responsible for changing cell behavior during different stages of disease progression allows for more informed and effective drug treatments to be developed. Additionally, understanding the signals cells use during specific events helps provide insight into unlocking key aspects of biological processes.

Which analytical method one chooses to use depends on many factors including the type of sample or biological matrix, sample volume available, and the analyte(s) of interest. Native biological samples (sweat, blood, urine, etc.) are messy and contain high abundance proteins that

often mask analytes of interest. Sample clean-up/preparation protocols (e.g., liquid-liquid extraction, protein precipitation, and solid-phase extraction) can be employed prior to analysis to improve sensitivity, but they are often laborious.[11] Another important consideration is the type of information one hopes to obtain. For example, monitoring a dynamic process in which analyte concentration is constantly changing will require the ability to detect signals in real-time. A microfluidic device is one solution as these devices can incorporate sample processing steps and detection steps in the same platform.[12,13] If however the goal is to glean more insight into signaling networks, being able to measure multiple analytes in a sample would be key; a method where multiplexing is possible—such as an immunoassay—might be used instead of a microfluidic device.[14] Finally, another important deciding factor is the sensitivity and selectivity of the method needed. Low abundance analytes can often be measured using sensitive readouts like electrochemical or fluorescence detection while selectivity is often improved by using specific, targeting conjugates such as antibodies or aptamers.[14]

One common method for quantifying cell signals in a cell culture is to analyze the media cells are cultured in (i.e., conditioned media) using liquid chromatography coupled to mass spectrometry (LC-MS). Chemical signals in a liquid sample are first separated in a chromatographic column based on chemical or physical properties; after separation is done, the liquid sample is then injected and ionized into a mass spectrometer where ions are separated and subsequently detected based on their mass-to-charge ratio and unique fragmentation pattern. This analytical approach is both qualitative and quantitative making it an incredibly useful tool in providing information on the full secretory profile—or secretome—of a cell culture.[15] It is also used widely in many areas including pharmaceuticals, toxicology, food and environment applications, and clinical research. While LC-MS offers high resolving power for analyte separation and sensitivity for detecting low abundance analytes, there are some challenges that hinder its routine use.[16] Native biological samples and conditioned media often contain high salt concentrations and high-abundance proteins like albumin.[12,16] Both of these factors contribute to interference

and/or suppression of analytes of interest making it difficult to detect analytes without employing additional sample clean-up protocols prior to analysis.[14,17] Further, LC-MS method programs may need optimization for each analyte of interest for better detection which can be challenging.[17]

Specialized microfluidic platforms and immunosensors are gaining popularity as alternative methods for analyzing cell-secreted molecules. Microfluidic-based technology manipulates small volumes of fluid (<1 mL) in features and geometries where at least one dimension is on the micron scale.[18] This field in part emerged after the success of other microanalytical techniques, such as capillary electrophoresis, with the desire to apply the technology to other areas like chemistry and biology. One of the biggest technological advantages in using microfluidics to study cell signaling is the ability to measure molecules in real-time. Numerous works have demonstrated this capability by placing detection zones near cell culture areas[19], measuring analytes directly in micro-patterned cell culture regions via optical[20] or electrical systems[21], or miniaturization of immunoassay platforms.[22] While microfluidic technologies are powerful tools, their widespread use and adoption in laboratories has been slow due to the expertise needed for designing, fabricating, operating, and optimizing protocols before conducting experimental studies.

Arguably the most common approach for measuring cell signals is the use of an immunoassay platform. There are various configurations of immunoassays including enzyme-linked immunosorbent assays (ELISA), bead-based systems, and gel-based methods (e.g., gel electrophoresis), however in this dissertation I will focus predominantly on discussing ELISA and bead-based immunoassays. The basic principle of an immunoassay relies on the use of antibodies to detect and bind to a molecule in a biological sample (blood, saliva, conditioned media, etc.) with high specificity and sensitivity. Furthermore, immunoassays are capable of measuring analytes over a wide range of concentrations (pM-nM).

In ELISA platforms, antibodies are first immobilized on the bottom surface of a well within a well-plate; a liquid sample is then added (100-200 µL) to allow for any analyte present to interact

with and be captured by the immobilized antibodies for subsequent detection.[23] Due to their robustness, relatively low cost, and reliability, ELISA is regularly used in clinical laboratories for therapeutic drug monitoring.[24] While performing an ELISA assay can take hours, many samples (>96) can be analyzed and processed simultaneously. However, this method is limited by a few analytical problems including potentially high background noise due to interference with reagents needed for the assay and signal instability/drift from reactions that have not been fully stopped.[25]

Bead-based immunoassays work similarly to ELISA platforms with antibodies being immobilized on microparticles (5-7 μm outer diameter) instead of a well-plate surface. Some improvements to ELISA systems that bead-based systems offer is the use of smaller sample volume (25 μL) and reduced assay time, however it comes at a cost as bead-based immunoassays are generally more expensive. One attractive feature of bead-based and ELISA systems over methods previously mentioned is the ability to perform multiplex detection. This allows for the detection of several analytes from the same sample at the same time, helping to reduce the overall effort of measurement. For bead-based immunoassays specifically, this helps to reduce the overall cost as the same reagents can be used for every step of the assay.

1.3 Bioanalytical cell culture models and platforms

To probe cellular communication, *in vitro* cell culture or tissue culture methods are employed in which cells are grown in controlled environments outside of their native environments in the human body. Models such as these are used for several applications including investigating the pathobiology of diseases, assessing toxicity and efficacy of drugs or vaccines, understanding tissue or organ regeneration, and gaining insights into basic biology mechanisms.[26] Traditional two-dimensional (2D) cell culture of adherent cells is performed on flat surfaces commonly made of plastic or glass. 2D cell culture models are simple, low-cost, and highly replicable making them useful for large-scale drug absorption studies or functional biology studies.[27]

However, a limitation to 2D culture systems is that they often fail to represent the full complexity of *in vivo* cellular environments as they typically only include one cell type (i.e, monoculture).[27,28] Inserts for well plates enable the culture of more than one cell type (i.e., coculture or multiculture) facilitating cell-cell interactions which improves the biological relevance of these models.[29] For example, the Transwell® insert has been used to establish models for the blood-brain barrier[30], air-liquid interface of the lung[31], and cell invasion/migration assays[32]. Still, these models do not consider the three-dimensional (3D) nature of tissue structures in the human body.

Three-dimensional (3D) cell culture models incorporate a scaffold—made from a hydrogel or extracellular matrix components—for cells to either grow on or inside of. The scaffold provides support for creating tissue architectures that can be tuned based on the characteristics of the tissue or organ under study. For example, skin is a complex organ with distinct layers and organization of multiple cell subtypes where chemical, mechanical, and cell state cues all work together during development.[33] Without the use of a scaffold, this *in vitro* organoid model would have very little biological relevance as the architecture and structural nature of the organ would be lost. While 3D cell culture/organoid models are improving the way researchers study human development and other studies, they are often difficult to set up and have low reproducibility.[27] Regardless of any disadvantage, 2D and 3D cell culture models/platforms are invaluable tools for researchers to study a wide range of biological questions in many disciplines.

1.4 Cytokines and the inflammatory response

Chemical signals that specifically affect or influence cell communication in immune responses can generally be referred to as cytokines. They are small proteins that are secreted by cells and are often produced in cascades or networks (e.g., cytokine storm). Cytokines can act synergistically or antagonistically with the surrounding environment and their production is both

tightly regulated and transient. What physiological events occur depends largely on the concentration of a cytokine(s) at any given time since they are in a constant state of flux.[14]

From an analytical/measurement science perspective, trying to unravel how cytokines are being used in paracrine signaling events is challenging as many cytokines are short-lived in the microenvironment due to degradation or removal mechanisms. Furthermore, many cytokines exhibit pleiotropic behavior meaning one signal can act on multiple targets or induce several physiological pathways. This crosstalk only further complicates deciphering cell signaling activity for understanding biological processes.[14] For example, IL-6 induces the synthesis of proteins (e.g., collagen, fibrinogen, albumin), stimulates antibody production as part of the acquired immune response, and promotes growth of other cell types amongst additional biological activity.[2,34] The ability to measure and determine the primary reason a cytokine like IL-6 is present provides insight into biological function and aids in understanding disease progression.

In response to harmful stimuli like pathogens, damaged cells, or toxins, the body's immune system initiates the inflammatory response as a defense mechanism.[35] During an acute inflammatory response (e.g., paper cut, bug bite, minor burn), pro-inflammatory cytokines are released by immune cells into the surrounding tissue and the circulatory system to recruit immune cells and contain the injured area.[35] This initial response manifests as redness, swelling, itching, burning sensation, pain, or heat at the injury site. Following the resolution of the localized injury, anti-inflammatory cytokines are produced to terminate the process and help regulate the body's return to homeostasis.[36] In chronic inflammation, a slightly different pathway is triggered resulting in a sustained and low-grade inflammatory response.[37] As inflammation is well-studied and a common precursor in several diseases—including cardiovascular diseases, diabetes, cancer, asthma, and arthritis—it is well suited to serve as an excellent model process to use for validating new bioanalytical methods for use in studying complex cell signaling events.

1.5 Airborne pathogens and respiratory illnesses

Particles dispersed and transmitted through the air (e.g., particulate matter, volatile organic compounds, and bioaerosols) are ubiquitous and affect the health of a wide range of organisms.[38,39] Inhalation or ingestion of airborne particles can trigger a wide range of respiratory illnesses or exacerbate allergic reactions and is considered the most dominant transmission route of infection.[40] Exposure levels to particles change frequently because of fluctuations in both physical (e.g., size, shape, density of particles) and environmental (e.g., air currents, humidity, temperature) factors which change the formation, dispersion, and transport of airborne particles.[41,42] A variety of active and passive methods (filters, cyclones, impactors, etc.) have been developed to evaluate everyday exposures to airborne particles.[43,44] These methods are robust in capturing airborne particles but are not intended for measuring particle concentrations in the air. Similarly, methods for counting particles exist but fail to retain the particles in the system for further analysis.[45]

Airborne particles of biological origin are classified as bioaerosols. This class of airborne particles includes pet dander, fungi, bacteria, viruses, metabolic fragments (e.g., endotoxin, mycotoxin, secondary metabolites), pollen, etc.[46,47] The composition of bioaerosols present in the air largely depends on the aerosolization mechanism, biological source, and environmental conditions described earlier. Bioaerosols are also quite variable and have a wide range of characteristics; they can be pathogenic or non-pathogenic in addition to being alive or dead. Moreover, some bioaerosols like the listeria-causing bacteria *Listeria monocytogenes* are viable but not culturable.[48] Common activities generate bioaerosols including composting, recycling, coughing, sneezing, and cleaning, making their potential for inhalation extremely high.[46] In order to determine if a bioaerosol in common settings can cause damage to a host (i.e., virulent), capture and detection methods like infectivity assays or culture setups are employed. Therefore, it is important to maintain the viability of bioaerosols as much as possible.

Current air sampling methods often desiccate or dry bioaerosols, but the integration of bulk liquid or hydrogel components has helped mitigate this problem.[41,43,49] Additionally, these systems are not very portable which reduces their use in personal spaces. An alternative to bulk liquid is a spray of liquid, which has only been used in wet scrubbers for air pollution control; they capture particles and volatile organic compounds from effluent waste streams in production facilities. Wet scrubbers have been identified as one of the most effective methods for removing particles larger than 1 μm from the air, but wet scrubbers are large (ranging from the size of a small appliance to an industrial smokestack), susceptible to corrosion, and have high energy requirements.[39,50,51]

The recent increased interest in sampling the air for bioaerosols has been to perform viability studies and determine their potential to infect hosts and cause illness.[52] One of the most notable bioaerosols of recent time has been the SARS-CoV-2 virus which causes COVID-19. However, bioaerosols have been causing illness/disease for decades: influenza virus can result in the flu which affects millions every year; *Aspergillus* spores can lead to aspergillosis or contribute to allergies; respiratory syncytial virus is the most common cause of bronchiolitis or pneumonia; and *Mycobacterium tuberculosis* causes tuberculosis.[40,53] Additionally, non-communicable illnesses/diseases (e.g., asthma, chronic obstructive pulmonary disease, cystic fibrosis) are just as aggravated by bioaerosols as communicable illness/disease.[54] Further study is necessary to identify the true extent of interactions and risk between bioaerosols and illness/disease caused by their inhalation.

1.6 References

1. J. Feher, Cell Signaling, *Quant. Hum. Physiol.*, 2017, 205–217.
2. T. Tanaka, M. Narazaki and T. Kishimoto, IL-6 in Inflammation, Immunity, and Disease, *Cold Spring Harb. Perspect. Biol.*, 2014, **6**, 16295–16296.
3. E. Choy and S. Rose-John, Interleukin-6 as a multifunctional regulator: Inflammation, immune response, and fibrosis, *J. Scleroderma Relat. Disord.*, 2017, **2**, S1–S5.
4. 9.2: Signaling Molecules and Cellular Receptors - Forms of Signaling - Biology LibreTexts (accessed 5 May 2023).
5. D. Segretain and M. M. Falk, Regulation of connexin biosynthesis, assembly, gap junction

formation, and removal, *Biochim. Biophys. Acta - Biomembr.*, 2004, **1662**, 3–21.
6. G. M. Cooper, Signaling Molecules and Their Receptors.
7. OpenStaxCollege, An Overview of the Endocrine System (accessed 9 May 2023).
8. Oxytocin: What It Is, Function & Effects, (accessed 23 May 2023).
9. 9.2 – Signaling Pathways, Hormones and Endocrine System – Introductory Animal Physiology, (accessed 5 May 2023).
10. C. Liu, D. Chu, K. Kalantar-Zadeh, J. George, H. A. Young and G. Liu, Cytokines: From Clinical Significance to Quantification, *Adv. Sci.*, 2021, **8**, 2004433.
11. P. L. Kole, G. Venkatesh, J. Kotecha and R. Sheshala, Recent advances in sample preparation techniques for effective bioanalytical methods, *Biomed. Chromatogr.*, 2011, **25**, 199–217.
12. A. M. Schrell, N. Mukhitov, L. Yi, X. Wang and M. G. Roper, Microfluidic Devices for the Measurement of Cellular Secretion, *https://doi.org/10.1146/annurev-anchem-071114-040409*, 2016, **9**, 249–269.
13. X. Cui, Y. Liu, D. Hu, W. Qian, C. Tin, D. Sun, W. Chen and R. H. W. Lam, Lab on a Chip A fluorescent microbead-based microfluidic immunoassay chip for immune cell cytokine secretion quantification †, 2018, **18**, 522.
14. J. A. Stenken and A. J. Poschenrieder, Bioanalytical chemistry of cytokines – A review, *Anal. Chim. Acta*, 2015, **853**, 95–115.
15. R. Chaleckis, I. Meister, P. Zhang and C. E. Wheelock, Challenges, progress and promises of metabolite annotation for LC–MS-based metabolomics, *Curr. Opin. Biotechnol.*, 2019, **55**, 44–50.
16. P. Mukherjee and S. Mani, Methodologies to decipher the cell secretome, *Biochim. Biophys. Acta - Proteins Proteomics*, 2013, **1834**, 2226–2232.
17. J. J. Pitt, Principles and Applications of Liquid Chromatography-Mass Spectrometry in Clinical Biochemistry, *Clin. Biochem. Rev.*, 2009, **30**, 19.
18. G. M. Whitesides, The origins and the future of microfluidics, *Nat. 2006 4427101*, 2006, **442**, 368–373.
19. K. J. Son, P. Gheibi, G. Stybayeva, A. Rahimian and A. Revzin, Detecting cell-secreted growth factors in microfluidic devices using bead-based biosensors, *Microsystems Nanoeng.* 2017*, 31*, **3**, 1–9.
20. S. Ansaryan, Y. C. Liu, X. Li, A. M. Economou, C. S. Eberhardt, C. Jandus and H. Altug, High-throughput spatiotemporal monitoring of single-cell secretions via plasmonic microwell arrays, *Nat. Biomed. Eng. 2023*, 2023, 1–16.
21. K. R. Mitchell, J. E. Esene and A. T. Woolley, Advances in multiplex electrical and optical detection of biomarkers using microfluidic devices, *Anal. Bioanal. Chem.*, 2022, **414**, 167–180.
22. T. Wu, H. J. Womersley, J. R. Wang, J. Scolnick, & Lih and F. Cheow, Time-resolved assessment of single-cell protein secretion by sequencing, *Nat. Methods 2023 205*, 2023, **20**, 723–734.
23. E. L. Chiswick, E. Duffy, B. Japp and D. Remick, Detection and quantification of cytokines and other biomarkers, *Methods Mol. Biol.*, 2012, **844**, 15–30.
24. A. Dasgupta, Issues of Interferences in Therapeutic Drug Monitoring, *Biot. Other Interf. Immunoassays*, 2019, 99–112.
25. S. Sakamoto, W. Putalun, S. Vimolmangkang, W. Phoolcharoen, Y. Shoyama, H. Tanaka and S. Morimoto, Enzyme-linked immunosorbent assay for the quantitative/qualitative analysis of plant secondary metabolites, *J. Nat. Med.*, 2018, **72**, 32.
26. C. P. Segeritz and L. Vallier, Cell Culture: Growing Cells as Model Systems In Vitro, *Basic Sci. Methods Clin. Res.*, 2017, 151.
27. M. Kapałczyńska, T. Kolenda, W. Przybyła, M. Zajączkowska, A. Teresiak, V. Filas, M. Ibbs, R. Bliźniak, Ł. Łuczewski and K. Lamperska, 2D and 3D cell cultures - a comparison of

different types of cancer cell cultures, *Arch. Med. Sci.*, 2018, **14**, 910–919.
28. C. Jensen and Y. Teng, Is It Time to Start Transitioning From 2D to 3D Cell Culture?, *Front. Mol. Biosci.*, 2020, **7**, 33.
29. L. Goers, P. Freemont and K. M. Polizzi, Co-culture systems and technologies: taking synthetic biology to the next level, *J. R. Soc. Interface*, , DOI:10.1098/RSIF.2014.0065.
30. K. Hatherell, P. O. Couraud, I. A. Romero, B. Weksler and G. J. Pilkington, Development of a three-dimensional, all-human in vitro model of the blood–brain barrier using mono-, co-, and tri-cultivation Transwell models, *J. Neurosci. Methods*, 2011, **199**, 223–229.
31. T. Bluhmki, S. Bitzer, J. A. Gindele, E. Schruf, T. Kiechle, M. Webster, J. Schymeinsky, R. Ries, F. Gantner, D. Bischoff, J. Garnett and R. Heilker, Development of a miniaturized 96-Transwell air–liquid interface human small airway epithelial model, *Sci. Reports 2020 101*, 2020, **10**, 1–14.
32. J. Marshall, Transwell® Invasion Assays, *Methods Mol. Biol.*, 2011, **769**, 97–110.
33. H. Sun, Y. X. Zhang and Y. M. Li, Generation of Skin Organoids: Potential Opportunities and Challenges, *Front. Cell Dev. Biol.*, 2021, **9**, 3176.
34. T. Kishimoto, Interleukin-6: discovery of a pleiotropic cytokine, *Arthritis Res. Ther.*, 2006, **8**, S2.
35. L. Chen, H. Deng, H. Cui, J. Fang, Z. Zuo, J. Deng, Y. Li, X. Wang and L. Zhao, Inflammatory responses and inflammation-associated diseases in organs, *Oncotarget*, 2018, **9**, 7204.
36. J. M. Zhang and J. An, Cytokines, Inflammation and Pain, *Int. Anesthesiol. Clin.*, 2007, **45**, 27.
37. D. Furman, J. Campisi, E. Verdin, P. Carrera-Bastos, S. Targ, C. Franceschi, L. Ferrucci, D. W. Gilroy, A. Fasano, G. W. Miller, A. H. Miller, A. Mantovani, C. M. Weyand, N. Barzilai, J. J. Goronzy, T. A. Rando, R. B. Effros, A. Lucia, N. Kleinstreuer and G. M. Slavich, Chronic inflammation in the etiology of disease across the life span, *Nat. Med.*, 2019, **25**, 1822.
38. J. E. Thompson, Airborne Particulate Matter: Human Exposure and Health Effects, *J. Occup. Environ. Med.*, 2018, **60**, 392–423.
39. H. T. Kim, C. H. Jung, S. N. Oh and K. W. Lee, Particle Removal Efficiency of Gravitational Wet Scrubber Considering Diffusion, Interception, and Impaction, *https://home.liebertpub.com/ees*, 2004, **18**, 125–136.
40. C. C. Wang, K. A. Prather, J. Sznitman, J. L. Jimenez, S. S. Lakdawala, Z. Tufekci and L. C. Marr, Airborne transmission of respiratory viruses, *Science*, 2021, **373**, 981.
41. Y. Wu, A. Calis, Y. Luo, C. Chen, M. Lutton, Y. Rivenson, X. Lin, H. C. Koydemir, Y. Zhang, H. Wang, Z. Göröcs and A. Ozcan, Label-Free Bioaerosol Sensing Using Mobile Microscopy and Deep Learning, *ACS Photonics*, 2018, **5**, 4617–4627.
42. P. Srikanth, S. Sudharsanam and R. Steinberg, Bio-aerosols in indoor environment: composition, health effects and analysis, *Indian J. Med. Microbiol.*, 2008, **26**, 302–312.
43. C. W. Haig, W. G. Mackay, J. T. Walker and C. Williams, Bioaerosol sampling: sampling mechanisms, bioefficiency and field studies, *J. Hosp. Infect.*, 2016, **93**, 242–255.
44. J. Namieśnik, B. Zabiegała, A. Kot-Wasik, M. Partyka and A. Wasik, Passive sampling and/or extraction techniques in environmental analysis: a review, *Anal. Bioanal. Chem. 2004 3812*, 2004, **381**, 279–301.
45. S. Sousan, K. Koehler, L. Hallett and T. M. Peters, Evaluation of consumer monitors to measure particulate matter, *J. Aerosol Sci.*, 2017, **107**, 123.
46. E. Can-Güven, The current status and future needs of global bioaerosol research: a bibliometric analysis, *Int. J. Environ. Sci. Technol.*, 2022, **19**, 7857.
47. B. Ghosh, H. Lal and A. Srivastava, Review of bioaerosols in indoor environment with special reference to sampling, analysis and control mechanisms, *Environ. Int.*, 2015, **85**, 254.
48. N. E. Wideman, J. D. Oliver, P. G. Crandall and N. A. Jarvis, microorganisms Detection and Potential Virulence of Viable but Non-Culturable (VBNC) Listeria monocytogenes: A Review, DOI:10.3390/microorganisms9010194.

49. T. Han and G. Mainelis, Investigation of inherent and latent internal losses in liquid-based bioaerosol samplers, *J. Aerosol Sci.*, 2012, **45**, 58–68.
50. B. K. Lee, B. Raj Mohan, S. H. Byeon, K. S. Lim and E. P. Hong, Evaluating the performance of a turbulent wet scrubber for scrubbing particulate matter, *J. Air Waste Manag. Assoc.*, 2013, **63**, 499–506.
51. E. R. Altwicker, Wet Scrubbing, *Air Noise Pollut. Control*, 1979, 145–198.
52. M. Pan, J. A. Lednicky and C. Y. Wu, Collection, particle sizing and detection of airborne viruses, *J. Appl. Microbiol.*, 2019, **127**, 1596.
53. L. D. Stetzenbach, Airborne Infectious Microorganisms, *Encycl. Microbiol.*, 2009, 175.
54. S. D. Shukla, K. S. Vanka, A. Chavelier, M. D. Shastri, M. M. Tambuwala, H. A. Bakshi, K. Pabreja, M. Q. Mahmood and R. F. O'Toole, Chronic respiratory diseases: An introduction and need for novel drug delivery approaches, *Target. Chronic Inflamm. Lung Dis. Using Adv. Drug Deliv. Syst.*, 2020, 1.

Chapter 2│*Localized cell-surface sampling using dual-functionalized beads*

Reproduced in part from T.L. van Neel, S.B. Berry,* E. Berthier, and A.B. Theberge, "Localized cell-surface sampling of a secreted factor using cell-targeting beads." Analytical Chemistry,* **2020***, 92, 13634-13640.*
** Equal contribution*

TLvN collected all experimental data and conducted analysis; SBB executed preliminary work; TLvN and SBB designed experiments; TLvN, SBB, EB, and ABT interpreted results and conceptualized ideas; EB and ABT supervised work.

Abstract: Intercellular communication through the secretion of soluble factors plays a vital role in a wide range of biological processes (e.g., homeostasis, immune response), yet identification and quantification of many of these factors can be challenging due to their degradation or sequestration in cell culture media prior to analysis. Here, we present a customizable bead-based system capable of simultaneously binding to live cells (through antibody-mediated cell tethering) and capturing cell-secreted molecules. Our functionalized beads capture secreted molecules (e.g., hepatocyte growth factor secreted by fibroblasts) that are diminished when sampled via traditional supernatant analysis techniques ($p < 0.05$), effectively rescuing a reduced signal in the presence of neutralizing components in the cell culture media. Our system enables capture and analysis of molecules integral to chemical communication that would otherwise be markedly decreased prior to analysis.

2.1 Introduction

Chemical signaling events involving cell-secreted soluble factors (e.g., growth factors, cytokines) play a vital role in the induction of cellular functions and larger systematic biological processes including immune response, maintenance of homeostasis, and cellular differentiation.[1] However, detecting these molecules to decipher this complex signaling landscape is often hindered through the degradation, sequestration, or neutralization of important signaling molecules by extracellular factors such as enzymes or receptors.[2,3] The elimination of these short-lived soluble factors from a cellular microenvironment is an important component of chemical signaling processes, yet their absence leads to an incomplete snapshot of the signaling

microenvironment, as these transient factors cannot be easily analyzed. For example, the instability of eicosanoids (e.g., leukotrienes, prostaglandins)[4,5] or the degradation of cytokines by proteases[6–8] or poor storage conditions in clinical settings[9] makes their quantification challenging, hindering understanding of their role in biological processes such as inflammation and cancer. Identification and quantification of these key short-lived factors in the context of their localized signaling milieu can provide important insight into the signaling mechanisms that mediate biological processes within complex in vivo and in vitro systems.[10,11]

Various analytical and quantification methods, such as mass spectrometry and enzyme-linked immunosorbent assays (ELISA), have been developed that examine cell culture supernatants (i.e., conditioned media) or biological fluids (e.g., serum, urine) to provide important information on the makeup of cellular secretion profiles.[12] However, these methods often rely on sampling processes wherein important effector molecules may be degraded, sequestered, or converted on time scales faster than those required for sample preparation and analysis, resulting in a diminished signal; further, these readouts are typically used as end-point analyses that lack the temporal resolution provided by in situ methods and analyses.[13] More targeted approaches that integrate sample collection and readout, such as compartmentalized microfluidic cell culture platforms for in situ bead-based assays,[14,15] integrated microchip single-cell culture and analysis devices,[16] small-volume cell encapsulation and cell-sensor systems,[17–21] and enzyme-linked immunosorbent spot (ELISpot) assays,[22,23] address the limitations posed by traditional techniques and enable precise in situ analysis of culture systems at flexible time points throughout the experiment. These integrated culture and analysis platforms allow users to probe specific phenomena using systems with excellent spatial and temporal detection resolution, as well as single-cell resolution for secretome analysis. However, many of these methods require complex platforms and advanced fabrication facilities, decreasing their transferability, and rely on materials such as polydimethylsiloxane (PDMS), which has been shown to absorb small molecules.[24,25] Therefore, we sought to add to the analytical capabilities demonstrated in these advanced

technologies through the creation of a transferable and easily deployed system compatible with virtually all culture setups and sizes.

Bead-based technologies have been widely used for both the analysis of soluble factors within biological samples (e.g., bead-based ELISA) and to selectively capture and analyze cells from a mixed culture (e.g., magnetic bead-based cell isolation).[26–28] Additionally, the use of beads for targeted cellular secretome analysis has been applied in customized systems (often at a single-cell resolution) in applications including T cell secretion and function in cancer cells[15,21,29] and B cell secretion of antibodies for vaccination and immunity.[19,20] However, for larger scale applications (i.e., greater than single cell or microfluidic analyses), there lacks a broadly deployable bead-based technology to examine the production of transient soluble factors and the origin of those factors (**Figure 2.1**); additionally, to our knowledge, the ability to simultaneously capture these transient soluble factors and the cell itself with the same bead has not been demonstrated. Here, we introduce a customized, off-the-shelf bead-based approach to enable capture of short-lived or unavailable compounds from within existing cell culture systems that can then be coupled with downstream analytical methods such as immunoassays (**Figure 2.1**). Our platform consists of a dual-functionalized (DF) magnetic bead with two distinct antibodies, enabling simultaneous cell binding and signal capture (**Figure 2.1 bii**). Through cell tethering, our DF beads can target a specific cell type via cell-specific surface markers, as well as capture cell-secreted signals before they enter the bulk solution, where they may be sequestered or degraded. Here, we demonstrate that our DF beads capture a cell-secreted signal (hepatocyte growth factor, HGF) localized near the cell surface from live fibroblast cultures in the presence of a neutralization factor; in contrast, HGF levels are markedly diminished when collected through traditional supernatant analysis. We envision these dual-functionalized beads being employed in a wide range of monocultures and multi-cultures, enabling researchers to easily “listen” to cellular communication between different cell populations in situ without needing to modify their culture protocols or setup.

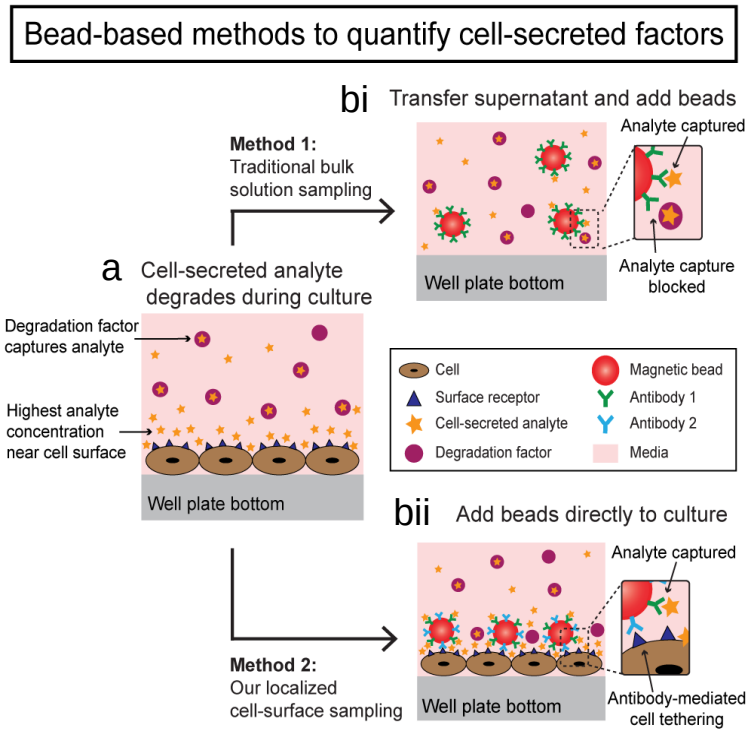

Figure 2.1. Bead-based approaches to quantifying cell-secreted factors. (a) Cells secrete soluble factors for communication, with the highest concentration immediately after secretion being near the cell surface. (bi) Traditional methods transfer the cell culture supernatant to another well plate and use beads for bulk solution analyte sampling, while (bii) our new approach utilizes cell-targeting beads in situ for analyte sampling.

2.2 Development and validation of beads

To probe the myriad of diverse environments where intercellular signaling occurs, an adaptable platform capable of being deployed across a wide range of signaling landscapes is required. Herein, we present a dual-functionalized (DF) bead system that binds to cells within a live in vitro cell culture system to analyze a secreted factor of interest in the presence and absence of a factor that may degrade, neutralize, or sequester the factor of interest. As a proof-of-concept model, we selected neonatal normal human dermal fibroblasts (NHDFn) expressing surface marker CD90 (**Figure A1**) and secreting hepatocyte growth factor (HGF) as our cellular and molecular target, respectively. HGF is a vital factor in multiple biological processes, including organ development, liver repair, and cancer progression, underscoring the importance of

fibroblast-driven chemical communication in a range of biological settings.[30] We designed and created dual-functionalized MagPlex beads covalently bound with antibodies against CD90 (anti-CD90) and HGF (anti-HGF) to target the secreted factor and cell surface marker, respectively (**Figures 2.2, 2.3,** and **Figure A2**).[31] To validate that the DF beads can successfully capture HGF at biologically relevant concentrations while simultaneously binding to the cell surface, we conducted two independent cell-binding and analyte capture assays (**Figures 2.2−2.4** and **Figures A3−A7**).

First, we performed a standard sandwich immunoassay using our DF beads (anti-CD90 and anti-HGF) and commercially available mono-functionalized (MF, anti-HGF only) beads with spiked HGF to compare HGF detection capabilities using the DF beads and MF beads when used according to traditional protocols (i.e., supernatant analysis). Both DF and MF beads successfully captured spiked HGF at a range of concentrations, enabling fitting to a five-parameter logistic (5PL) calibration curve as recommended by the manufacturer[31] and supporting the use of the DF beads as a tool for capturing and measuring secreted factors from cells (**Figure 2.2**). Differences in the curve shape is due to variation of kit performance; the kit performance variation was within accepted variability ranges based on the manufacturer's standards and protocols. We observed different limits of detection (LODs) between the two beads consistent with the different bead functionalization: DF beads, 104.25 pg/ mL; MF beads, 34.87 pg/mL (**Figure 2.2**). We also observed that DF beads had a 17%−36% lower total fluorescent signal than the MF beads (**Figure 2.2**). This is expected, as the number of available binding sites on the surface of the DF beads is less than the binding sites on the surface of the MF beads due to the presence of anti-CD90 antibodies, thereby decreasing the total number of fluorescent detection antibodies that will bind to HGF on the surface of the DF bead.

Second, we performed a cell-binding assay wherein we incubated DF beads with CD90-expressing NHDFn cells (**Figure 2.3**) and quantified their ability to remain bound to the cell surface after multiple wash steps (**Figures A3−A6** and **Table A1**). Beads were added directly to

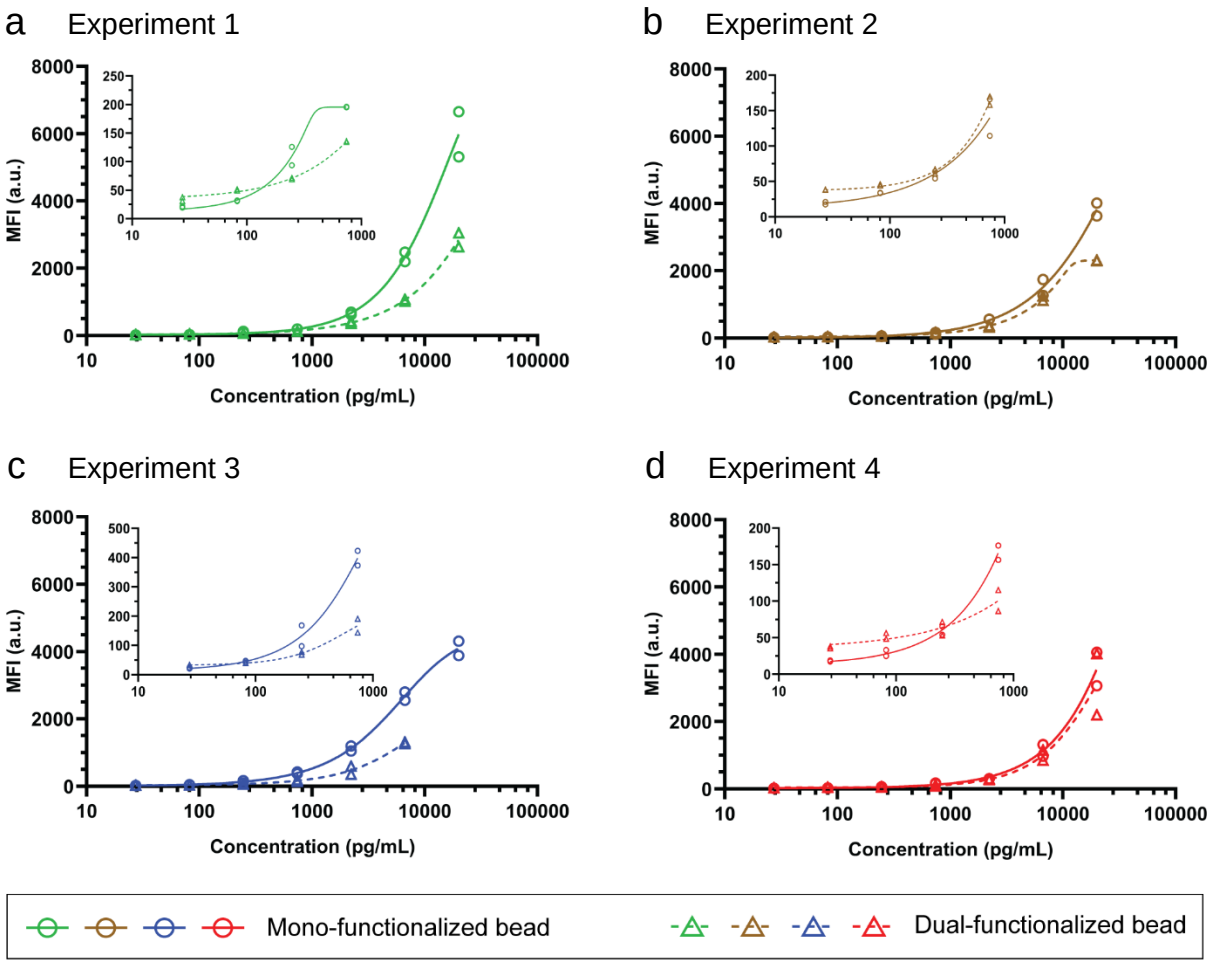

Figure 2.2. Calibration curves for mono-functionalized (MF) and dual-functionalized (DF) beads demonstrate ability of both beads to capture HGF. Per MagPlex manufacturer's recommendation, a five-parameter logistic fit was used to fit calibration curves and demonstrate the HGF-bead binding ability for each independent experiment (a, Experiment 1; b, Experiment 2; c, Experiment 3; d, Experiment 4) in duplicate (duplicates are shown as two plotted circles or triangles). Curves follow the expected trend based on manufacturer's technical notes. Decreased signal is observed for DF beads as the surface has roughly half the binding sites for HGF compared to MF beads. Insets are of first four points of the calibration curves. All curves are plotted on a logarithmic scale for visualization.

a 96-well plate culture of NHDFn cells and incubated for 2 h; after incubation, the culture was rinsed three times to remove unbound or nonspecifically bound beads. The remaining beads were then imaged and counted to quantify the ability of the DF beads to bind CD90+ cells (i.e., NHDFn) (**Figure 2.3, Figures A3−A7,** and **Table A1**). In addition to the fluorescence microscopy images shown in **Figure 2.3** and **Figure A3**, phase contrast images at 10X and 20X are provided in **Figures A4** and **A5.** After washing, 71% of the beads were retained, suggesting successful CD90-

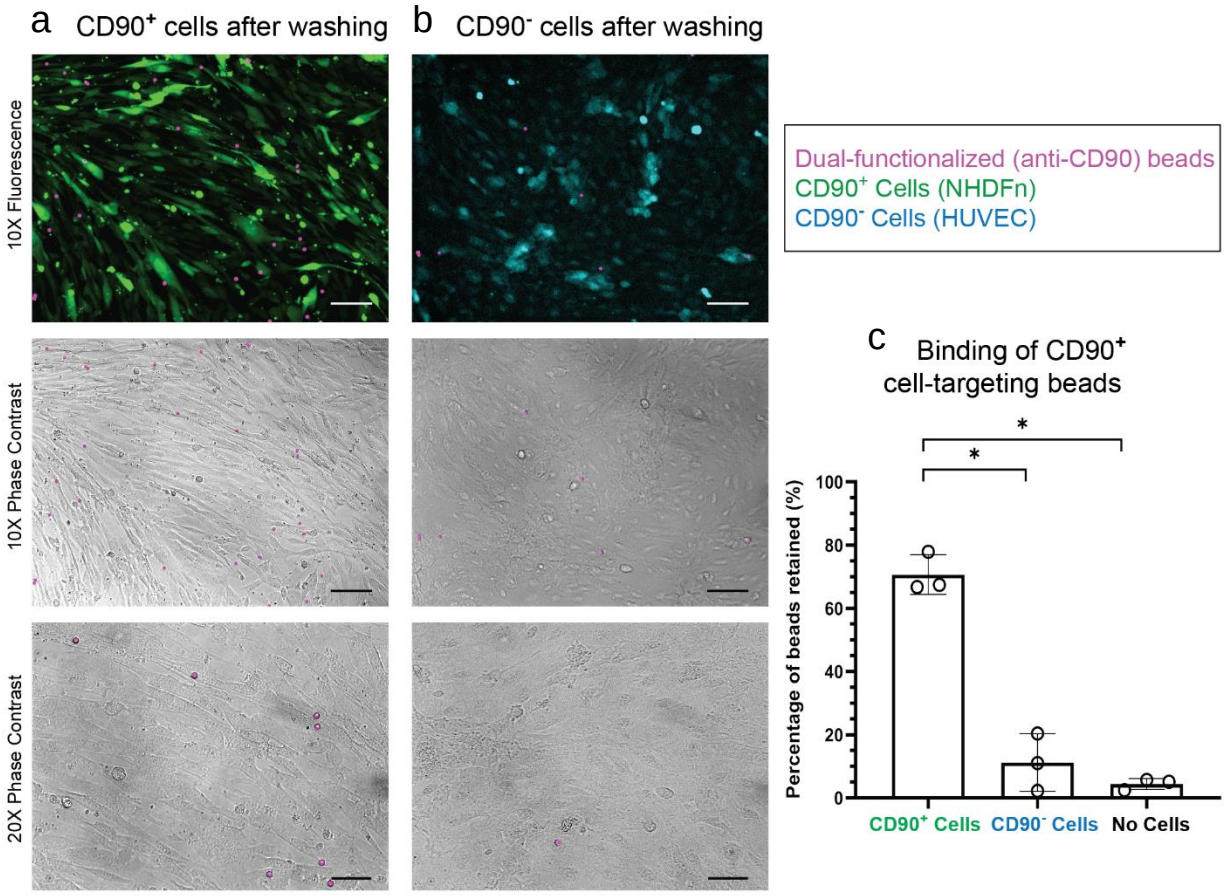

Figure 2.3. Dual-functionalized (DF) beads (functionalized with anti-CD90 and anti-HGF) target CD90+ cells (NHDFn). (a, b) Representative images of $CD90^+$ cells stained with CellTracker Green (green) and $CD90^-$ cells stained with CellTracker Blue (blue); cells were seeded at a density of 2.6×10^4 cells/mL, cultured for 3 days, and incubated with DF beads (pink) for 2 h. Images of wells were taken after washing to determine successful bead binding to the cell surface receptor CD90. (a) $CD90^+$ cells show an increased bead retention compared to (b) $CD90^-$ cells. (c) An average of 71% of DF beads were retained when incubated with CD90+ cells, significantly higher bead retention than for $CD90^-$ cells or no cells (empty well). Some non-specific binding was observed for beads placed in an empty well (<5% of beads retained). Bar graphs represent mean ± SD of n = 3 independent experiments. Brown-Forsynthe and Welch ANOVA tests were used followed by Dunnett's T3 test. * $p < 0.05$. 10X Scale bar = 100 µm. 20X Scale bar = 50 µm.

mediated cell binding (**Figure 2.3, Figure A3,** and **Table A1**). Further optimization of the bead functionalities (i.e., analyte capture and cell binding) can be accomplished by adjusting the ratio of antibodies on the surface, as well as through modulation of the specific biological system of interest to increase expression of cell-binding markers or secretion of soluble factors.

2.3 Application/proof-of-concept

To demonstrate one utility of our DF bead system, we created a model NHDFn culture system where we test the ability of the beads to capture a HGF signal before the signal is diminished in the bulk solution through neutralization with free anti-HGF antibodies; we hypothesized that this resuscitation of the HGF signal would be achieved through binding of the DF beads to the cell surface so that the beads can capture HGF as it is being secreted from the cell. To test this hypothesis, we cultured NHDFn cells with our DF beads and free anti-HGF antibodies so that secreted HGF could bind to either the beads (and be detected) or the free anti-HGF (and be neutralized); after a 2 h incubation, the supernatant was collected, and the culture was washed to remove any unbound beads or remaining free anti-HGF (**Figure 2.4**). The cells were then lysed to release the beads, which were subsequently washed and analyzed using standard Luminex assay protocols.[31] In parallel, we analyzed the HGF signal captured by MF beads according to the manufacturer's protocol (i.e., traditional cell culture supernatant sampling) (**Figure 2.4**). Following traditional cell culture supernatant sampling protocols, we observed a significant decrease ($p < 0.05$) in HGF quantification as a result of the presence of free anti-HGF in the cell culture media in comparison to controls without free anti-HGF (**Figure 2.4 bi**), suggesting that a sequestering factor (such as free anti-HGF) is able to reduce the secreted HGF available for quantification in bulk media. In contrast, under identical culture conditions, our dual-functionalized beads deployed on the cell surface restored the HGF signal to levels comparable to those found in the absence of free anti-HGF (**Figure 2.4 bii**), suggesting that the DF beads are able to capture the signal prior to its reduction in the bulk supernatant. The increased values observed in Experiment 4 are due to biological cell variability, which is expected in cell culture experiments. When examining the relative standard deviation, we observed an increased variability in the traditional supernatant sampling (8%−62%), while our localized cell-surface sampling method was consistently below 15% (**Table A2**).

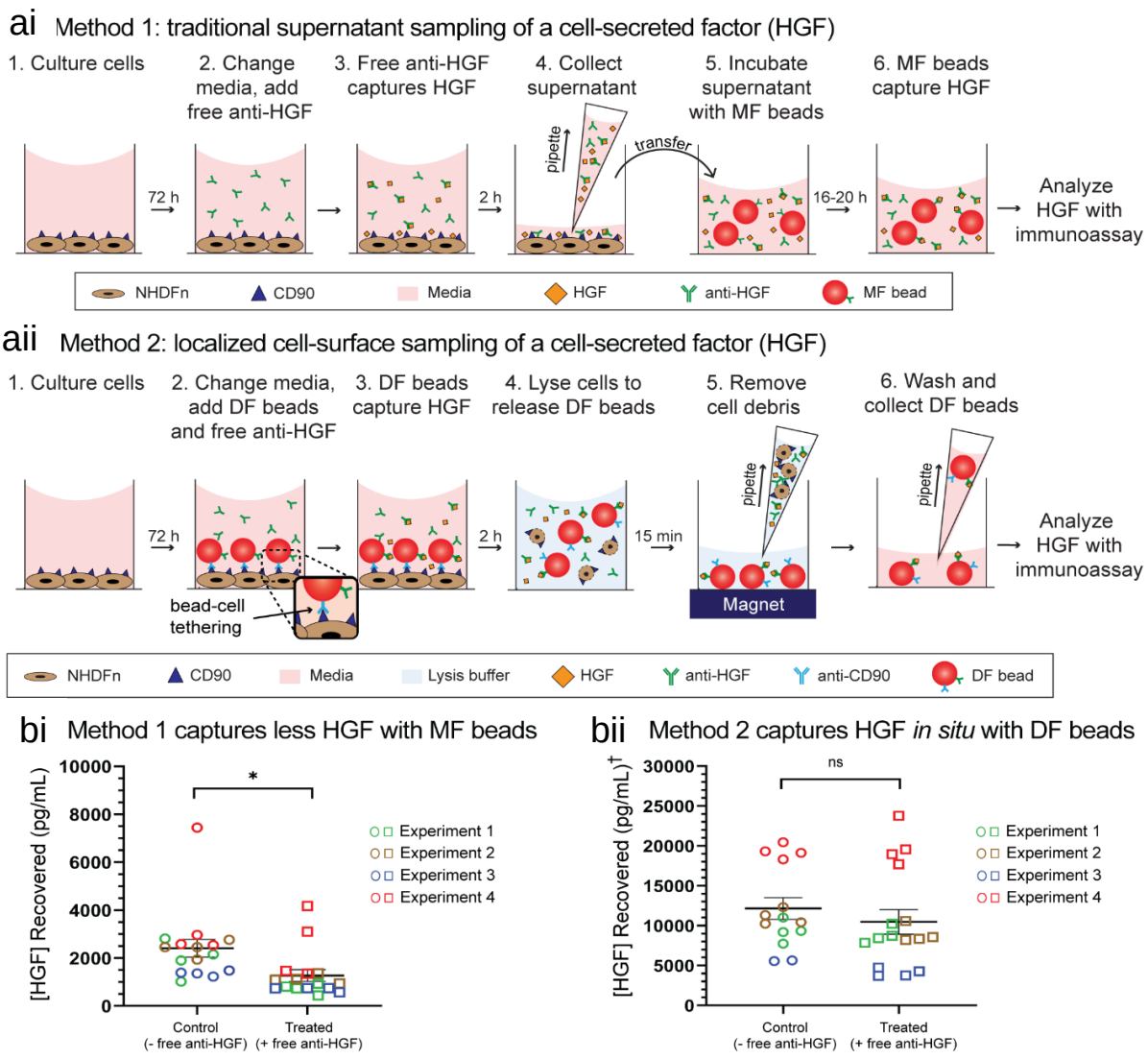

Figure 2.4. Localized cell-surface sampling recovers HGF signal in the presence of a neutralizing factor. Schematics showing workflow of (ai) traditional supernatant sampling and (aii) localized cell-surface sampling of a cell-secreted factor. Mono-functionalized (MF) beads (functionalized with anti-HGF) are used for supernatant sampling, while dual-functionalized (DF) beads (functionalized with anti-HGF and anti-CD90) are used for localized cell-surface sampling. (ai) MF beads are added to supernatant samples collected from cell cultures after a 2 h incubation. (aii) DF beads are added directly to cultures for a 2 h sampling period. (bi) Supernatant analysis shows a decrease in recovered HGF when cells are incubated with free anti-HGF, whereas (bii) localized cell-surface sampling with DF beads shows no change in recovered HGF since beads capture HGF before neutralization by free anti-HGF. Error bars are SEM. Experiments were performed in the absence (−) or presence (+) of free anti-HGF and are represented as circles or squares, respectively; each point represents a single culture well (in the case of supernatant sampling two technical replicates were performed on each well, and they are averaged). (bii, †: HGF recovered using DF beads is captured at the surface of the cell, rather than the bulk, leading to increased overall HGF capture. The absolute values in panel bi should not be directly compared to the absolute values in panel bii, but rather the trend within each graph between control and treated conditions.) Unpaired Student's t test. * p = 0.016; ns p = 0.428.

As a control, to verify that the proximity of the DF beads to the cell promotes improved HGF capture, and to eliminate any artifacts associated with cell-bead binding and the lysis step employed in our localized cell-surface sampling method, we cultured NHDFn cells in close proximity to (10 μm) and at a distance (1.3 mm) from the beads in the presence and absence of free anti-HGF using a Transwell® insert setup (**Figure A8**). The use of the Transwell® insert ensured that the DF beads remained segregated from the cells due to the difference in the membrane pore size and bead diameter (0.2 and 5.6 μm, respectively). We found that the beads captured increased levels of HGF (both in the presence and absence of free anti-HGF) when in close proximity to the cells when compared to at a distance. This finding supports that the increased signal capture capabilities of our localized cell-surface sampling method are due to the proximal location of the DF beads on the cell surface (**Figure 2.4** and **Figure A8**). While it is likely that MF beads would provide a similar signal if allowed to settle nonspecifically on the cell surface, the ability of the DF beads to specifically bind to cell types of interest enables beads to target the desired cell and ensure the cellular origin of the secreted signal (**Figure A7**). Further, to validate that the observed HGF signal in our localized cell-surface sampling method (**Figure 2.4 bii**) was not simply intracellular HGF released during the lysis steps, we sought to separately quantify HGF concentrations in samples containing the lysis buffer. Utilizing the DF beads, we quantified the concentration of HGF present in the cell lysate (cells had been rinsed to remove extracellular HGF prior to lysis) and observed significantly less HGF signals in cell lysate when compared to the signals captured from localized cell-surface sampling (**Figure A9**), indicating that the majority of the HGF captured using our localized cell-surface sampling method is secreted from the cell. Further, in future work, we will develop gentler methods to remove the bead from the cell surface without lysing the cell. In summary, our DF beads can selectively bind to the surface of a cell and capture signals directly secreted from the cell before the secreted factor is sequestered and lost in bulk solution.

2.4 Conclusion

In this work, we present a new bead-based system that enables in situ capture of a secreted molecule (HGF) in the presence of a known neutralization factor (free anti-HGF); through targeted cell tethering of DF beads, we can capture secreted HGF as it is released from the cell, rescuing a signal that is lost in traditional supernatant analysis due to HGF binding to free anti-HGF in the bulk solution (**Figure 2.4**). MagPlex beads were chosen to enable future development and multiplexing of different analytes and cell types, as they are commercially available and compatible with a wide range of antibodies, allowing easy adaptation of this technology without the need for specialized fabrication or experimental protocols. Further development of this platform will focus on selective bead detachment methods and optimizing antibody ratios to improve binding capabilities and permit continuation of cultures after bead detachment. Future application of this technology includes deploying this method in complex biological systems containing multiple cell types (e.g., mixed cocultures of mammalian cells, multi-kingdom culture containing microbial and mammalian cells, and ex vivo tissue slices) to demonstrate our method's potential to selectively target a specific cell type in a complex environment containing multiple cell types, as well as complex biological samples (e.g., blood), to capture short-lived factors for physiological analysis.

2.5 Materials and Methods

Reagents and Materials: Luminex kits (Product # HAGP1MAP-12K) containing wash buffer, assay buffer, secondary detection antibody, mono-functionalized beads, recombinant human hepatocyte growth factor (HGF), and streptavidin-R-phycoerythrin conjugate (SAPE) were purchased from EMD Millipore (Burlington, MA) and used for anti-HGF/HGF Assay experiments (details below). Clear tissue culture treated (TCT) 96-, 24-, and 12-well plates (Corning #3596, #3526, and #3515, respectively) and black TCT 96-well plates (Corning #3603) were purchased from Corning (Corning, NY). Falcon Transwell® 24-well plate inserts (Corning #353104) were

purchased from Fisher Scientific (Hampton, NH). Antibody coupling kits (Product #40-50016) were purchased from Luminex Corporation (Austin, TX).

Cell Culture: Normal Human Dermal Fibroblast neo-natal cells (NHDFn) (ATCC, Manassas, VA) were cultured, passaged, and seeded in fibroblast basal medium supplemented with a low-serum growth kit (ATCC, #PCS-201-030 and #PCS-201-041) (fibroblast media). 24 h after seeding cells in well plates or Transwell® inserts, media was replaced with Endothelial Cell Growth Medium-2 BulletKit (EGM-2) (Lonza, Basel, Switzerland) supplemented with 10% heat-inactivated (HI) fetal bovine serum (FBS) (see below); media was changed daily. NHDFn passage numbers ranged from 6-8 for experiments. Human Umbilical Vein Endothelial cells (HUVEC) (Lonza, Basel, Switzerland, #C2517A) were cultured, passaged, and seeded in EGM-2 media. HUVEC passage numbers ranged from 3-5 for experiments. FBS was heat-inactivated following the procedure provided by Serum Source International. Briefly, FBS was brought to room temperature and placed in a water bath heated to 56 °C for 30 min. HI-FBS was then cooled to room temperature before being stored at -80 °C until use.

CD90 Expression by Normal Human Dermal Fibroblast neo-natal Cells (NHDFn): Expression of CD90 by NHDFn cells was validated through standard immunocytochemistry techniques. NHDFn cells were cultured in a black TCT 96-well plate for 3 days; on Day 3 post seeding, cells were fixed for 10 min with 4% paraformaldehyde, permeabilized with 0.2% Triton X-100, and then blocked with 3% bovine serum albumin (BSA). After blocking, primary anti-CD90 monoclonal antibody (clone AF-9, Abcam, #ab23894) (1:50 dilution) was added and incubated overnight at 4 °C; goat anti-mouse secondary polyclonal antibody conjugated with Alexa Fluor-488 (1:200 dilution) (Jackson ImmunoResearch Laboratories Inc., #115-545-166) was then allowed to incubate for 1 h at room temperature. After washing, DAPI (ThermoFisher, #D1306) (1:200 dilution) was incubated for 5 mins at room temperature before washing and imaging (**Figure A1**). HUVECs were simultaneously cultured as described above to serve as a negative control. HUVECs were stained with CellTracker Blue (ThermoFisher, #C2110) for 1 h before seeding

according to the manufacturer's protocols. Fixing and staining protocols outlined above were followed before imaging (**Figure A1**).

Bead Functionalization: MagPlex microspheres (region 34) were purchased from Luminex Corp. and functionalized with anti-human hepatocyte growth factor (anti-HGF) monoclonal antibody [(clone 24516) (R&D Systems, Inc., Minneapolis, MN)] and anti-human cluster of differentiation 90 (anti-CD90) monoclonal antibody (clone AF-9) (Abcam, Cambridge, MA) according to the manufacturer's instructions (Luminex antibody coupling kit, #40-50016).[31] Briefly, carboxylated microspheres were first activated with 1-ethyl-3-[3-dimethylaminopropyl] carbodiimide hydrochloride (EDC) and sulfo-N-hydroxysulfosuccinimide (Sulfo-NHS). Once activated, anti-CD90 and anti-HGF antibodies were added at a 1:1 concentration-based ratio to covalently bind to the surface of the activated microspheres. Once coupled, microspheres were rinsed and stored in phosphate buffered saline (PBS) containing 1% bovine serum albumin (BSA) at 4 °C until use. Care was taken to protect the microspheres from light to prevent photobleaching during coupling. Microspheres were used as per the manufacturer's instructions and within 6 months of coupling. To validate successful coupling of the antibodies with the microspheres, we performed a secondary antibody labeling and subsequent analysis.[31] Briefly, phycoerythrin-conjugated rat anti-mouse IgG (clone M1-14D12) (ThermoFisher Scientific) was added to the microspheres at a range of concentrations (0.0625 µg/mL to 4 µg/mL), incubated, and analyzed to generate a calibration curve as per the manufacturer's instructions (**Figure A2**). Antibodies used for bead functionalization (anti-HGF and anti-CD90) were validated by manufacturers established quality assurance protocols (not specified).

Bead-Cell Binding Validation: To validate the bead-cell binding, NHDFn cells were passaged, incubated with CellTracker Green for 1 h at room temperature, washed with 1X PBS, and seeded in a black TCT 96-well plate at a density of 2.6×10^4 cells/mL and cultured for 3 days; cells were seeded in fibroblast media and replaced with EGM-2 media for the remainder of the experiment. As a negative control, HUVECs were passaged, incubated with CellTracker Blue for 1 h at room

temperature, washed with 1X PBS, and seeded at a density of $2.6x10^4$ cells/mL; cells were cultured for 3 days in EGM-2 media. Dual-functionalized (DF) beads (coupled with both anti-CD90 and anti-HGF antibodies) at a concentration of 50 beads/μL were added to the cultures on Day 3, post-seeding. An additional negative control was used in which different dual-functionalized beads [(coupled with both anti-CD64 (cluster of differentiation 64) and anti-MMP12 (matrix metallopeptidase 12) antibodies) (Abcam, #ab119843 and #ab52897, respectively)] were added to separate wells containing NHDFn cultured in the same manner as stated above. Plates were shaken at 100 rpm for 1 min then placed on a plate magnet (Stemcell Technologies, #18102) for 1 min; this was repeated twice more for a total of three rounds followed by a 2 h incubation. After incubation, wells were washed with EGM-2 media 3 times. Wells were imaged before washing wells and after washing wells (**Figure A3-A6**). To demonstrate cell-targeting ability, a device (Monorail2) was used to pattern NHDFn and HUVECs in separate regions of the well plate.[32] Full device operation and protocol is provided in Day and Nicholson et al.[32] Briefly, a Monorail2 device was placed into a 24-well plate and a 1.5 wt% low gelling temperature agarose pre-gel solution (Sigma-Aldrich, #39346-81-1) was flowed to create a hydrogel wall; gel was cooled at room temperature until solidified. 1X PBS was loaded into wells for 24 h before use in experiments. Prior to seeding, NHDFn were incubated with CellTracker green dye for 1 h at room temperature and HUVECs were incubated with CellTracker blue dye for 1 h at room temperature (following dilution instructions provided) and washed with 1X PBS. Both cell types were seeded at a density of $2.6x10^4$ cells/mL and cultured for 3 days in EGM-2 media. On Day 3 post-seeding, Monorail2 devices were removed and dual-functionalized beads (coupled with both anti-CD90 and anti-HGF antibodies) at a concentration of 50 beads/μL were added to the cultures. Experimental workflow outlined above (shaking, washing, incubation, and imaging steps) was followed (**Figure A7**).

Bead-Analyte Binding Validation: A model capture sandwich immunoassay was performed using both dual-functionalized beads (anti-CD90 and anti-HGF antibodies) and commercial mono-functionalized kit beads (Product # HAGP1MAP-12K) (anti-HGF antibody only) according to

manufacturer's instruction. Briefly, diluted beads (50 beads/µL) were incubated with recombinant human HGF protein [(clone #24516) (R&D Systems, Minneapolis, MN)] at concentrations ranging from 0 to 20,000 pg/mL (standard curve range according to each commercial kit). After incubation, beads were washed and detection antibody (biotinylated anti-human HGF polyclonal antibody, #BAF294, R&D Systems) was added to label the captured HGF. After binding of the detection antibody, streptavidin-R-phycoerythrin conjugate (SAPE) (ThermoFisher, #S866) was added and the corresponding fluorescence of the beads was analyzed. A five-parameter logistic fit (5PL) was used to fit calibration curves based on kit protocols. Calibration curves from each experiment, for both mono- and dual-functionalized beads, are shown in **Figure 2.2**. Curves were used to determine HGF concentration for each independent experiment. Limit of detection (LOD) was calculated using the standard definition of three times the background signal for each curve. Per manufacturer's instructions, if a well did not contain sufficient bead count (>50 beads), it was not analyzed and was excluded from further data analysis (**Figure 2.2 c** Experiment 3 20,000 pg/mL HGF standard, **Figure 2.4 bii** Experiment 3 control condition, **Figure A9** Experiment 3 control condition).

Cell-secreted HGF Assay: *Media preparation:* Two different media were used, one control and one treated. The control media consisted of EGM-2 supplemented with 10% HI-FBS and 1X PBS in place of antibody (control media). The treated media consisted of EGM-2 supplemented with 10% HI-FBS and free anti-HGF [(clone 24516) (R&D Systems, Inc., Minneapolis, MN)] in 1X PBS for a final concentration of 10 ng/mL free anti-HGF (treated media). Media were made fresh on the day of the experiment. *Localized cell-surface sampling:* NHDFn cells were cultured in a clear TCT 96-well plate as described above. On Day 3 post seeding, cells were washed once with media; 75 µL control (- free anti-HGF) or treated (+ free anti-HGF) media and 50 µL of diluted dual-functionalized (anti-HGF and anti-CD90) beads (100 beads/µL) in control media were added and incubated with the cells for 2 h. To distribute added beads within a well, the plate was shaken at 100 rpm for 1 min, then placed on a plate magnet (Stemcell Technologies, #18102) for 1 min;

this was done for a total of 3 rounds in the beginning of the incubation period. After 2 h, well contents were washed twice with 125 µL control media to remove any beads not bound to the cell surfaces; 50 µL of lysis buffer (10 mM Tris-HCl, 1 mM EDTA, 1% Triton X-100, 0.1% SDS, 140 mM NaCl) was then added and incubated for 15 mins to detach beads from the cell surface. A mini cell scraper (ABI Scientific Inc., catalog #MCS-200) was used 5 min into the 15 min lysis step to break up cellular debris during the lysing period. The plate was then placed on a magnet, and beads were washed with control media 3 times before being resuspended in 50 µL control media, collected, and added to assay plate; this resuspension was used as the final sample with no additional beads added and utilized for the Luminex assay. The assay was continued using the Luminex kit and procedure.[31] Briefly, samples were incubated for 16-20 h on an orbital shaker S5 at 4 °C. Beads are washed with wash buffer and secondary detection antibodies are added for a 1 h room temperature incubation. SAPE is then added for an additional 30 mins. Additional wash steps remove any unbound antibodies and SAPE before beads are resuspended in 1% BSA for analysis with FLEXMAP 3D System instrument. *Traditional bulk supernatant sampling:* Cell culture methods were the same as described in the above paragraph. On Day 3 post seeding, cells were washed once with media; 75 µL control (- free anti-HGF) or treated (+ free anti-HGF) media and 50 µL of control media were added and incubated with the cells for 2 h. Cell culture supernatant samples were collected from each well and transferred to new wells in a 96 well plate to be analyzed with mono-functionalized beads. The assay was continued using the Luminex kit and procedure.[31] Briefly, mono-functionalized (anti-HGF only) beads are added to supernatant samples to incubate for 16-20 h on an orbital shaker at 4 °C for HGF analyte capture. [Note: while dual-functionalized beads (anti-HGF and anti-CD90) described in the prior paragraph undergo the same process, it is important to note that analyte capture is completed prior to addition onto the assay plate for the dual-functionalized beads.] Beads are washed with wash buffer and secondary detection antibodies are added for a 1 h room temperature incubation. SAPE is then added for an additional 30 mins. Additional wash steps remove any unbound antibodies and SAPE before

beads are resuspended in 1% BSA for analysis with FLEXMAP 3D System instrument. *Transwell® assays:* Inverted Transwell® inserts were placed into a clear TCT 12-well plate after which a 50 µL fibroblast cell suspension ($2.6x10^4$ cells/mL) was placed on top of the Transwell® inverted insert (in the pore membrane area); cells were incubated for 2 h to allow cell adherence before Transwell® inserts were flipped and placed correctly into a clear TCT 24-well plate with 500 µL control media in the basal side (**Figure A8)**. Additionally, in other wells, cells were also cultured on the bottom of a clear TCT 24-well plate at the same density (**Figure A8**). Cells were cultured as described above for the remainder of the experiment. On Day 3 post seeding, 50 µL diluted beads (100 beads/µL) and 50 µL +/- free anti-HGF media were added to the apical side of the Transwell® inserts while 500 µL +/- free anti-HGF media was added to the basal side for a 2 h incubation. Beads were collected from the apical side of the Transwell® inserts and washed twice before being resuspended in 100 µL control media and added to assay plate; this resuspension was used as sample with no additional beads added. The assay was continued as previously described above using the Luminex kit and procedure. The data are presented in **Figure A6**.

Instrumentation: Analysis for all bead-based assays (MF and DF beads) were performed on a FLEXMAP 3D System (Luminex Corp.) in the Immune Monitoring Lab (Fred Hutchinson Cancer Research Center, Seattle, WA). The microspheres were analyzed with the following settings: 50 beads, 50 events/bead, 75 µL, bead region 45 (commercial kit mono-functionalized beads) or 34 (dual-functionalized beads), 5000 – 30000 gate, 60 sec time out. Fluorescent images of the cells and beads were obtained using a Zeiss Axiovert 200 and an Axiocam 503 mono camera (Carl Zeiss AG, Oberkochen, Germany). Data and statistical analyses were completed using Prism (Graphpad, San Diego, CA) software. All cell and bead images were processed using FIJI image software (ImageJ, NIH).

2.6 References

1. G. M. Cooper, Signaling Molecules and Their Receptors.
2. W. Zhao, C. A. Oskeritzian, A. L. Pozez and L. B. Schwartz, Cytokine Production by Skin-Derived Mast Cells: Endogenous Proteases Are Responsible for Degradation of Cytokines, *J. Immunol.*, 2005, **175**, 2635–2642.
3. Y. Niwa, H. Akamatsu, H. Sumi, Y. Ozaki and A. Abe, Evidence for degradation of cytokines in the serum of patients with atopic dermatitis by calcium-dependent protease, *Arch. Dermatol. Res.*, 2000, **292**, 391–396.
4. K. R. Maddipati and S. L. Zhou, Stability and analysis of eicosanoids and docosanoids in tissue culture media, *Prostaglandins Other Lipid Mediat.*, 2011, **94**, 59–72.
5. Y. S. Chhonker, V. Bala and D. J. Murry, Quantification of eicosanoids and their metabolites in biological matrices: a review, 2018, **10**, 2027–2046.
6. K. Felix and M. M. Gaida, Neutrophil-Derived Proteases in the Microenvironment of Pancreatic Cancer -Active Players in Tumor Progression, *Int. J. Biol. Sci.*, 2016, **12**, 302.
7. Z. Fu, M. Thorpe, R. Alemayehu, A. Roy, J. Kervinen, L. de Garavilla, M. Åbrink and L. Hellman, Highly Selective Cleavage of Cytokines and Chemokines by the Human Mast Cell Chymase and Neutrophil Cathepsin G, *J. Immunol.*, 2017, **198**, 1474–1483.
8. O. Wiedow and U. Meyer-Hoffert, Neutrophil serine proteases: potential key regulators of cell signalling during inflammation, *J. Intern. Med.*, 2005, **257**, 319–328.
9. X. Zhou, M. S. Fragala, J. E. McElhaney and G. A. Kuchel, Conceptual and methodological issues relevant to cytokine and inflammatory marker measurements in clinical research, *Curr. Opin. Clin. Nutr. Metab. Care*, 2010, **13**, 541.
10. J. M. Inal, U. Kosgodage, S. Azam, D. Stratton, S. Antwi-Baffour and S. Lange, Blood/plasma secretome and microvesicles, *Biochim. Biophys. Acta - Proteins Proteomics*, 2013, **1834**, 2317–2325.
11. H. Haslene-Hox, O. Tenstad and H. Wiig, Interstitial fluid—A reflection of the tumor cell microenvironment and secretome, *Biochim. Biophys. Acta - Proteins Proteomics*, 2013, **1834**, 2336–2346.
12. P. Mukherjee and S. Mani, Methodologies to decipher the cell secretome, *Biochim. Biophys. Acta - Proteins Proteomics*, 2013, **1834**, 2226–2232.
13. P. Müller and A. F. Schier, Extracellular Movement of Signaling Molecules, *Dev. Cell*, 2011, **21**, 145–158.
14. K. J. Son, P. Gheibi, G. Stybayeva, A. Rahimian and A. Revzin, Detecting cell-secreted growth factors in microfluidic devices using bead-based biosensors, *Microsystems Nanoeng. 31*, 2017, **3**, 1–9.
15. K. J. Son, A. Rahimian, D. S. Shin, C. Siltanen, T. Patel and A. Revzin, Microfluidic compartments with sensing microbeads for dynamic monitoring of cytokine and exosome release from single cells, *Analyst*, 2016, **141**, 679–688.
16. Y. Ji, D. Qi, L. Li, H. Su, X. Li, Y. Luo, B. Sun, F. Zhang, B. Lin, T. Liu and Y. Lu, Multiplexed profiling of single-cell extracellular vesicles secretion, *Proc. Natl. Acad. Sci. U. S. A.*, 2019, **116**, 5979–5984.
17. M. N. Hsu, S. C. Wei, S. Guo, D. T. Phan, Y. Zhang and C. H. Chen, Smart Hydrogel Microfluidics for Single-Cell Multiplexed Secretomic Analysis with High Sensitivity, *Small*, 2018, DOI:10.1002/SMLL.201802918.
18. I. Barbulovic-Nad, H. Yang, P. S. Park and A. R. Wheeler, Digital microfluidics for cell-based assays, *Lab Chip*, 2008, **8**, 519–526.
19. A. Gérard, A. Woolfe, G. Mottet, M. Reichen, C. Castrillon, V. Menrath, S. Ellouze, A. Poitou, R. Doineau, L. Briseno-Roa, P. Canales-Herrerias, P. Mary, G. Rose, C. Ortega, M. Delincé, S. Essono, B. Jia, B. Iannascoli, O. Richard-Le Goff, R. Kumar, S. N. Stewart, Y. Pousse, B. Shen, K. Grosselin, B. Saudemont, A. Sautel-Caillé, A. Godina, S. McNamara,

K. Eyer, G. A. Millot, J. Baudry, P. England, C. Nizak, A. Jensen, A. D. Griffiths, P. Bruhns and C. Brenan, High-throughput single-cell activity-based screening and sequencing of antibodies using droplet microfluidics, *Nat. Biotechnol., 386*, 2020, **38**, 715–721.

20. K. Eyer, R. C. L. Doineau, C. E. Castrillon, L. Briseño-Roa, V. Menrath, G. Mottet, P. England, A. Godina, E. Brient-Litzler, C. Nizak, A. Jensen, A. D. Griffiths, J. Bibette, P. Bruhns and J. Baudry, Single-cell deep phenotyping of IgG-secreting cells for high-resolution immune monitoring, *Nat. Biotechnol., 3510*, 2017, **35**, 977–982.
21. V. Chokkalingam, J. Tel, F. Wimmers, X. Liu, S. Semenov, J. Thiele, C. G. Figdor and W. T. S. Huck, Probing cellular heterogeneity in cytokine-secreting immune cells using droplet-based microfluidics, *Lab Chip*, 2013, **13**, 4740–4744.
22. J. H. Cox, G. Ferrari and S. Janetzki, Measurement of cytokine release at the single cell level using the ELISPOT assay, *Methods*, 2006, **38**, 274–282.
23. S. Janetzki, M. Rueger and T. Dillenbeck, Stepping up ELISpot: Multi-Level Analysis in FluoroSpot Assays, *Cells 2014, Vol. 3, Pages 1102-1115*, 2014, **3**, 1102–1115.
24. K. J. Regehr, M. Domenech, J. T. Koepsel, K. C. Carver, S. J. Ellison-Zelski, W. L. Murphy, L. A. Schuler, E. T. Alarid and D. J. Beebe, Biological implications of polydimethylsiloxane-based microfluidic cell culture, *Lab Chip*, 2009, **9**, 2132–2139.
25. J. N. Lee, C. Park and G. M. Whitesides, Solvent Compatibility of Poly(dimethylsiloxane)-Based Microfluidic Devices, *Anal. Chem.*, 2003, **75**, 6544–6554.
26. N. Reslova, V. Michna, M. Kasny, P. Mikel and P. Kralik, xMAP technology: Applications in detection of pathogens, *Front. Microbiol.*, 2017, **8**, 55.
27. B. D. Plouffe, S. K. Murthy and L. H. Lewis, Fundamentals and application of magnetic particles in cell isolation and enrichment: a review, *Reports Prog. Phys.*, 2014, **78**, 016601.
28. M. Biotec, Cytokine Capture System (IFN-gamma) Product Sheet. 200-070-217.
29. Y. Zhou, N. Shao, R. Bessa de Castro, P. Zhang, Y. Ma, X. Liu, F. Huang, R. F. Wang and L. Qin, Evaluation of Single-Cell Cytokine Secretion and Cell-Cell Interactions with a Hierarchical Loading Microwell Chip, *Cell Rep.*, 2020, **31**, 107574.
30. T. Nakamura and S. Mizuno, The discovery of Hepatocyte Growth Factor (HGF) and its significance for cell biology, life sciences and clinical medicine, *Proc. Japan Acad. Ser. B*, 2010, **86**, 588–610.
31. S. Angeloni, D. Shubhagata, D. Sherry, S. Valerie and S. Sarah, *xMAP ® Cookbook A collection of methods and protocols for developing multiplex assays with xMAP ® Technology,* Luminex Corp, Austin, TX, 4th edn., 2022.
32. J. H. Day, T. M. Nicholson, X. Su, T. L. Van Neel, I. Clinton, A. Kothandapani, J. Lee, M. H. Greenberg, J. K. Amory, T. J. Walsh, C. H. Muller, O. E. Franco, C. R. Jefcoate, S. E. Crawford, J. S. Jorgensen and A. B. Theberge, Injection molded open microfluidic well plate inserts for user-friendly coculture and microscopy, *Lab Chip*, 2020, DOI:10.1039/c9lc00706g.

Chapter 3│ *Guess who: using cell-targeting beads to investigate cellular communication via soluble factors*

This chapter contains work which is ongoing at the time of this dissertation's submission. The proposed experimental work is outlined below. The anticipated author list is: T.L. van Neel, A.B. Theberge,[§] and E. Berthier[§].
[§] Co-corresponding authors

3.1 Introduction

Soluble factors secreted by cells into the extracellular microenvironment (i.e., the secretome) is one mode of communication cells employ to affect cellular function.[1] These chemical signals guide a diverse range of biological processes from cell growth and maintenance to immune and inflammatory responses. Cytokines are small proteins that drive cell function during the immune response and act as immunomodulators.[2] Secretion of cytokines from a heterogenous cell population are determined by the types of cells present, the quantity of cells present, and the concentration of cytokines present within the microenvironment.[3,4] This makes for a dynamic environment, with cytokine levels frequently changing. Following the movement of cytokines is key to translating and deciphering signaling cascades in disease progression which is of great importance for many areas including therapeutics and basic science knowledge. Additionally, several cytokines are pleiotropic and can affect multiple targets which further complicates linking the role of cytokines to primary functions.[3] However, many cytokines are like whispers in the signaling milieu, making it incredibly difficult to measure them amongst the shouts of other dominant cytokine signals.

Accurate detection of physiological levels of cytokines is challenging due to their low concentration (picomolar range), transient nature, and short lifespan in the signaling environment.[2,5] Signaling networks are complicated webs and unraveling how they work requires simultaneous quantification of multiple soluble factors to get a better understanding of what is happening within the cell landscape. For this reason—amongst others—enzyme-linked immunosorbent assays (ELISA) are amongst the most widely used methods for measuring

soluble factors such as cytokines, growth factors, and chemokines.[6] Many soluble factors can be quantified from a single-100 µL sample using an ELISA platform or amplified using PCR techniques before analysis but these methods take hours (>6 hours) to perform.[7] Additionally, cytokines with short lifespans are often missing or severely diminished in samples analyzed with these methods due to degradation, conversion, or removal.[2,8] Furthermore, these measurement methods provide little insight into what cell type produced a cytokine or what cell type is receiving and using that cytokine. Thus, there is a need for a method that can capture cell-secreted analytes within the signaling microenvironment and one which can decode the producer or receiver of a cytokine.

Bead-based immunoassay platforms are attractive methods for measuring soluble factors because they are specific, sensitive, and can be multiplexed.[9–11] Beads are typically used to either capture a soluble factor in biological samples (such as serum isolated from blood, conditioned media, etc.) or isolate cell types from a heterogenous cell sample (e.g., tissue biopsies).[12] Other next-generation bead-based technologies exist like hydrogel beads which absorb molecules based on size[13] or designer microparticles with unique cavities[14], which are well-positioned for single-cell studies. We are focused on creating a bridging method which provides more information than bulk fluid analysis but does not have single cell level information. Prior to our work, the two functionalities—soluble factor capture and cell binding—had never been incorporated onto one bead (described in Chapter 2 of this dissertation).[15] Our dual-functionalized beads are surface functionalized with two different antibodies – one antibody serves to capture a soluble factor while the second antibody enables bead tethering to a cell surface during a cell culture period. This enables researchers to listen in on cellular communication while understanding how soluble factors are being used in signaling pathways during critical moments in disease progression. Importantly, our capture method can be easily integrated into existing cell culture setups without requiring modifications to the cell culture setup.

Herein we describe the proposed deployment of dual-functionalized beads for localized cell-surface sampling in tracking the exchange of a cell-secreted soluble factor in a coculture model. Our previous work detailed the creation of a bead that targets fibroblast cells and captures cell-secreted hepatocyte growth factor (HGF). Building upon that work, we have developed a second dual-functionalized bead to target endothelial cells and capture cell-secreted HGF. By deploying both bead sets in a coculture model comprising fibroblast and endothelial cells, we hope to observe and identify which cell type produces HGF and which cell type utilizes or receives HGF based on the bead set analysis.

3.2 Proposed experimental design and workflow

The body contains highly structured cellular architectures where the organization of different cell types influences the function and signaling observed. While 3D tissue models accurately capture complex cellular interactions, they are often complicated to establish. Thus, mimicking and translating 3D structures that are well-defined into 2D setups is important when trying to simplify biological complexity whilst trying to understand the role soluble factors play in signaling pathways. To provide a controlled environment for observing how hepatocyte growth factor (HGF) moves between fibroblast cells and endothelial cells, we chose to utilize a segregated coculture system. To achieve this, a polydimethylsiloxane (PDMS) well-plate insert was designed. Fabrication of the insert mold was first completed using computer numerical control (CNC) micromilling, followed by a casting method to create the well-plate insert. The well-plate insert comprises of two cell culture chambers separated by a wall so that the cell types are physically separated (**Figure 3.1 a**). Removal of the insert from the well allows soluble factor signaling to be initiated as the two cell types then share one signaling environment via media.

Measurement of HGF within this fibroblast cell and endothelial cell coculture system is achieved using two different dual-functionalized bead sets. Bead F consists of anti-CD90 and anti-HGF antibodies to target fibroblast cells; bead E consists of anti-CD31 and anti-HGF

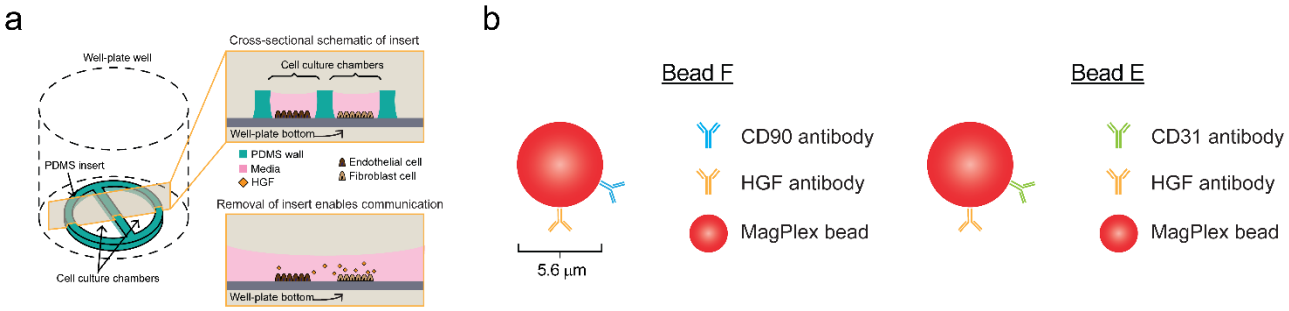

Figure 3.1. Components for localized cell-surface sampling in a coculture model. (a) shows the PDMS well-plate insert and (b) shows the two bead sets developed. Bead F targets fibroblast cells via CD90 antibodies and captures HGF while Bead E targets endothelial cells via CD31 antibodies and captures HGF.

antibodies to target endothelial cells (**Figure 3.1 b**). Due to the dual-functionalization of the bead sets, they can be added directly to cell cultures for simultaneous cell-tethering (via CD90 or CD31) and soluble factor capture. Moreover, by localizing our sampling of soluble factors to the cell-surface, we are able to protect soluble factors with short lifespans from being removed whilst maintaining sensitivity of picomolar concentrations. A schematic shown in **Figure 3.2** outlines the proposed workflow for conducting localized cell-surface sampling.

One of the main advantages to using beads is the ability to multiplex or detect multiple different beads within a sample. This is possible because each bead set contains a unique ratio of fluorescent dye. Analysis of the bead sets with an immunoassay allows us to quantify the HGF captured within the culture from each cell type. Additional insights into the signaling route between the two cell types is also provided because we can trace the likely source and receiver of the soluble factor by comparing the measured concentration of the soluble factor. By probing different culture setups (fibroblast cell monoculture, endothelial cell monoculture, and coculture of the two cell types), we can begin to tease apart how a soluble factor is used between two cell types and what influence that signaling has within the context of broader functions.

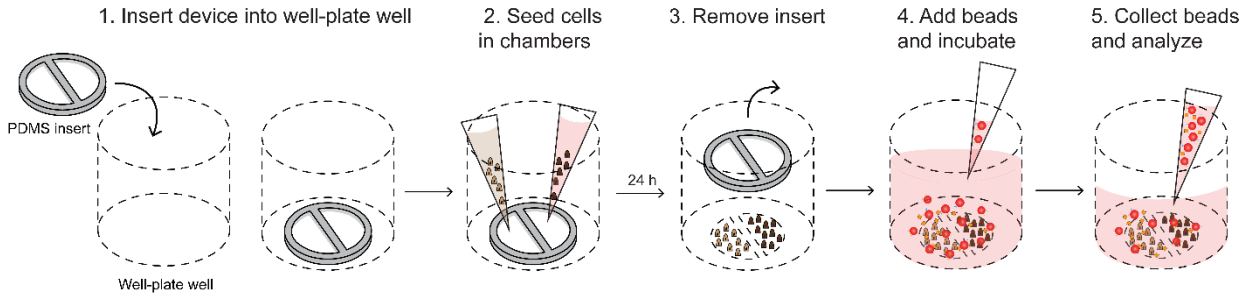

Figure 3.2. Localized cell-surface sampling workflow for coculture model. The basic steps are shown in which a PDMS well-plate insert is added. Two cell types are then seeded into their respective chamber for 24 h before the insert is removed to enable soluble factor communication. Bead F and E are added for a 2 h sampling period. The beads are then collected and analyzed using an immunoassay.

3.3 Ongoing work

The current work is focused on executing experiments which support the hypotheses detailed above. We hope to demonstrate that designed beads F and E (i) localize to and (ii) bind to their targeted cell type with minimal to no off-target binding. Our expectation is to see a majority of the measured HGF from bead F (fibroblast cells) with a reduced signal from bead E (endothelial cells) relative to bead F; this is because fibroblast cells are known to be a main producer of HGF.[16] Additionally, we will reduce the sampling time of the bead sets (from 2 h to 1 h or 20 min) to investigate the effects on the measured HGF. We hope to show that soluble factor secretion from cells and the removal of soluble factors from the signaling landscape is fast (seconds to minutes) and that methods such as these can be utilized to protect cytokines with short lifespans without losing sensitivity. Ultimately, we envision these bead sets to be used in cell or tissue culture studies to help researchers identify either what cell type is responsible for producing a soluble factor or what and how a cell type might be using a soluble factor within a signaling microenvironment.

3.4 Materials and Methods

Reagents and Materials: Luminex kits (Product # HAGP1MAP-12K) containing wash buffer, assay buffer, secondary detection antibody, mono-functionalized beads, recombinant human

hepatocyte growth factor (HGF), and streptavidin-R-phycoerythrin conjugate (SAPE) were purchased from EMD Millipore (Burlington, MA). Clear tissue culture treated (TCT) 24-well plates (Corning #3526) and black TCT 96-well plates (Corning #3603) were purchased from Corning (Corning, NY).

Well-plate inserts: A device insert mold was created using Solidworks (Dassault Systems, Waltham, MA) and fabricated from 1.2 mm thick polystyrene sheets using a CNC micromill (Datron neo, Datron Dynamics). Molds were then cleaned using 70% ethanol, rinsed with DI water, and finally dried with air. Polydimethylsiloxane (PDMS) (Slygard™ 184, Dow) was made using a 9:1 ratio and poured onto molds; PDMS was cured at 85 ºC for 2 h before inserts were removed from the mold. A Soxhlet extraction with 100% ethanol was used to remove any uncrosslinked oligomers for 4 cycles. Device inserts were sterilized via autoclave before use.

Cell Culture: Normal Human Dermal Fibroblast neo-natal cells (NHDFn) (ATCC, Manassas, VA) were cultured, passaged, and seeded in fibroblast basal medium supplemented with a low-serum growth kit (ATCC, #PCS-201-030 and #PCS-201-041) (fibroblast media). NHDFn passage numbers ranged from 5-8 for experiments. Human Umbilical Vein Endothelial cells (HUVEC) (Lonza, Basel, Switzerland, #C2517A) were cultured, passaged, and seeded in EGM-2 media. HUVEC passage numbers ranged from 5-8 for experiments.

Bead Functionalization: MagPlex microspheres (region 13 and 90) were purchased from Luminex Corp. and functionalized with mouse anti-human hepatocyte growth factor (anti-HGF) monoclonal antibody [(clone 24516) (R&D Systems, Inc., Minneapolis, MN)] and either mouse anti-human cluster of differentiation 90 (anti-CD90) monoclonal antibody [(clone AF-9) (Abcam, Cambridge, MA)] or mouse anti-human cluster of differentiation 31 (anti-CD31) monoclonal antibody [(clone WM59) (Bio-Rad, Hercules, CA) according to xMAP Luminex protocols.[17] Briefly, carboxylated microspheres were first activated with 1-ethyl-3-[3-dimethylaminopropyl] carbodiimide hydrochloride (EDC) and sulfo-N-hydroxysulfosuccinimide (Sulfo-NHS). Once activated, antibodies were added at a 1:1 concentration-based ratio to covalently bind to the surface of the

activated microspheres. Once coupled, microspheres were rinsed and stored in phosphate buffered saline (PBS) containing 1% bovine serum albumin (BSA) at 4 °C until use. Care was taken to protect the microspheres from light to prevent photobleaching during coupling. Microspheres were used as per the manufacturer's instructions and within 6 months of coupling. To validate successful coupling of the antibodies with the microspheres, we performed a secondary antibody labeling and subsequent analysis.[17] Briefly, phycoerythrin-conjugated rat anti-mouse IgG (clone M1-14D12) (ThermoFisher Scientific) was added to the microspheres at a range of concentrations (0.0625 µg/mL to 4 µg/mL), incubated, and analyzed to generate a calibration curve as per the manufacturer's instructions.

Bead-Analyte Binding Validation: A model capture sandwich immunoassay was performed using dual-functionalized beads (anti-CD90/anti-HGF; anti-CD31/anti-HGF) and a commercially available immunoassay kit protocol. Briefly, diluted beads (50 beads/µL) were incubated with recombinant human HGF protein at concentrations ranging from 0 to 20,000 pg/mL (standard curve range according to each commercial kit). After incubation, beads were washed and detection antibody was added to label the captured HGF. After binding of the detection antibody, streptavidin-R-phycoerythrin conjugate (SAPE) was added and the corresponding fluorescence of the beads was analyzed. A five-parameter logistic fit (5PL) was used to fit calibration curves based on kit protocols. Limit of detection (LOD) was calculated using the standard definition of three times the background signal for each curve. Per manufacturer's instructions, if a well did not contain sufficient bead count (> 50 beads), it was not analyzed and was excluded from further data analysis.

Localized cell-surface sampling: Sterilized PDMS device inserts were placed in wells on a clear TCT 24-well plate. NHDFn and HUVEC cells were seeded and cultured into device chambers for 24 h. 24 h post seeding, device inserts were removed, and cells were washed once with EGM-2 media. A bead solution containing both anti-CD90/anti-HGF and anti-CD31/anti-HGF beads (each at a concentration of 50 beads/µL) was made in EGM-2 media and added to wells for a 2 h

incubation. To distribute added beads within a well, the plate was shaken at 100 rpm for 1 min, then placed on a plate magnet (Stemcell Technologies, #18102) for 1 min; this was done for a total of 3 rounds in the beginning of the incubation period. After 2 h, well contents were washed twice with EGM-2 media to remove any beads not bound to the cell surfaces; lysis buffer (10 mM Tris-HCl, 1 mM EDTA, 1% Triton X-100, 0.1% SDS, 140 mM NaCl) was then added and incubated for 15 min to detach beads from the cell surface. A mini cell scraper (ABI Scientific Inc., catalog #MCS-200) was used 5 min into the 15 min lysis step to break up cellular debris during the lysing period. The plate was then placed on a magnet, and beads were washed with wash buffer 3 times before being resuspended in EGM-2 media, collected, and added to assay plate; this resuspension was used as the final sample with no additional beads added and utilized for the Luminex assay. The assay was continued using the immunoassay kit and a modified procedure.[17] Briefly, beads were washed with wash buffer and secondary detection antibodies are added for a 1 h room temperature incubation. SAPE is then added for an additional 30-min incubation. Additional wash steps remove any unbound material before beads are resuspended in 1% BSA for analysis.

Instrumentation: Analysis weas performed on a Luminex 100/200 System (Luminex Corp.). The microspheres were analyzed with the following settings: 50 beads, 50 events/bead, 75 µL, bead region [13 (anti-CD31/anti-HGF dual-functionalized bead) and 90 (anti-CD90/anti-HGF dual-functionalized bead)], 5000 – 30000 gate, 60 sec time out. Data and statistical analyses were completed using Prism (Graphpad, San Diego, CA) and Belysa (Millipore Sigma) software.

3.5 References

1. M. Uhlén, M. J. Karlsson, A. Hober, A. S. Svensson, J. Scheffel, D. Kotol, W. Zhong, A. Tebani, L. Strandberg, F. Edfors, E. Sjöstedt, J. Mulder, A. Mardinoglu, A. Berling, S. Ekblad, M. Dannemeyer, S. Kanje, J. Rockberg, M. Lundqvist, M. Malm, A. L. Volk, P. Nilsson, A. Månberg, T. Dodig-Crnkovic, E. Pin, M. Zwahlen, P. Oksvold, K. von Feilitzen, R. S. Häussler, M. G. Hong, C. Lindskog, F. Ponten, B. Katona, J. Vuu, E. Lindström, J. Nielsen, J. Robinson, B. Ayoglu, D. Mahdessian, D. Sullivan, P. Thul, F. Danielsson, C. Stadler, E. Lundberg, G. Bergström, A. Gummesson, B. G. Voldborg, H. Tegel, S. Hober, B. Forsström, J. M. Schwenk, L. Fagerberg and Å. Sivertsson, The human secretome, *Sci. Signal.*, 2019,

12, eaaz0274.
2. C. Liu, D. Chu, K. Kalantar-Zadeh, J. George, H. A. Young and G. Liu, Cytokines: From Clinical Significance to Quantification, *Adv. Sci.*, 2021, **8**, 2004433.
3. J. A. Stenken and A. J. Poschenrieder, Bioanalytical chemistry of cytokines – A review, *Anal. Chim. Acta*, 2015, **853**, 95–115.
4. L. Naomi Handly, A. Pilko and R. Wollman, Paracrine communication maximizes cellular response fidelity in wound signaling, *Elife*, , DOI:10.7554/ELIFE.09652.
5. T. L. Whiteside, Cytokines and cytokine measurements in a clinical laboratory., *Clin. Diagn. Lab. Immunol.*, 1994, **1**, 257.
6. E. L. Chiswick, E. Duffy, B. Japp and D. Remick, Detection and quantification of cytokines and other biomarkers, *Methods Mol. Biol.*, 2012, **844**, 15–30.
7. A. Giulietti, L. Overbergh, D. Valckx, B. Decallonne, R. Bouillon and C. Mathieu, An overview of real-time quantitative PCR: applications to quantify cytokine gene expression, *Methods*, 2001, **25**, 386–401.
8. W. De Jager, K. Bourcier, G. T. Rijkers, B. J. Prakken and V. Seyfert-Margolis, Prerequisites for cytokine measurements in clinical trials with multiplex immunoassays, *BMC Immunol.*, 2009, **10**, 52.
9. H. Graham, D. J. Chandler and S. A. Dunbar, The genesis and evolution of bead-based multiplexing, *Methods*, 2019, **158**, 2–11.
10. S. A. Dunbar, Applications of Luminex® xMAP™ technology for rapid, high-throughput multiplexed nucleic acid detection, *Clin. Chim. Acta.*, 2006, **363**, 71.
11. M. Vostrý, Multiplex Immunoassays: Chips and Beads, *EJIFCC*, 2010, **20**, 162.
12. M. A. Witek, I. M. Freed and S. A. Soper, Cell Separations and Sorting, *Anal. Chem.*, 2020, **92**, 105.
13. C. Longo, A. Patanarut, T. George, B. Bishop, W. Zhou, C. Fredolini, M. M. Ross, V. Espina, G. Pellacani, E. F. Petricoin, L. A. Liotta and A. Luchini, Core-Shell Hydrogel Particles Harvest, Concentrate and Preserve Labile Low Abundance Biomarkers, *PLoS One*, 2009, **4**, e4763.
14. S. Lee, J. De Rutte, R. Dimatteo, D. Koo and D. Di Carlo, Scalable Fabrication and Use of 3D Structured Microparticles Spatially Functionalized with Biomolecules, *ACS Nano*, 2022, **16**, 38–49.
15. T. L. van Neel, S. B. Berry, E. Berthier and A. B. Theberge, Localized Cell-Surface Sampling of a Secreted Factor Using Cell-Targeting Beads, *Anal. Chem.*, 2020, DOI:10.1021/acs.analchem.0c02578.
16. N. Molnarfi, M. Benkhoucha, H. Funakoshi, T. Nakamura and P. H. Lalive, Hepatocyte growth factor: A regulator of inflammation and autoimmunity, *Autoimmun. Rev.*, 2015, **14**, 293–303.
17. S. Angeloni, D. Shubhagata, D. Sherry, S. Valerie and S. Sarah, *xMAP ® Cookbook A collection of methods and protocols for developing multiplex assays with xMAP ® Technology*, Luminex Corp, Austin, TX, 4th edn., 2022.

Chapter 4 | Enabling cell culture models and platforms

The content of this chapter will discuss the fabrication and use of two different cell culture models. The first half of the chapter will discuss a method to create hydrogel lumen structures using a casting approach. The second half of this chapter will focus on the characterization of an injection-molded cell culture insert and its use in a variety of applications.

4.1 Freestanding hydrogel lumens for modeling blood vessels and vasodilation

Reproduced in part from A.M. Dostie, H.G. Lea*, U.N. Lee*, T.L. van Neel, E. Berthier, A.B. Theberge "Freestanding hydrogel lumens for modeling blood vessels and vasodilation." SLAS Technologies,* ***2022****, 27, 344-349.*
** Equal contribution*

AMD, HGL, and UNL conceptualized the project and created methods; AMD, HGL, UNL, and TLvN conducted experiments; AMD, UNL, EB, and ABT interpreted results; EB and ABT supervised work. TLvN conducted experimental work shown in ***Figure 4.1.2*** *and contributed to writing the manuscript.*

Abstract: Lumen structures exist throughout the human body, and the vessels of the circulatory system are essential for carrying nutrients and oxygen and regulating inflammation. Vasodilation, the widening of the blood vessel lumen, is important to the immune response as it increases blood flow to a site of inflammation, raises local temperature, and enables optimal immune system function. A common method for studying vasodilation uses excised vessels from animals; major drawbacks include heterogeneity in vessel shape and size, time-consuming procedures, sacrificing animals, and differences between animal and human biology. We have developed a simple, user-friendly *in vitro* method to form freestanding cell-laden hydrogel rings from collagen and quantitatively measure the effects of vasodilators on ring size. The hydrogel rings are composed of collagen I and can be laden with human vascular smooth muscle cells, a major cellular and structural component of blood vessels, or lined with endothelial cells in the lumen. The methods presented include a 3D printed device (which is amenable to future fabrication by injection molding) and commercially available components (e.g., Teflon tubing or a syringe) to form hydrogel rings between 2.6–4.6 mm outer diameter and 0.79–1.0 mm inner diameter. Here

we demonstrate a significant difference in ring area in the presence of a known vasodilator, fasudil ($p < 0.0001$). Our method is easy to implement and provides a foundation for a medium-throughput solution to generating vessel model structures for future investigations of the fundamental mechanisms of vasodilation (e.g., studying uncharacterized endogenous molecules that may have vasoactivity) and testing vasoactive drugs.

4.1.1 Introduction

Lumen structures exist throughout the body including in the glandular organs such as the breast and prostate, and blood vessels of the circulatory system. Vasodilation, the widening of the blood vessel lumen, is important to the immune response as it increases blood flow to a site of inflammation, raises local temperature, and enables optimal immune system function.[1] Over the last two decades, tissue engineers and cell biologists have been working towards performing cell culture experiments in a three-dimensional environment, as opposed to two-dimensional culture.[2–4] It is well accepted that in the human body, cells are encapsulated in a 3D environment (extracellular matrix, ECM) and receive signals very differently than they would in a 2D polystyrene culture plate. Incorporation of relevant hydrogels, multiculture of different cell types, or generation of specific architectures, such as tubular structures, have resulted in changes in cell behavior that more closely recapitulate in vivo cell function and morphology.[5,6] Such observations have been increasingly helpful in drug discovery and tissue engineering due to increased cell to cell contact, cell communication, and cell-ECM interactions.[3] Current methods for studying vasodilation and constriction involve time-consuming ex vivo methods utilizing blood vessels excised from animals (e.g., rabbit and rodent models), and simplified in vitro methods that capture a portion of the biological response.[7–10] While excised animal vessels are valuable in understanding cell signaling in an ex vivo environment, procedures are time intensive, requiring processing of the excised tissue and then almost immediate testing of samples; additionally, the responses observed in these excised vessels may not be representative of a response in human tissue.[11] An innovative model system is needed that is (1) simple to use and multiplex, enabling

rapid adoption by biology laboratories, (2) incorporates multiple human cell types, and (3) can quantify the degree of dilation.

To offer an alternative to animal methods and clinical trials in humans,[12–14] several groups have recently developed in vitro assays with primary human smooth muscle cells to study the effects of vasoactive compounds.[11,15–18] Alford et al. created what they called 'muscular thin filament', or MTFs, which are strips of polydimethylsiloxane (PDMS) with adhered vascular smooth muscle cells.[15] The MTFs were imaged and analyzed, measuring constriction or dilation by curvature of the MTF.[15,17,19] Alternatively, several groups have performed vasoactivity tests on tissue engineered blood vessels (TEBVs) as part of characterization of TEBVs to be used for drug testing[16] or to be potentially implanted as vascular grafts.[18] Recently, Tseng et al. developed a platform to study vasoactivity of vascular smooth muscle cells that were 3D printed into a ring configuration that fit within the well of a 96-well plate.[11] Other well-based methods have been created that enable cells to settle and self-assemble into a ring formation.[20,21] We sought to add to this body of work by developing a user-friendly method for generating blood vessel mimics that require only commercially available supplies and simple parts produced with an inexpensive resin 3D printer. Additionally, the device can be scaled up by injection molding in polystyrene, a common cell culture material.[22]

Here, we present a modular casting method to form a 3D hydrogel structure with a lumen (i.e., a ring) that is embedded with smooth muscle cells. The method is user friendly and amenable to medium-throughput experiments (~100 rings per day). These hydrogel rings are 2.6–4.6 mm in outer diameter, 0.79–1.0 mm in inner diameter, and are free-standing and transferable between well plates. The lack of attachment to any surface enables the hydrogel to be remodeled by the cells; thus, the addition of vasoactive compounds results in a visible and quantifiable readout. Our method enables the use of smooth muscle cells embedded in the hydrogel and endothelial cells in the lining of the lumen. Our method has the potential to be developed further and used to assay

potential drug candidates to reduce harmful vasodilation in patients with various inflammatory diseases (e.g., asthma, rheumatoid arthritis, Raynaud's syndrome).

4.1.2 Forming lumen structures using a casting approach

Our goal was to develop a user-friendly protocol for producing cell-laden hydrogel rings that can be used for medium-throughput biological and drug screening experiments. Lumen structures are commonplace in the human body; our area of focus in this work was modeling blood vessels to study vasodilation. Two casting methods were utilized to produce cell-laden hydrogel rings, however only one will be presented here (**Figure 4.1.1**); both methods are easy to implement with 3D printed components and low-cost commercially available materials (e.g., Teflon tubing). A table comparing the general features of excised animal tissue models, standard closed microfluidic lumen models, and our freestanding method is included in Appendix B (**Table B1**).

To use cell-laden hydrogel rings in vasoactivity experiments, it is important that the hydrogel is not attached to stiff materials that may prevent hydrogel deformation (i.e., dilation or constriction); therefore, our approach was to cast hydrogels using an easily removable mold. We used a simple 3D printed design and Teflon tubing to mold precursor hydrogel solution into a ring that could be removed and placed in a standard 96-well plate. Current 3D printed molds consist of 6 posts per device, enabling the generation of 6 hydrogel rings per mold. It is feasible to make ~100 rings per day with each rack taking ~10 min total for assembly and loading of hydrogel. Incubation time varies on the hydrogel used (1 h for collagen). Other methods that utilize specialized assemblies to hold or rotate the rings during incubation limit the throughput of hydrogel ring structures to approximately <10 per experiment. Additionally, testing vasodilation with ex vivo vessels from mice or rabbits and wire myography only enables the measurement of 1-4 vessels at a time.[23] A PDMS spacer was applied to the device, and Teflon tubing was added onto each post (**Figure 4.1.1 aii**). The PDMS spacer holds up the Teflon tubing and enables the

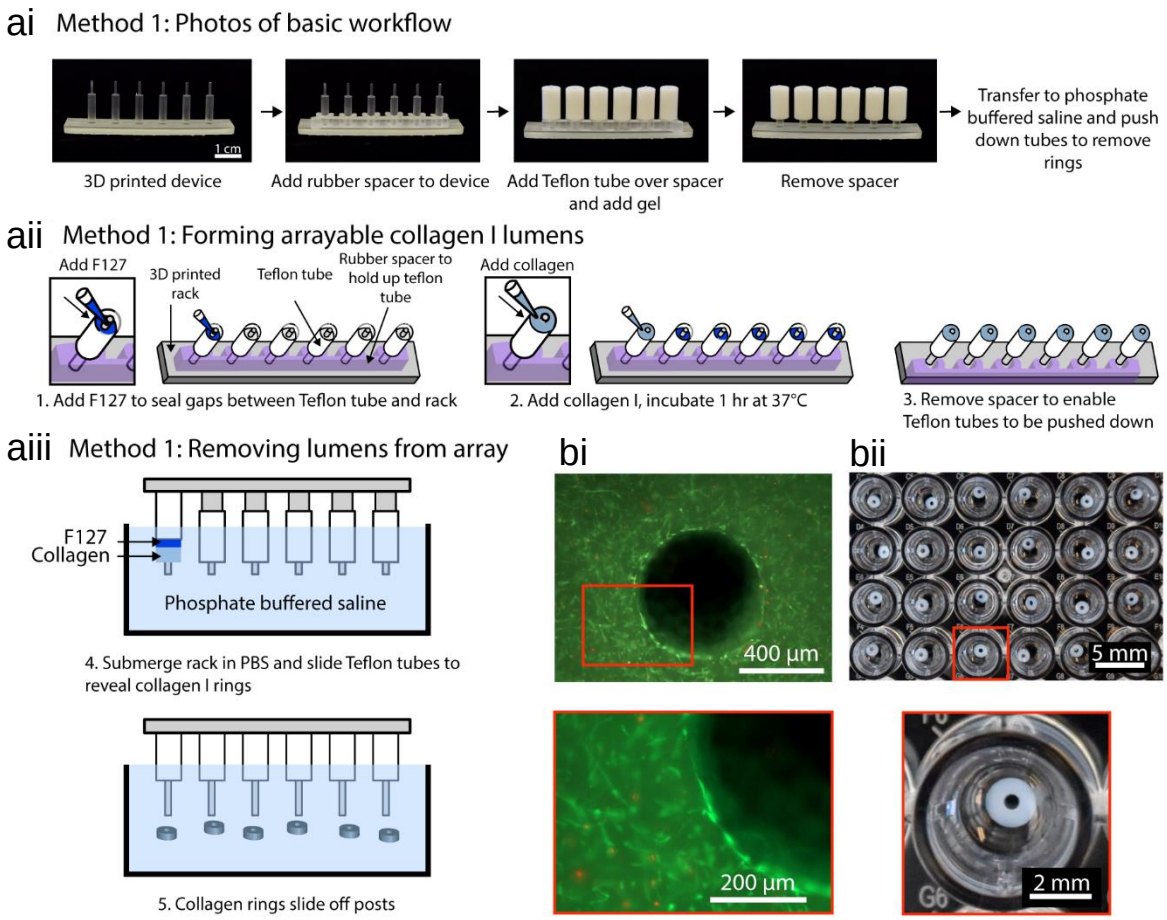

Figure 4.1.1. An arrayable method for fabricating cell-embedded free-standing collagen I lumens. (ai) Photographs of device setup and basic workflow for Method 1. (aii) A rubber spacer was added to the 3D printed device to hold up the Teflon tubes on each post. F127 hydrogel seals small gaps so the collagen I does not leak through. (aiii) The rack was submerged in phosphate buffered saline, and the tubes were pushed down to remove the collagen rings and dissolve F127. (bi) Fluorescence image of primary human umbilical artery smooth muscle cells embedded in a collagen I ring. Cells are stained with calcein AM (live, green) and ethidium-homodimer I (dead, red). (bii) Image of an array of 3 mm OD and 1 mm ID hydrogel rings in a 96-well plate.

tubing to slide down the post and unmold the hydrogel ring when the spacer is removed. F127 (a polyethylene glycol (PEG)-based hydrogel) was added to seal any gaps between the tubing and the 3D printed post. We chose F127 as a sacrificial layer because it is not toxic to cells and easily dissolves once placed in a liquid such as cell culture media or phosphate buffered saline (PBS). After the F127 gelled, collagen I was added to form the ring. Once the collagen I polymerized the PDMS spacer was removed and the device was placed in PBS. The tubing was pushed down

into the gap created by the removal of the PDMS spacer to reveal the hydrogel rings which were then released into solution; the PBS dissolved the sacrificial F127 (**Figure 4.1.1 aii**). Collagen laden with primary human umbilical artery smooth muscle cells (HUASMCs) was used to form cell-laden hydrogel rings. A live/dead stain was performed with calcein AM and ethidium homodimer-1, showing the cells maintained excellent viability (**Figure 4.1.1 bi**). Further, arrays of hydrogel rings can efficiently be made with this method (**Figure 4.1.1 bii**).

The addition of endothelial cells to line the lumen allows our method to further model the structure of a human blood vessel. To achieve this, the method of creating collagen rings was adapted to make the post removable, enabling an endothelial cell suspension to be added to the lumen after gelation of the hydrogel ring (**Figure 4.1.2**). The post was removed and an endothelial cell suspension was pipetted into the lumen, after which the device was incubated for 1 h. During this incubation period, the device was rotated 180 degrees every 5 min for the first 20 min and then every 10 min for an additional 40 min to ensure distribution of cells on all sides of the lumen. The spacer was removed and the Teflon tube was pushed down to reveal the ring with endothelial cells seeded in the lumen. The cells were then incubated in a well plate with cell culture media for 24 h after which a live/dead stain was performed. Endothelial cells were viable at 24 h and were evenly distributed within the lumen (**Figure 4.1.2 b**). Imaging the hydrogel ring due to its free-standing nature can be challenging as it is suspended in liquid media. To increase the usability of this method, future work includes adding a holder to stabilize the ring without restricting its movement in three dimensions.

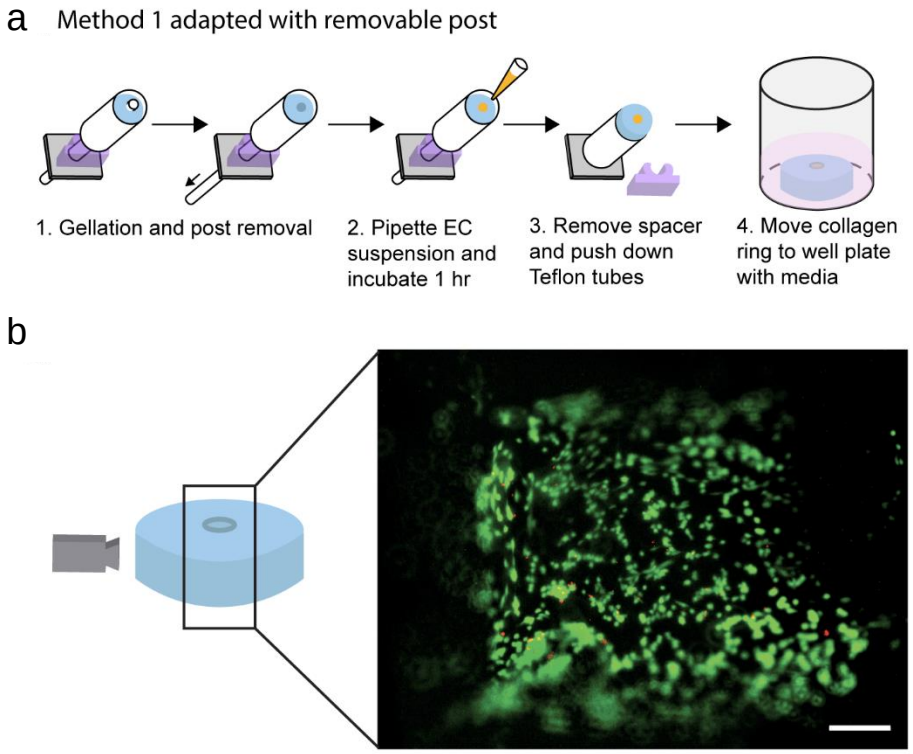

Figure 4.1.2. Addition of endothelial cells to the lumen of collagen I rings. (a) Workflow for adding the endothelial cell suspension to the gelled collagen rings. (b) Image of the lumen was taken after 24 h of cell seeding to show the viability of the endothelial cells. Cells are stained with calcein AM (live, green) and ethidium-homodimer I (dead, red). Scale bar is 100 μm.

4.1.3 Conclusion

We demonstrate that we have created a simple method for forming freestanding cell-laden hydrogel rings that can be used in a quantifiable assay for measuring dynamic change after treatment with a known vasodilator. Our goal was to create a method that does not rely on animal models or rigid devices to stabilize the lumen. Our method takes the unique approach to being freestanding which allows unrestricted movement in all three dimensions in response to vasoactive compounds. This method enables researchers to study the response of a controlled human cell-laden hydrogel ring to different inflammatory drugs or molecules, as well as study the cellular communication that is important to understanding the pathways that are activated during inflammation. So far, we have only tested the model with fasudil; additional vasodilators and vasoconstrictors would need to be tested to further validate our method for use in vasodilator and

vasoconstrictor studies. Additionally, alignment of the smooth muscle cells was not achieved in this current work. This will be a focus of future work to ensure smooth muscle cells are able to constrict and dilate the vessel mimic while in the alignment observed in blood vessels. In future work we will also work to achieve lumen size and wall thickness relevant to smaller vessels in the human body. We anticipate this can be addressed using higher resolution fabrication methods. Additionally, we will integrate these freestanding lumens with other co- and multiculture platforms to incorporate fibroblasts, smooth muscle cells, endothelial cells, and other stromal cells important for modeling disease-specific vasodilation, as well as cell types in circulating blood including leukocytes that may interact with endothelial cells and be recruited to neighboring tissue. We envision that our model will be important for studying a range of diseases such as asthma, cancer, autoimmune disease, and other diseases that have periods of induced inflammation, vasodilation, or constriction.

4.1.4 Materials and Methods

Cell culture of human umbilical artery smooth muscle cells (HUASMCs) and human umbilical vein endothelial cells (HUVECs): Human umbilical artery smooth muscle cells (HUASMCs; Cell Applications, Inc) were cultured in human smooth muscle cell growth medium (SmGM; Cell Applications, Inc) supplemented with penicillin (100 units/mL) and streptomycin (100 µg/mL). Human umbilical vein endothelial cells (HUVECs; Lonza) were cultured in endothelial cell growth medium (EGM-2; Lonza) supplemented with penicillin (100 units/mL) and streptomycin (100 µg/mL). Culture flasks were maintained at 37 °C with 5% CO2. HUASMCs between passages 4 and 8 were used; HUVECs between passages 5 and 11 were used.

Preparation of collagen I solution: HEPES buffer was prepared as 500 mM in 10X PBS and adjusted to a pH of 7.4 using NaOH pellets. The HEPES buffer was then thoroughly mixed with high concentration collagen I (8–10 mg/mL; Corning) in a 1:9 ratio of HEPES to collagen.

Encapsulation of HUASMCs in collagen I hydrogel: HUASMCs were trypsinized and resuspended at a concentration of 5×10^6 cells/mL in growth medium (SmGM). The cell suspension was then added to the neutralized collagen solution for a final concentration of 1×10^6 cells/mL and 6 mg/mL collagen I.

Fabrication of device to mold hydrogel rings (**Figures 4.1.1** and **4.1.2**): Molds were designed using Solidworks (Dassault Systems, Waltham, MA). Hydrogel ring molds were fabricated using a Form 2 SLA 3D printer (Formlabs, Somerville, MA) using Clear V4 resin (Formlabs) with a Z resolution of 0.05 mm. After printing, molds were cleaned in a FormWash with isopropyl alcohol (IPA) for 10 min, followed by a second wash with fresh IPA for 10 min. Molds were then dried using compressed air and cured under UV (FormCure, Formlabs) for 30 min at 60 °C. A 3.5 mm thick polydimethylsiloxane (PDMS) spacer was made by milling a polystyrene mold (Datron Neo) and pouring PDMS (Sylgard™ 184, Dow) in a 1:8 ratio. The PDMS was left to cure at room temperature for 48 h. Prior to use for cell culture, molds were sprayed with 70% ethanol, air dried in a biosafety cabinet, and irradiated with UV light for 15 min.

Hydrogel ring fabrication (**Figure 4.1.1** and **4.1.2**): Teflon tubing (McMaster Carr) with an inner diameter of 3.175 mm and an outer diameter of 6.35 mm was cut to 1 cm in length, sonicated in with 70% ethanol for 30 min, air dried, and then transferred onto the 3D printed molds with PDMS spacers. A 20% solution of Pluronic® F127 (P2443–1KG; referred to as F127) (Sigma Aldrich) was pipetted into the mold for the rings and then removed, leaving a thin layer of F127 and filling any gaps between the 3D printed device and the Teflon tubing. The devices were placed in a box with Kimwipes saturated in 1X PBS to prevent evaporation of any hydrogel. The box was placed in a 37°C incubator for 5 min to fully set the F127. A tube of collagen was warmed up to room temperature to prevent it from dissolving the F127. The collagen was then pipetted into the molds, the molds placed back in the box with PBS, and incubated for 1 h. To remove the collagen rings the PDMS spacer was removed and the device was submerged in 1X PBS. The Teflon tube was pushed down and the collagen rings were gently removed from the 3D printed post using tweezers

or by gently shaking the device. They were then transferred to a 24-well plate with 500 µL of 1X PBS in each well.

Addition of endothelial cells to hydrogel rings (**Figure 4.1.2**): A 3D printed mold was generated with a hole rather than a post. Teflon tubing (McMaster Carr) was run through each mold to act as a retractable post. Collagen I was added to the mold carefully to avoid bubbles and incubated for 1 h, as outlined above. After 1 h of incubation, the BioAssay Dish containing hydrogel ring molds was removed from the incubator and brought into a biosafety cabinet. The retractable Teflon tubing was then drawn down to reveal a lumen while the hydrogel rings remained in the mold. Approximately 5 µL solution of HUVECs (1×10^6 cells/mL) was carefully pipetted into the lumen for each ring. The devices were rotated 180° every 5 min for the first 20 min and then 180° every 10 min for the following 40 min to ensure even distribution of HUVECs within the lumen. After 1 h of incubation and rotation, hydrogel rings were removed in a solution of PBS and transferred to a well plate as described above. Each ring was incubated in 60 µL of EGM-2 media for 24 h. At the 24 h mark rings were washed with 1X PBS and stained with calcein AM (C3100MP, Fisher Scientific) and ethidium-homodimer 1 (E1169, Fisher Scientific) for 30 min at 37 °C, rinsed with 1X PBS, and imaged using a fluorescence microscope (Zeiss Axiovert 200 and an Axiocam 503 mono camera; Carl Zeiss AG, Oberkochen, Germany).

4.1.5 References

1. G. Horvath and A. Wanner, Inhaled corticosteroids: effects on the airway vasculature in bronchial asthma, *Eur. Respir. J.*, 2006, **27**, 172–187.
2. K. Duval, H. Grover, L. H. Han, Y. Mou, A. F. Pegoraro, J. Fredberg and Z. Chen, Modeling Physiological Events in 2D vs. 3D Cell Culture, *Physiology (Bethesda).*, 2017, **32**, 266–277.
3. R. Edmondson, J. J. Broglie, A. F. Adcock and L. Yang, Three-Dimensional Cell Culture Systems and Their Applications in Drug Discovery and Cell-Based Biosensors, *Assay Drug Dev. Technol.*, 2014, **12**, 207.
4. M. W. Tibbitt and K. S. Anseth, Hydrogels as Extracellular Matrix Mimics for 3D Cell Culture, *Biotechnol. Bioeng.*, 2009, **103**, 655.
5. L. L. Bischel, K. E. Sung, J. A. Jiménez-Torres, B. Mader, P. J. Keely and D. J. Beebe, The importance of being a lumen, *FASEB J.*, 2014, **28**, 4583.
6. F. Pampaloni, E. G. Reynaud and E. H. K. Stelzer, The third dimension bridges the gap between cell culture and live tissue, *Nat. Rev. Mol. Cell Biol.*, 2007, **8**, 839–845.
7. W. Jia, P. S. Gungor-Ozkerim, Y. S. Zhang, K. Yue, K. Zhu, W. Liu, Q. Pi, B. Byambaa, M. R. Dokmeci, S. R. Shin and A. Khademhosseini, Direct 3D bioprinting of perfusable vascular

constructs using a blend bioink, *Biomaterials*, 2016, **106**, 58–68.
8. F. Marceau, D. deBlois, E. Petitclerc, L. Levesque, G. Drapeau, R. Audet, D. Godin, J. F. Larrivée, S. Houle, T. Sabourin, J. P. Fortin, G. Morissette, L. Gera, M. T. Bawolak, G. A. Koumbadinga and J. Bouthillier, Vascular smooth muscle contractility assays for inflammatory and immunological mediators, *Int. Immunopharmacol.*, 2010, **10**, 1344–1353.
9. Q. Pi, S. Maharjan, X. Yan, X. Liu, B. Singh, A. M. van Genderen, F. Robledo-Padilla, R. Parra-Saldivar, N. Hu, W. Jia, C. Xu, J. Kang, S. Hassan, H. Cheng, X. Hou, A. Khademhosseini and Y. S. Zhang, Digitally Tunable Microfluidic Bioprinting of Multilayered Cannular Tissues, *Adv. Mater.*, , DOI:10.1002/ADMA.201706913.
10. Y. Zhang, Y. Yu, A. Akkouch, A. Dababneh, F. Dolati and I. T. Ozbolat, In Vitro Study of Directly Bioprinted Perfusable Vasculature Conduits, *Biomater. Sci.*, 2015, **3**, 134.
11. H. Tseng, J. A. Gage, W. L. Haisler, S. K. Neeley, T. Shen, C. Hebel, H. G. Barthlow, M. Wagoner and G. R. Souza, A high-throughput in vitro ring assay for vasoactivity using magnetic 3D bioprinting, *Sci. Reports 2016 61*, 2016, **6**, 1–8.
12. D. B. Badesch, Clinical trials in pulmonary hypertension, *Annu. Rev. Med.*, 1997, **48**, 399–408.
13. D. Impellizzeri, G. Bruschetta, E. Esposito and S. Cuzzocrea, Emerging drugs for acute lung injury, *Expert Opin. Emerg. Drugs*, 2015, **20**, 75–89.
14. H. H. Leuchte, C. Baezner, R. A. Baumgartner, D. Bevec, G. Bacher, C. Neurohr and J. Behr, Inhalation of vasoactive intestinal peptide in pulmonary hypertension, *Eur. Respir. J.*, 2008, **32**, 1289–1294.
15. P. W. Alford, A. P. Nesmith, J. N. Seywerd, A. Grosberg and K. K. Parker, Vascular smooth muscle contractility depends on cell shape, *Integr. Biol. (Camb).*, 2011, **3**, 1063–1070.
16. C. E. Fernandez, R. W. Yen, S. M. Perez, H. W. Bedell, T. J. Povsic, W. M. Reichert and G. A. Truskey, Human Vascular Microphysiological System for in vitro Drug Screening, *Sci. Reports 2016 61*, 2016, **6**, 1–14.
17. E. S. Hald, K. E. Steucke, J. A. Reeves, Z. Win and P. W. Alford, Long-term vascular contractility assay using genipin-modified muscular thin films, *Biofabrication*, DOI:10.1088/1758-5082/6/4/045005.
18. Y. Jung, H. Ji, Z. Chen, H. Fai Chan, L. Atchison, B. Klitzman, G. Truskey and K. W. Leong, Scaffold-free, Human Mesenchymal Stem Cell-Based Tissue Engineered Blood Vessels, *Sci. Reports 2015 51*, 2015, **5**, 1–9.
19. K. E. Steucke, P. V. Tracy, E. S. Hald, J. L. Hall and P. W. Alford, Vascular smooth muscle cell functional contractility depends on extracellular mechanical properties, *J. Biomech.*, 2015, **48**, 3044.
20. K. L. Manning, J. Feder, M. Kanellias, J. Murphy and J. R. Morgan, Toward Automated Additive Manufacturing of Living Bio-Tubes Using Ring-Shaped Building Units, *SLAS Technol.*, 2020, **25**, 608–620.
21. H. A. Strobel, E. L. Calamari, B. Alphonse, T. A. Hookway and M. W. Rolle, Fabrication of Custom Agarose Wells for Cell Seeding and Tissue Ring Self-assembly Using 3D-Printed Molds, *J. Vis. Exp.*, 2018, **2018**, 56618.
22. U. N. Lee, X. Su, D. J. Guckenberger, A. M. Dostie, T. Zhang, E. Berthier and A. B. Theberge, Fundamentals of rapid injection molding for microfluidic cell-based assays, *Lab Chip*, 2018, **18**, 496–504.
23. A. Spiers and N. Padmanabhan, A guide to wire myography, *Methods Mol. Med.*, 2005, **108**, 91–104.

4.2 Injection molded open microfluidic well plate inserts for user-friendly coculture and microscopy

Reproduced in part from J.H. Day, T.M. Nicholson*, X. Su, T.L. van Neel, I. Clinton, A. Kothandapani, J. Lee, M.H. Greenberg, J.K. Amory, T.J. Walsh, C.H. Muller, O.E. Franco, C.R. Jefcoate, S.E. Crawford, J.S. Jorgensen, A.B. Theberge, "Injection molded open microfluidic well plate inserts for user-friendly coculture and microscopy." Lab on a Chip,* ***2020****, 20, 107.*
** Equal contribution*

JHD, TMN, XS, and IC developed and validated device operation, conducted cell culture experiments, evaporation control, and microscopy protocols. JHD designed and fabricated devices. TLvN performed, analyzed, and wrote about diffusion characterization shown in ***Figure 4.2.4****. TMN, JKA, TJW, and CHM designed and executed human primary testis culture experiments. AK, JL, CRJ, and JSJ designed, performed, analyzed, and wrote about smFISH experiments. MHG, OEF, and SEC designed, performed, analyzed, and wrote about prostate cancer-adipocyte coculture experiment. JHD, TM, and ABT designed overall study and wrote manuscript with all authors revising.*

Abstract: Open microfluidic cell culture systems are powerful tools for interrogating biological mechanisms. We have previously presented a microscale cell culture system, based on spontaneous capillary flow of biocompatible hydrogels, that is integrated into a standard cell culture well plate, with flexible cell compartment geometries and easy pipet access. Here, we present two new injection molded open microfluidic devices that also easily insert into standard cell culture well plates and standard culture workflows, allowing seamless adoption by biomedical researchers. These platforms allow culture and study of soluble factor communication among multiple cell types, and the microscale dimensions are well-suited for rare primary cells. Unique advances include optimized evaporation control within the well, manufacture with reproducible and cost-effective rapid injection molding, and compatibility with sample preparation workflows for high resolution microscopy (following well-established coverslip mounting procedures). In this work, we present several use cases that highlight the usability and widespread utility of our platform including culture of limited primary testis cells from surgical patients, microscopy readouts including immunocytochemistry and single molecule fluorescence *in situ* hybridization (smFISH), and coculture to study interactions between adipocytes and prostate cancer cells.

4.2.1 Introduction

An important goal of microscale cell culture systems is their translation and widespread adoption into everyday biomedical research.[1] While the promise of microscale cell culture systems in biomedical research has been recognized for the past two decades, these technologies have only recently become well-poised for widespread adoption by biomedical researchers.[2,3] 'Open' microfluidic devices, which contain channels with at least one air-liquid interface, have contributed to increased accessibility.[4]

Open microfluidics allows precise patterning of liquids and cell suspensions via spontaneous capillary flow.[5–8] We have recently presented a 3D-printed well plate insert for cell culture, the Monorail Device, that utilizes spontaneous capillary flow to pattern biocompatible hydrogels on a surface, creating hydrogel walls that partition the well into separate chambers for cell culture.[9] This platform enables a range of cell culture compartment geometries with physical partitioning of different cell types and the ability to study soluble factors exchanged in coculture through the hydrogel wall.[9] Key advantages of this platform include compatibility with traditional cell culture platforms (e.g., well plates) so that cells can be grown on commercially available cell culture treated surfaces, ease of pipetting due to open microfluidic design, and the ability to pattern various shapes. Lee et al. presented a different platform based on similar principles, using injection molded polystyrene to create a 3D coculture system in the form of a 96-well plate; in this case, the entire well plate structure containing the fluidic features was manufactured as a single plastic structure, and the well plate floor was subsequently created by bonding adhesive tape to the injection molded structure. This innovative device enables a number of experimental designs involving 3D culture, however it cannot be used for 2D culture experiments due to the nature of the adhesive floor on which cells would be cultured.[10,11]

Both of these examples represent important advances in translating microscale cell-culture systems into formats that are easily utilized for biological applications. However, microscale cell culture platforms based on open and suspended microfluidics continue to have

several challenges for cell culture applications that may limit widespread adoption by biomedical researchers. These challenges include evaporation control at the air-liquid interface, variability from device fabrication and user operation, and difficulty interfacing with standard workflows for high resolution microscopy which involve culturing cells on coverslips and subsequent mounting on glass slides. Here, we present two new open microfluidic devices based on our previously established platform.[9] These devices retain the advantages of the original iteration—easy integration with well plates that are familiar to biomedical researchers, flexible geometric patterning of biocompatible hydrogels, and pipet accessibility. Distinct advantages demonstrated herein include simple and effective evaporation control strategies, manufacture with rapid injection molding, and compatibility with high resolution microscopy; these three considerations are reviewed in the following paragraphs.

Compared to conventional cell culture vessels such as flasks, petri dishes and well plates, microscale systems have a higher surface area to volume ratio, leading to less cell culture media per cell.[12] The resulting cell stress can be mitigated by frequent media changes and decreased cell seeding density, but evaporation remains an important concern, and is of particular importance for microscale cell culture systems that are suited for rare, sensitive cell types affected by changes in osmolarity.[12–15] The full pipet accessibility that makes our devices easier to use also allows for more evaporation due to the larger air-liquid interfaces present in the pipet-accessible culture chambers. The combination of low culture volume and pipet accessibility makes evaporation a major consideration in this work and is addressed either in the standard operating procedure for cell culture in the device (Monorail1) or the device design itself (Monorail2).

A number of strategies have been employed to attenuate evaporation, typically by adding surplus water near the culture to keep the partial pressure of water vapor near equilibrium above the culture; such strategies include reservoirs of water on-chip, surrounding cultureware with wetted Kimwipes™, and placing culture-ware in a larger secondary containment unit.[9,13] Oil has

also been employed to mitigate evaporation by covering aqueous liquids.[8] Some of these strategies can be cumbersome in the hands of researchers that are not accustomed to microfluidic devices and may pose contamination or spillage risks for multiday cultures. In this work, we present two approaches to mitigate evaporation in our devices that are conducive to cell viability and do not require placement of the entire well plate in a larger secondary evaporation control vessel.

Widespread adoption of microscale cell culture systems in biomedical applications is challenging because of the need for low-cost production, reproducible manufacturing, and the ability to iterate on designs. Common methods for microfluidic device fabrication, which include micro-machining,[16] soft lithography,[17] hot embossing,[18] and 3D printing,[19] are better suited for early-stage prototyping than mass production. Injection molding is the gold standard for mass manufacturing and offers high reproducibility and fast manufacturing times.[20,21] Until recently, the downside of injection molding had been the high cost associated with producing complex high-quality steel molds. Rapid injection molding, as defined by Lee et al.,[22] uses computerized workflows and less robust molds (often made from aluminum) to reduce mold costs (typically ~$2,000–4,000 per mold vs. ~$50,000 or more per mold in traditional injection molding). Microscale cell culture systems are now poised for high volume use in biological and clinical applications.[22]

An important challenge for adoption of microscale cell culture systems in biomedical research is compatibility with high resolution imaging. In contrast to Transwell® inserts, a common commercially available platform for segregated coculture in which one cell type is cultured on a semipermeable membrane in an insert above the well plate, our device allows coculture of separated populations of cells on the same plane, therefore conferring the ability to view both populations under a microscope at the same time. The ability to view all cells is useful for monitoring the cells during the culture period (to observe confluence, morphology, and overall health of the culture). The single coverslip coculture also greatly simplifies sample preparation

compared to Transwell® workflows, which require the user to cut the membrane out of the Transwell® with a scalpel and fasten it to a glass slide. Additionally, our platform enables triculture (whereas Transwells® are limited to coculture), and the material of the Transwell® membrane is an added variable that can affect cell culture experiments because some cell types adhere differently to Transwells® than glass or tissue culture treated plastic. Finally, imaging is a useful endpoint readout; we demonstrate that our device enables coculture on glass coverslips, which can be removed from the device after the culture period and mounted on a glass slide for high resolution immunocytochemistry and single molecule fluorescence in situ hybridization (smFISH), important endpoints in biomedical research.[23]

Taken together, we present two injection molded microscale coculture devices specifically developed for easy use by biomedical researchers. Our devices are manufactured from polystyrene, which is traditionally used for cell culture in biology laboratories.[24,25] We discuss key aspects of device design and manufacture, and present several use cases, including culture of limited primary testis cells from surgical patients and coculture to study interactions between adipocytes and prostate cancer cells; these use cases highlight the accessibility of our platform. Importantly, we have manufactured several thousand devices and sent them to eight independent biology ‘test labs,’ where they are used for wide-ranging applications including lymph, prostate, and microbial signaling. The work presented was collected in three independent laboratories—with devices and protocols shipped from the University of Washington to the Jorgensen lab in Comparative Biosciences at the University of Wisconsin-Madison (MA-10 cell culture and smFISH imaging) and the Crawford lab in Surgery at NorthShore HealthSystem, University of Chicago (prostate cancer-adipocyte signaling), demonstrating the robustness and accessibility of our culture platform.

4.2.2 Device overview: segregated coculture on a well plate surface

In previous work, we introduced a 3D printed platform that uses hydrogel walls patterned on a plastic or glass surface to make unique segregated coculture systems integrated into standard cell culture well plates for mammalian cell culture; we also demonstrated proof-of-concept soluble factor exchange through hydrogel using an established microbial coculture system.[9] This work focuses on essential developments to translate this platform to biomedical laboratories, including engineering design modifications that enable manufacturing by injection molding, features for preventing evaporation, and the development of workflows that enable high resolution imaging at the end of culture. We designed two hydrogel patterning devices for culture of multiple cell types (referred to as the "Monorail1 device" and the "Monorail2 device"). We used 3D printing and computer numerical control (CNC) milling to prototype the platforms and manufactured the final devices with rapid injection molding using Protolabs. As shown in **Figure 4.2.1**, the Monorail1 device fits securely into the well of a 12-well plate and enables segregated coculture of up to three cell types. Pressure struts are features of the device that apply pressure to the walls of the well, allowing the well plate to be handled or inverted without dislodging the device. As shown in **Figure 4.2.1**, three cell culture chambers are delineated by hydrogel walls that encompass the perimeter of the cell culture chambers. When a device is placed in the well of a 12-well plate, the foot of the device (which runs around the perimeter of the device) holds the rails 250 μm above the floor of the well. A hydrogel precursor solution is loaded into the loading port of the device and flows spontaneously in the 250 μm gap between the rails of the device and the floor of the well plate. Hydrogel precursor solution flows and is confined to the space under the rail. As in our prior work,[9] we used rails with a trapezoidal cross-section to induce pinning of the fluid on the edges of the bottom of the rail. This geometry prevents the hydrogel precursor solution from wetting the vertical faces of the device. After completion of flow, the hydrogel solution can be polymerized to yield a selectively permeable barrier that demarcates a set of chambers in which cells can be cultured (**Figure 4.2.1**). Cells seeded on either side of the hydrogel wall are physically separated, as shown

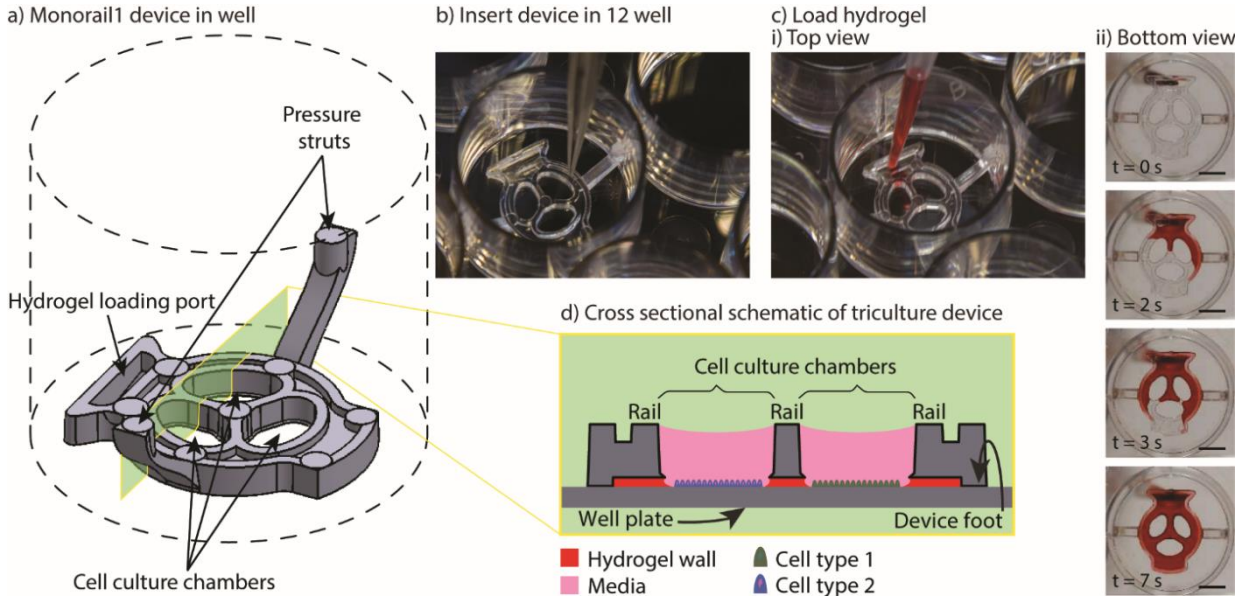

Figure 4.2.1. Overview of Monorail1 device design features and operation. a) Monorail1 device (dashed lines represent the well of a 12-well cell culture plate). b) The device is loaded into the well of a standard 12-well cell culture plate using forceps. c) Hydrogel is loaded into the hydrogel loading port with a standard pipet, as seen from i) above the well plate or ii) below the well plate. Hydrogel is tinted with red dye for visualization purposes. ii) Bottom view images of the gel-precursor solution patterning progression at four timepoints. Scale bars: 5 mm d) Schematic of the device in cross-section depicting distinct cell types (blue, green) in different culture chambers that are separated by a hydrogel wall formed between the bottom of the rail and the base of the well.

schematically in **Figure 4.2.1 d**, while soluble factors (e.g., small molecules, proteins) diffuse through the hydrogel wall. Up to three distinct cell populations can be seeded into different cell culture chambers. This platform can be used with several hydrogels, including collagen I and matrigel.[9] In the present work, we developed protocols for use of low gelling temperature agarose, recommended instead of collagen when working with primary cells isolated from tissues digested with collagenase because residual collagenase can degrade the collagen wall.

4.2.3 Evaporation controls for microscale culture

We optimized a protocol to mitigate evaporative loss in the Monorail1 device without the need for secondary containment. We cultured testis cells (MA-10) in the device and used cell viability as a qualitative metric to assess evaporation. Negligible evaporation was inferred in the setting of high cell viability. We found that cells were nearly 100% viable after 24 h in culture when

the four corner wells, as well as the spaces between the wells, were used as reservoirs for additional water, as shown in **Figure 4.2.2 a**. If the user loads fewer than eight devices into a well plate, we recommend adding additional water to vacant wells. The eight-device layout maximizes the number of usable wells in a well plate while keeping cell viability high. Other layouts showed dispersed pockets of dead cells throughout the well plate, likely due to evaporation in the microculture system (**Figure B4**). Multiple cell types were successfully cultured and showed comparable viability in the Monorail1 device (**Figure 4.2.2 c–d**). Without the need for secondary

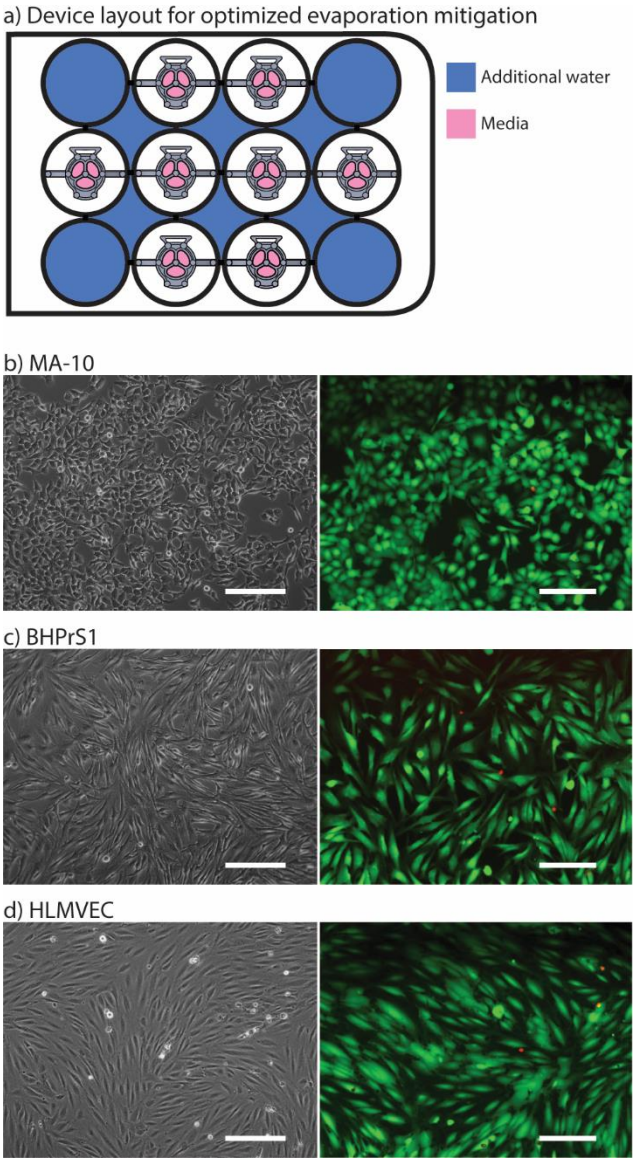

Figure 4.2.2. Adding water to corner wells and interwell spaces mitigates evaporation. a) Schematic of Monorail1 device layout in 12-well plate that optimizes evaporation control. Blue color indicates well or interwell space that is filled with water to mitigate evaporation. b) Testis cells (MA-10), c) benign human prostate stromal cells (BHPrS1), and d) primary human lung microvascular endothelial cells (HLMVEC) were cultured in the Monorail1 device for 24 h in the layout shown in a. Left images are phase contrast microscopy showing expected cell morphology. Right images show results of live (green) and dead (red) cell staining performed at 24 h. Fluorescence images are representative of the lowest viability field of view that was observed. Scale bars: 200 μm.

containment to address evaporation concerns, this device offers a simple platform for coculture and triculture experiments in a form factor that is familiar to biomedical researchers.

We also developed a microscale coculture device with a smaller cell culture area and in-device evaporation control. This second device (referred to as the Monorail2 device) was conceived to enable coculture experiments with rare cells, or cultures of cells that require soluble factors from supporting cells to maintain viability in vitro (**Figure 4.2.3**). To address this need, the Monorail2 device features a smaller central cell culture region (~3 mm^2) flanked by two larger outer culture regions (~8 mm^2 each), which hold 8 and 20 µL of media, respectively. **Figure 4.2.3** shows details of the Monorail2 device, which was designed with a built-in media reservoir. The media reservoir surrounds the periphery of the cell culture chambers and is segregated by a pinning ridge. When the device is secured in the bottom of the well, there is a thin void space under the device, created by imperfections in the plastic surfaces of the device and well (labelled "contact area" in **Figure 4.2.3 aii**). When fluid evaporates from the cell culture chambers, media flows under the device from the media reservoir to the culture chambers. Importantly, we designed the device to limit diffusion of soluble factors secreted by cells in the culture chambers (or drug treatments applied in the culture chambers) to the media reservoir by making the "contact area" as large as possible within the footprint of the well. The large contact area increases the diffusion distance, mitigating diffusion on the timescale of cell culture experiments. Additionally, the contact area was polished (on the mold) to be as flush as possible with the floor of the well, further mitigating diffusion under the contact area. As shown in **Figure 4.2.3 aii**, hydrogel precursor solution floods under the contact area when it is loaded into the device, further mitigating diffusive loss of soluble factors to the media reservoir; however, the relatively high viscosity of most hydrogels precludes them from completely filling this space. Because the concentration of soluble factors is important in biological experiments, we characterized diffusion from the cell culture chambers to the media reservoir. The diffusion of a 10 kDa fluorophore, which was used as a model soluble factor, is limited to 2.4± 0.2% after a 24 h incubation (mean ± standard deviation

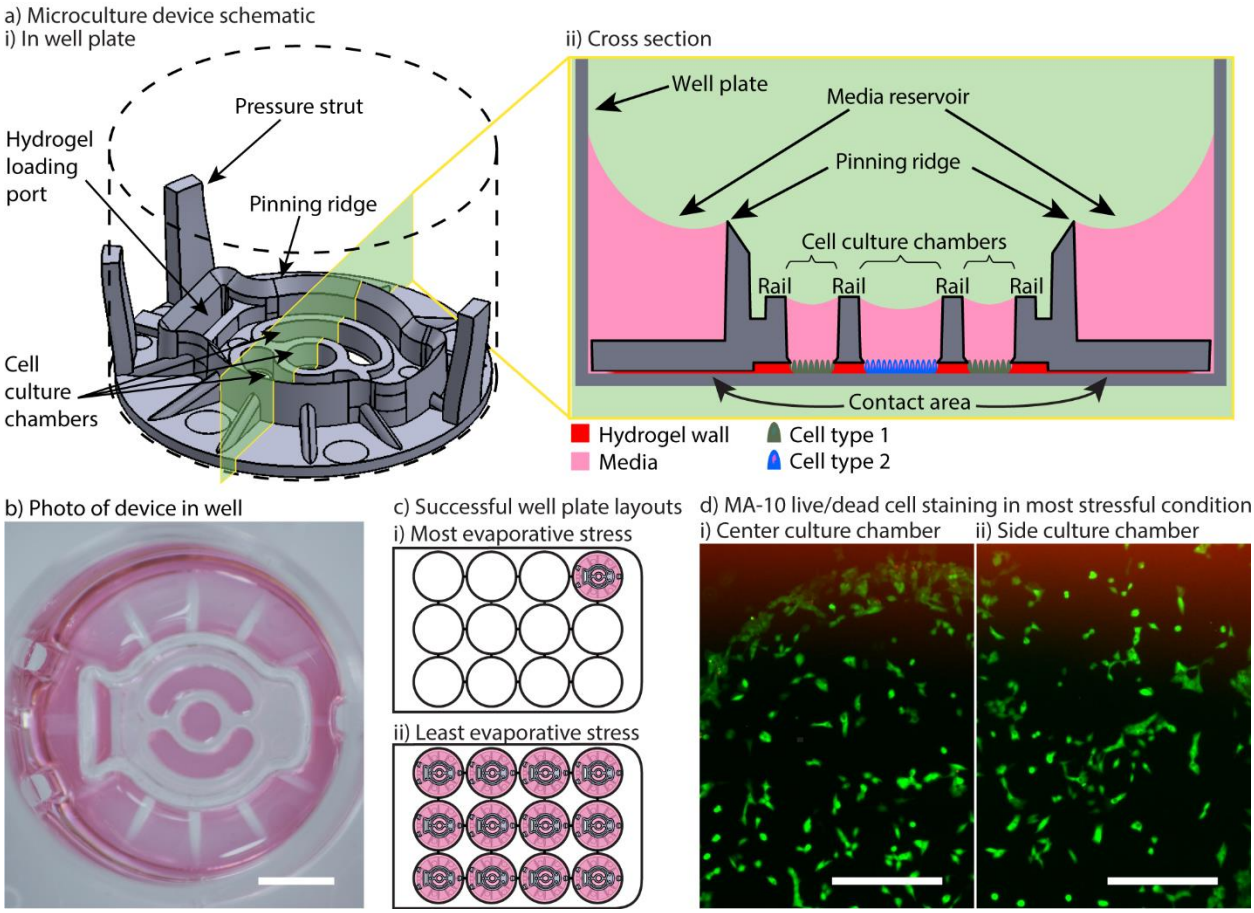

Figure 4.2.3. Monorail2 device design features minimize evaporative stress on cells in culture. a) i) Monorail2 device schematic (dashed lines represent the well plate of a 12-well cell culture plate). ii) Cross-sectional schematic of the Monorail2 device when loaded in a 12-well plate with media loaded into cell culture chambers. The media reservoir exists on the peripheries of the device, and is kept from spilling over the top of the device into the cell culture chambers by a pinning ridge that runs around the cell culture chambers and loading port. b) Photo of a Monorail 2 device in a 12-well plate loaded with media. Scale bar: 5 mm. c) Schematics of well plate layout experiment to test evaporation. d) Testis cells (MA-10) were cultured in the Monorail2 device for 24 h, and live (green) and dead (red) staining was performed. High viability (nearly 100%) was observed in all devices and in all configurations. Representative images of cells in the center and side cell culture chambers are shown. Scale bars: 200 μm.

for three replicates). Therefore, soluble factor diffusion from the cell culture chambers to the media reservoir is minimal, maintaining the benefit of the low volumes when pharmacologic manipulations are used in experiments.

To validate the mitigation of evaporative water loss in the Monorail2 device, we used the aforementioned cell viability readout and observed little to no cell death in any part of the device, irrespective of the number of devices in the well plate or the position of a device within the well

plate. It is known that using a single well of a well plate offers the most challenging condition for minimizing evaporation. This is because each well of a well plate that contains evaporating water will contribute some water vapor to the other wells of the plate. Therefore, we performed cell viability experiments in well plates with devices in every well (easiest condition for evaporation control) and well plates with only one device in the corner (most challenging condition for evaporation control). As shown in **Figure 4.2.3**, excellent viability was observed in the most challenging evaporative condition. Of note, when using this device, it is essential to use the device as designed (i.e., placing media in the media reservoir); without media in the media reservoir, fluid will flow from the cell culture chambers to the outer ring which is incompatible with cell viability.

Some experiments utilizing primary mammalian cells require the use of enzymatic tissue digestion as a step prior to cell isolation and/or purification. We observed utilizing a collagenase digestion step could lead to digestion of the collagen hydrogel walls after 24 h in culture; therefore, we developed a protocol for an alternative hydrogel, low gelling temperature agarose. **Figure 4.2.4** shows that diffusion of molecules of 75 kDa, 10 kDa and 527 Da size is comparable with collagen or low temperature gelling agarose walls. The Monorail2 device is particularly beneficial for culture of small numbers of cells in small media volumes, or coculture of rare cells with supporting cells to study paracrine interactions. It is readily adopted by biomedical researchers because it is a well plate compatible and pipet accessible format, and has the potential to simplify a wide range of difficult coculture conditions.

4.2.4 Device applications in biological studies

We are currently working in collaboration with the University of Washington Male Fertility Laboratory to culture primary human testis cells in the Monorail2 device. Cells are collected from residual tissues after patients undergo testicular sperm aspiration (TESA) or testicular sperm extraction (TESE), surgical protocols commonly performed to collect sperm for in vitro fertilization

or intracytoplasmic sperm injection. For these experiments, the tissues are removed in the operating room and processed in the adjacent clinical laboratory at the Male Fertility Laboratory;

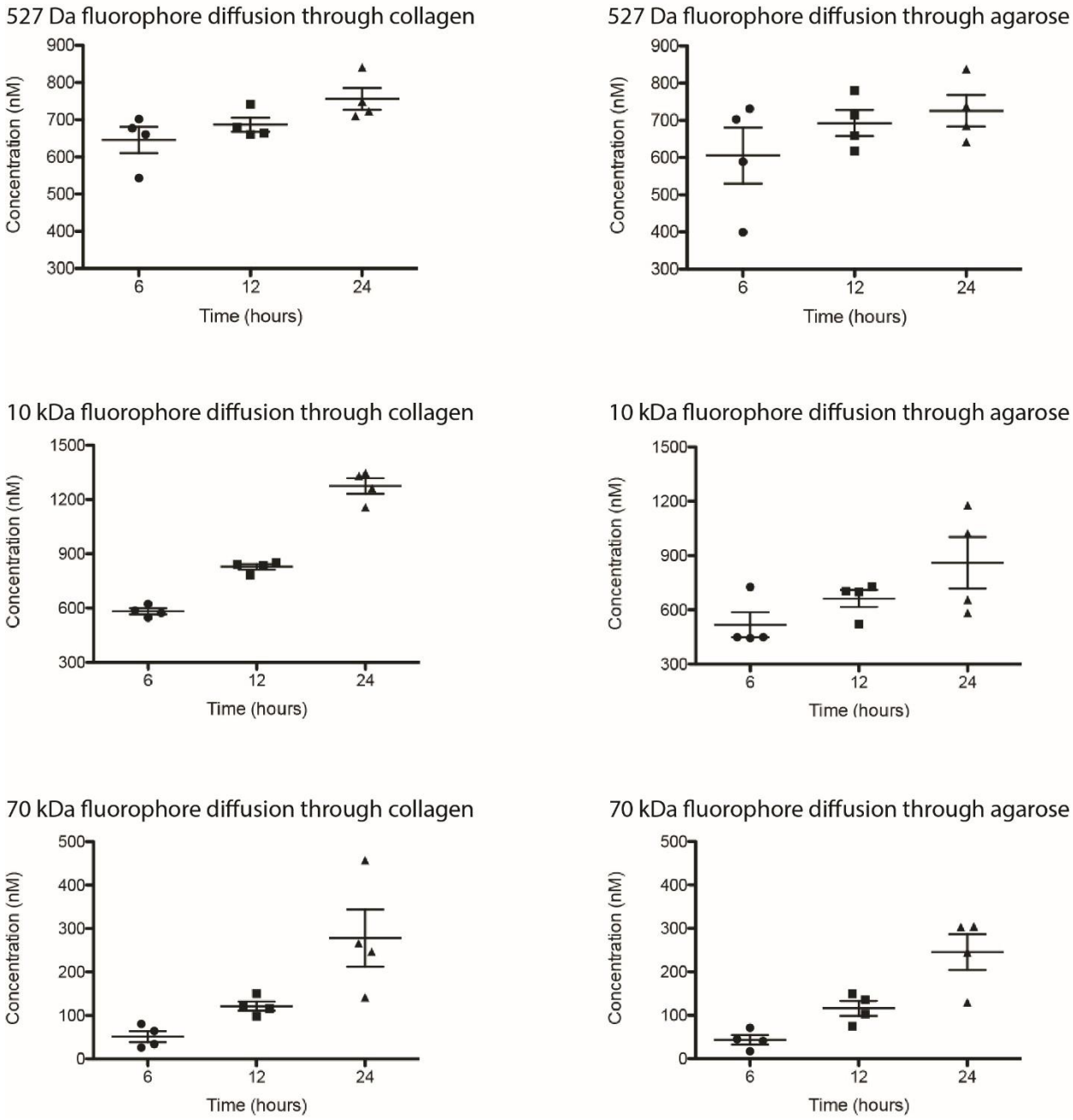

Figure 4.2.4. Diffusion of fluorescent dyes through collagen and agarose gel walls in Monorail2 devices. Concentrations of 527 Da (top row), 10 kDa (middle row), or 70 kDa (bottom row) fluorophore in receiving chambers of microculture device after 6, 12, and 24 h. Gel walls through which diffusion occurred were made of either type I collagen (left column) or agarose (right column). Each plotted point represents a pooled sample from both outer chambers in a Monorail2 device. Error bars represent standard deviation.

the ability to use our Monorail2 device in a clinical laboratory underscores the ease with which the device can be setup and operated. Here, we show preliminary results indicating that our Monorail2 device enables culture and maintenance of mixed interstitial testis cells isolated from testicular sperm extraction (**Figure 4.2.5**). Due to the low cell yield from this TESE, we only recovered cells sufficient to seed the central chamber of five Monorail2 devices, underscoring the importance of the microscale culture dimensions. As collagenase was used for enzymatic digestion, we used low gelling temperature agarose to make the hydrogel wall. Phase contrast images were taken of fixed cells after four and seven days in culture (**Figure 4.2.5**). In future work, we are developing protocols to isolate, characterize, and culture Leydig cells, a rare cell type that produces steroid hormones, including testosterone, in the testis (which will be cultured in the center chamber of the Monorail2 device) with Sertoli cells and other supporting cell types (which will be cultured in the outer chambers), paralleling our prior work with mouse fetal Leydig and Sertoli cells.[26]

Obesity is known to synergize with several different types of cancer to yield higher likelihoods for tumorigenesis in cancer-free patients and enhanced tumor growth and metastasis rates in patients with cancer.[27] As such, adipocytes have received growing attention in cancer

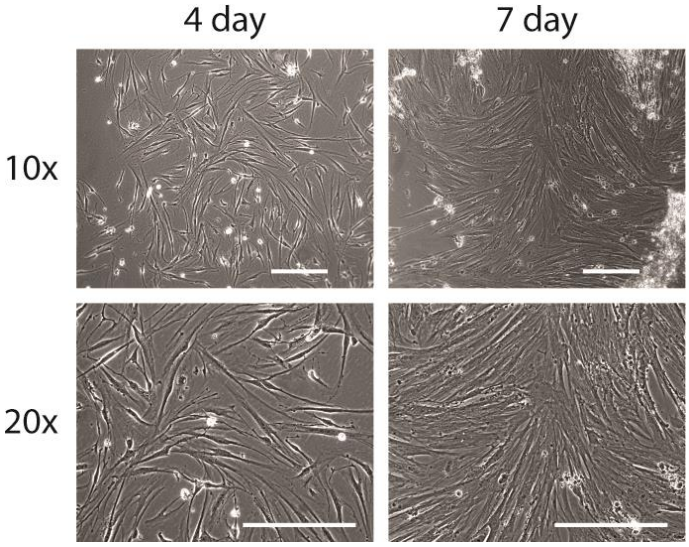

Figure 4.2.5. Human primary testis cells cultured in the microculture device. Cells were maintained for four days (left column) and seven days (right column), showing the ability to culture limited numbers of primary cells isolated from surgical procedures. Images are representative of three replicate devices (at day four) and two replicate devices (at day seven). Scale bars: 200 μm.

research for their role in promoting cancer progression.[28] In addition, inhibition of lipogenesis in prostate cancer cells has been shown to suppress tumor growth.[29] The role of paracrine signaling between cancer cells and adipocytes has been studied, but more work needs to be done to parse out the mechanisms by which adipocyte signaling influences malignant tumors.[30] In this work, we show preliminary data from a model of prostate cancer that is influenced by adipocyte signaling. We used the Monorail1 device to coculture prostate cancer (PC-3) cells with adipocytes (3T3-L1). Given that lipid metabolism is important to the maintenance of prostate cancer energy homeostasis, we quantified lipid droplet area in PC-3 cells in the presence and absence of 3T3-L1 cells cultured in a neighboring chamber of the Monorail1 device. **Figure 4.2.6** shows an increased area per lipid droplet in PC-3 cells cocultured with 3T3-L1 cells compared to monoculture, supporting the hypothesis that 3T3-L1 cells secrete soluble factors that augment lipid droplet induction in PC-3 cells.

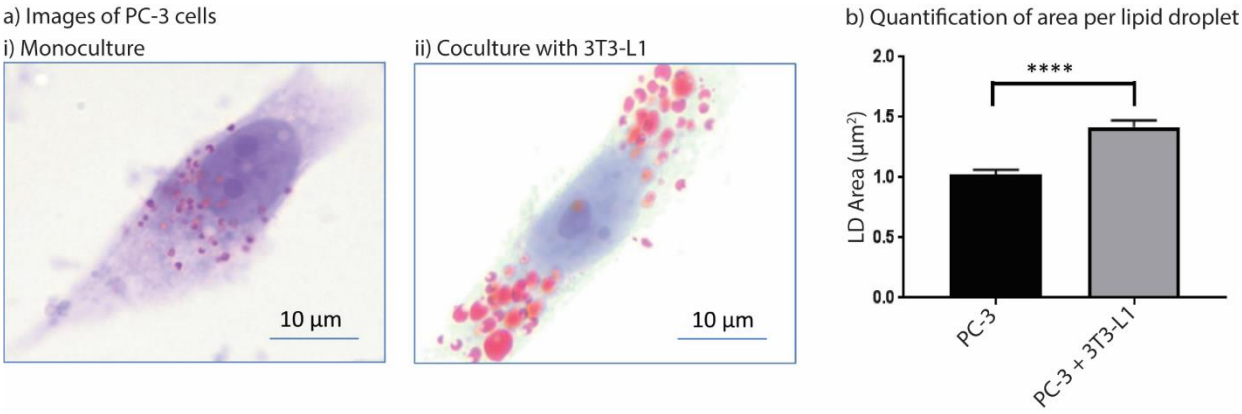

Figure 4.2.6. Coculture of prostate cancer cells (PC-3) with adipocytes (3T3-L1) leads to increased lipid droplet area in prostate cancer cells. a) Representative images of PC-3 cells in monoculture (i) and cocultured with 3T3-L1 (ii) (Oil-Red-O, red; counterstained with hematoxylin and lithium carbonate, blue). b) Quantification of lipid droplet area in PC-3 cells cultured alone or with 3T3-L1 cells. Lipid droplets were quantified from 15 high power (100x) fields of view for both monoculture and coculture groups. Data plotted are from one experiment and are representative of data collected across two independent experiments. Error bars represent the standard error of the mean.

4.2.5 Conclusion

In this work, we developed two open microfluidic well plate inserts for coculture that are compatible with mass production via injection molding. These devices seamlessly integrate into standard well plate monoculture procedures, enabling more advanced experimentation without drastically altering experimental conditions. By manufacturing our devices with rapid injection molding, we have been able to disseminate them to numerous biology laboratories for diverse coculture applications. We find that biology laboratories with no prior microfluidics experience can readily use our devices for advanced coculture applications, including use with human primary cells coming from patients, by first following a simple protocol that they use to train and "test their hands" with food coloring (see Device Protocols included in Appendix B). In the future, we will continue optimizing our devices by iterating on their designs based on user feedback. Our ultimate goal is to make the platform commercially accessible, and thus add to the toolbox of cell culture technologies that are available to any biology researcher.

4.2.6 Materials and Methods

Device fabrication: We have previously described details of design and fabrication of 3D printed and milled devices, as well as cleaning procedures.[9] Briefly, devices were fabricated with a 3D printer (Form 2, Formlabs) or a CNC mill (PCNC 770, Tormach; Datron Neo, Datron) during the iterative design process. The final devices that are featured in this work were injection molded in polystyrene (Styron 666D) through Protolabs (Protolabs, Maple Plain, MN). The Monorail2 device mold was polished—using the highest level polish available (SPI_A2)— on the contact area; the Monorail 1 device mold was not polished.

Device preparation for diffusion experiments (**Figure 4.2.4**): Injection molded Monorail2 devices were sonicated in isopropanol for 1 h, soaked in 70% ethanol for 30 min, and allowed to air-dry overnight. Before use, devices were plasma treated for 5 min at 0.25 mbar and 70 W in a Zepto LC PC Plasma Treater (Diener Electronic GmbH, Ebhausen, Germany) using oxygen. The

devices were inserted into the bottom of a tissue culture treated polystyrene 12-well plate (Corning, 07-200-82) and loaded with 40 µL of either collagen or low gelling temperature agarose. Once gelled, 1X PBS was loaded into the center chamber (8 µL), side chambers (20 µL/chamber), and sacrificial media reservoir (500 µL) and stored at 6 °C overnight. 1X PBS in the center chamber was replaced with fluorescent dye the following morning (t = 0 hour), and the plate was incubated at 37 °C. Solution from the side chambers were collected and pooled at t = 6 h, 12 h, and 24 h for each technical replicate. The fluorescence of each sample was measured using a Multiskan Spectrum UV/Visible Microplate Reader (Thermo Labsystems, Waltham, MA) (n = 4 for each time point).

Hydrogel preparation: Collagen was prepared using a 1:9 solution of 10X HEPES (500 mM HEPES with 10X PBS and pH 7.6): ~9 mg/mL rat tail collagen I (Corning, 354249), producing a final concentration of 1X HEPES and ~8 mg/mL collagen. The collagen solution was pipetted into the devices at the loading port. After conclusion of flow in devices, plates were incubated at 37 °C for at least 30 min before 1X PBS loading. Agarose was prepared using low gelling temperature agarose (Sigma-Aldrich, 39346–81-1) and 1X PBS for a final concentration of 1.5 wt%. Gel solution was autoclaved for sterilization and to aid in dissolving agarose. Gel solution was heated to 55 °C before loading into device and allowed to cool at room temperature after conclusion of flow. Once gelled, devices were loaded with 1X PBS.

Fluorescent dye preparation: 10 µM fluorescent dye solutions for Alexa Fluor 488 (MW 546 Da, Thermo Fisher, A33077), dextran Alexa Fluor 527 (MW 10 kDa, Invitrogen, D22911) and dextran fluorescein (MW 70 kDa, Invitrogen, D1823) were all prepared in 1X PBS.

Device preparation for evaporation and biological experiments (**Figure 4.2.2, 4.2.3, 4.2.5,** and **B6**): Prior to use, all devices were rinsed with deionized water, sonicated for one hour in isopropanol and for 30 min in 70% ethanol, air dried and treated with oxygen plasma at 0.25 mbar and 70 W for 5 min in a Zepto LC PC Plasma Treater (Diener Electronic GmbH, Ebhausen, Germany). For the evaporation assays (**Figures 4.2.2** and **4.2.3**), devices were placed directly

into the wells of tissue culture treated 12-well plates (Corning 3513). For immunostaining experiments (**Figure B6**), glass coverslips were sterilized with 70% ethanol, inserted into wells, and submerged in a coating solution containing 0.01 wt% poly-L-lysine (Sigma, P4707) for 30 min. Coating solution was then aspirated, and coverslips were washed 3 times with sterile deionized water. Monorail1 devices (**Figure B6 c,d**) or milled Monorail2 devices (**Figure B6 b,e**) were then placed on top of glass coverslips inside of wells. Collagen I was used to make the hydrogel wall for experiments shown in **Figure 4.2.2** and **Figure B6 b,c,e**. For all other experiments, low gelling temperature agarose was used to make the hydrogel wall; we recommend using agarose for experiments involving primary cells isolated from tissues digested with collagenase (**Figure 4.2.5**), as residual collagenase can digest the hydrogel wall if collagen I is used. Detailed protocols for preparation/use of the devices presented in this manuscript can be found in Appendix B. These protocols include “test your hands” sections that we send out to biology labs who use these devices. We recommend that new users follow the “test your hands” protocol (which uses food coloring added to the cell culture chambers) to ensure that they can form the hydrogel walls correctly before running biological experiments.

Primary cell isolation and culture (**Figure 4.2.5**): Experiments were conducted under a protocol approved by the University of Washington Institutional Review Board (IRB), which ensures compliance with institutional guidelines and national laws concerning human subjects research. Subjects provided informed consent for use of residual tissue from testicular sperm extraction. Following isolation of sperm for cryopreservation, residual testis tissue was received and placed in DMEM/F12 media containing 10 mg/mL type IV collagenase and 25 mg/mL DNAse for 30 min at 37 °C.[31] Following enzymatic digestion, tubule tissue settled for 5 min with gravity and the supernatant was removed and centrifuged for 7 min at 250 RPM. The resulting pellet was resuspended in culture media (Adv DMEM/F12 media with 1% BSA, 10% fetal bovine serum and 1% Pen/strep) and underwent two washings and centrifugations prior to resuspension in 100 µL of culture media. Viability of mixed interstitial testis cells was assessed with a trypan blue assay

and was greater than 80% prior to seeding into the device. 8 µL of cell suspension was added to each center well of the Monorail2 device, with media placed in the outer wells and media reservoir. Primary testis cells were incubated at 34 °C for 4 and 7 days prior to fixation with paraformaldehyde for phase contrast imaging.

Prostate cancer cell-adipocyte coculture (**Figure 4.2.6**): In this study, the experiments were performed using human prostate cancer cells (PC-3) and an adipocyte phenotype cell line (3T3-L1). The cell lines were purchased from ATCC (Manassas, VA, USA). Cells were maintained in DMEM medium (Gibco, Ref #:11330–032) containing 10% FBS and 1% penicillin/streptomycin (Gibco, 15240) in flasks. PC-3 and 3T3-L1 cells were cocultured in separate wells of the Monorail1 device. We prepared a cell density of 1×10^6 cells/mL and 10 µL of the solution was placed in each well of the Monorail1 device along with 12 µL of medium. The cell containing device was then incubated at 37 °C under 5% CO2 in RPMI medium (ThermoFisher Scientific, Waltham, MA, USA) containing 10% fetal bovine serum (FBS; Sigma, St Louis, MO,USA) and penicillin (100 units/ml)/streptomycin (100 µg/ml). After 24 h, cells were fixed in 10% formalin prior to staining.

4.2.7 References

1. E. K. Sackmann, A. L. Fulton and D. J. Beebe, The present and future role of microfluidics in biomedical research, *Nature*, 2014, **507**, 181–189.
2. B. Zhang, A. Korolj, B. F. L. Lai and M. Radisic, Advances in organ-on-a-chip engineering, *Nat. Rev. Mater. 2018 38*, 2018, **3**, 257–278.
3. D. Huh, Y. S. Torisawa, G. A. Hamilton, H. J. Kim and D. E. Ingber, Microengineered physiological biomimicry: organs-on-chips, *Lab Chip*, 2012, **12**, 2156–2164.
4. E. Berthier, A. M. Dostie, U. N. Lee, J. Berthier and A. B. Theberge, Open Microfluidic Capillary Systems, *Anal. Chem.*, 2019, **91**, 8739–8750.
5. S. H. Lee, A. J. Helnz, S. Shln, Y. G. Jung, S. E. Chol, W. Park, J. H. Roe and S. Kwon, Capillary based patterning of cellular communities in laterally open channels, *Anal. Chem.*, 2010, **82**, 2900–2906.
6. B. P. Casavant, E. Berthier, A. B. Theberge, J. Berthier, S. I. Montanez-Sauri, L. L. Bischel, K. Brakke, C. J. Hedman, W. Bushman, N. P. Keller and D. J. Beebe, Suspended microfluidics, *Proc. Natl. Acad. Sci. U. S. A.*, 2013, **110**, 10111–10116.
7. J. Berthier, K. A. Brakke and E. Berthier, Open microfluidics, 2016, 330.
8. E. J. Walsh, A. Feuerborn, J. H. R. Wheeler, A. N. Tan, W. M. Durham, K. R. Foster and P. R. Cook, Microfluidics with fluid walls, *Nat. Commun.*, , DOI:10.1038/S41467-017-00846-4.
9. S. B. Berry, T. Zhang, J. H. Day, X. Su, I. Z. Wilson, E. Berthier and A. B. Theberge, Upgrading well plates using open microfluidic patterning, *Lab Chip*, 2017, **17**, 4253–4264.

10. Y. Lee, J. W. Choi, J. Yu, D. Park, J. Ha, K. Son, S. Lee, M. Chung, H. Y. Kim and N. L. Jeon, Microfluidics within a well: an injection-molded plastic array 3D culture platform, *Lab Chip*, 2018, **18**, 2433–2440.
11. J. Ko, J. Ahn, S. Kim, Y. Lee, J. Lee, D. Park and N. L. Jeon, Tumor spheroid-on-a-chip: a standardized microfluidic culture platform for investigating tumor angiogenesis, *Lab Chip*, 2019, **19**, 2822–2833.
12. X. Su, A. B. Theberge, C. T. January and D. J. Beebe, Effect of microculture on cell metabolism and biochemistry: do cells get stressed in microchannels?, *Anal. Chem.*, 2013, **85**, 1562–1570.
13. S. H. Yun, L. M. Cabrera, J. W. Song, N. Futai, Y. C. Tung, G. D. Smith and S. Takayama, Characterization and resolution of evaporation-mediated osmolality shifts that constrain microfluidic cell culture in poly(dimethylsiloxane) devices, *Anal. Chem.*, 2007, **79**, 1126–1134.
14. E. Berthier, J. Warrick, H. Yu and D. J. Beebe, Managing evaporation for more robust microscale assays. Part 1. Volume loss in high throughput assays, *Lab Chip*, 2008, **8**, 852–859.
15. E. Berthier, J. Warrick, H. Yu and D. J. Beebe, Managing evaporation for more robust microscale assays, *Lab Chip*, 2008, **8**, 860–864.
16. D. J. Guckenberger, T. E. De Groot, A. M. D. Wan, D. J. Beebe and E. W. K. Young, Micromilling: a method for ultra-rapid prototyping of plastic microfluidic devices, *Lab Chip*, 2015, **15**, 2364–2378.
17. D. B. Wolfe, D. Qin and G. M. Whitesides, Rapid prototyping of microstructures by soft lithography for biotechnology, *Methods Mol. Biol.*, 2010, **583**, 81–107.
18. E. W. K. Young, E. Berthier, D. J. Guckenberger, E. Sackmann, C. Lamers, I. Meyvantsson, A. Huttenlocher and D. J. Beebe, Rapid prototyping of arrayed microfluidic systems in polystyrene for cell-based assays, *Anal. Chem.*, 2011, **83**, 1408–1417.
19. P. F. O'Neill, A. Ben Azouz, M. Vázquez, J. Liu, S. Marczak, Z. Slouka, H. C. Chang, D. Diamond and D. Brabazon, Advances in three-dimensional rapid prototyping of microfluidic devices for biological applications, *Biomicrofluidics*, , DOI:10.1063/1.4898632.
20. S. Tanzi, P. F. Ostergaard, M. Matteucci, T. L. Christiansen, J. Cech, R. Marie and R. Taboryski, Fabrication of combined-scale nano- and microfluidic polymer systems using a multilevel dry etching, electroplating and molding process, *J. Micromechanics Microengineering*, 2012, **22**, 115008.
21. S. Tanzi, M. Matteucci, T. L. Christiansen, S. Friis, M. T. Christensen, J. Garnaes, S. Wilson, J. Kutchinsky and R. Taboryski, Ion channel recordings on an injection-molded polymer chip, *Lab Chip*, 2013, **13**, 4784–4793.
22. U. N. Lee, X. Su, D. J. Guckenberger, A. M. Dostie, T. Zhang, E. Berthier and A. B. Theberge, Fundamentals of rapid injection molding for microfluidic cell-based assays, *Lab Chip*, 2018, **18**, 496–504.
23. J. Lee, Y. H. Foong, I. Musaitif, T. Tong and C. Jefcoate, Analysis of specific RNA in cultured cells through quantitative integration of q-PCR and N-SIM single cell FISH images: Application to hormonal stimulation of StAR transcription, *Mol. Cell. Endocrinol.*, 2016, **429**, 93–105.
24. E. Berthier, E. W. K. Young and D. Beebe, Engineers are from PDMS-land, Biologists are from Polystyrenia, *Lab Chip*, 2012, **12**, 1224–1237.
25. S. Halldorsson, E. Lucumi, R. Gómez-Sjöberg and R. M. T. Fleming, Advantages and challenges of microfluidic cell culture in polydimethylsiloxane devices, *Biosens. Bioelectron.*, 2015, **63**, 218–231.
26. C. M. Carney, J. L. Muszynski, L. N. Strotman, S. R. Lewis, R. L. O'Connell, D. J. Beebe, A. B. Theberge and J. S. Jorgensen, Cellular microenvironment dictates androgen production by murine fetal Leydig cells in primary culture, *Biol. Reprod.*, ,

DOI:10.1095/BIOLREPROD.114.118570.
27. G. De Pergola and F. Silvestris, Obesity as a major risk factor for cancer, *J. Obes.*, , DOI:10.1155/2013/291546.
28. K. M. Nieman, I. L. Romero, B. Van Houten and E. Lengyel, Adipose tissue and adipocytes support tumorigenesis and metastasis, *Biochim. Biophys. Acta*, 2013, **1831**, 1533–1541.
29. F. Nardi, O. E. Franco, P. Fitchev, A. Morales, R. E. Vickman, S. W. Hayward and S. E. Crawford, DGAT1 Inhibitor Suppresses Prostate Tumor Growth and Migration by Regulating Intracellular Lipids and Non-Centrosomal MTOC Protein GM130, *Sci. Rep.*, , DOI:10.1038/S41598-019-39537-Z.
30. B. Dirat, L. Bochet, G. Escourrou, P. Valet and C. Muller, Unraveling the obesity and breast cancer links: a role for cancer-associated adipocytes?, *Endocr. Dev.*, 2010, **19**, 45–52.
31. H. Chemes, S. Cigorraga, C. Bergada, H. Schteingart, R. Rey and E. Pellizari, Isolation of human Leydig cell mesenchymal precursors from patients with the androgen insensitivity syndrome: testosterone production and response to human chorionic gonadotropin stimulation in culture, *Biol. Reprod.*, 1992, **46**, 793–801.

Chapter 5 | Miniaturizing wet scrubbers for aerosolized droplet capture

Reproduced in part from U.N. Lee, T.L. van Neel,* F.Y. Lim, JW. Khor, J. He, R.S. Vaddi, A.Q.W. Ong, A. Tang, J. Berthier, J.S. Meschke, I.V. Novosselov,§ A.B. Theberge,§ E. Berthier,§ "Miniaturizing wet scrubbers for aerosolized droplet capture." Analytical Chemistry, **2021**, 93, 11433–11441.*
** Equal contribution*
§ Co-corresponding authors

UNL and TLvN designed the device and conducted experiments; FYL advised on microbes; JK and RSV advised on simulations; JH, AQWO, and AT conducted trainings for capture efficiency experiments and assays; JSM provided expertise in bioaerosols; IVN, ABT, and EB supervised and UNL, TLvN, ABT and EB interpreted the results.

Abstract: Aerosols dispersed and transmitted through the air (e.g., particulate matter pollution, bioaerosols) are ubiquitous and one of the leading causes of adverse health effects and disease transmission. A variety of sampling methods (e.g., filters, cyclones, impactors) have been developed to assess personal exposures. However, a gap still remains in the accessibility and ease-of-use of these technologies for people without experience or training in collecting airborne samples. Additionally, wet scrubbers (large non-portable industrial systems) utilize liquid sprays to remove aerosols from the air; the goal is to "scrub" (i.e., clean) the exhaust of industrial smokestacks, not collect the aerosols for analysis. Inspired by wet scrubbers, we developed a device fundamentally different from existing portable air samplers by using aerosolized microdroplets to capture aerosols in personal spaces (e.g., homes, offices, schools). Our aerosol-sampling device is the size of a small teapot, can be operated without specialized training, and features a winding flow path in a supersaturated relative humidity environment enabling droplet growth. The integrated open mesofluidic channels shuttle coalesced droplets to a collection chamber for subsequent sample analysis. Here, we present the experimental demonstration of aerosol capture into water droplets. Iterative study optimized the non-linear flow manipulating baffles and enabled an 83% retention of the aerosolized microdroplets in the confined volume of our device. As a proof-of-concept for aerosol capture into a liquid medium, 0.5-3 μm model

particles were used to evaluate aerosol capture efficiency. Finally, we demonstrate the device can capture and keep a bioaerosol (bacteriophage MS2) viable for downstream analysis.

5.1 Introduction

We inhale a variety of aerosols (e.g., dust particles, ultrafine particulate matter [PM], biologically derived aerosols, and potentially infectious bioaerosols) on a daily basis.[1–3] When aerosols come into contact with the incredibly large surface area of the lungs, they can trigger and exacerbate allergic reactions, cause serious infections, and induce severe toxic reactions, particularly in immunocompromised individuals.[3–5] Despite years of research on the effects of aerosols on human health, our understanding of the effects specific types of aerosols can have on our short- and long-term health has focused largely on a number of salient aerosol types (e.g., cigarette smoke and $PM_{2.5}$ particles)[6,7] and environmental settings (hospitals, farms, etc.).[8–11] This is in part due to the fluctuating and highly personalized nature of an individual's exposure as the formation, dispersion, and transport of aerosols is influenced by both physical (e.g., size, shape, and density of aerosols) and environmental (e.g., air currents, humidity, and temperature) factors.[12,13] Coupled with the limitations of personal sampling and ability to analyze chemical and biological composition of the collected sample, researchers and clinicians are still unable to pinpoint the patient-specific triggers for the millions of people worldwide affected by environmentally induced respiratory illnesses. There is a need for a portable and easy-to-operate air-sampling device to inform individuals of their environmental exposures and provide information on personalized health triggers (**Figure 5.1**). In this work, we developed a lightweight and low-cost portable device that can be used without technical training; it utilizes liquid to capture aerosols for subsequent analysis—effectively miniaturizing technology used in industrial wet scrubbers. We aimed to maximize the time in which aerosolized microdroplets interact with aerosols to improve capture.

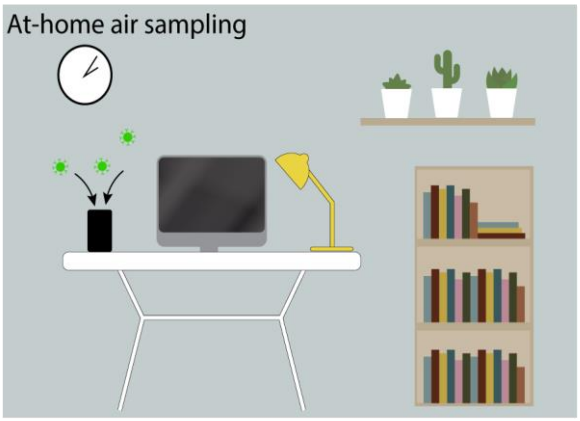

Figure 5.1. Schematic representation of our battery-powered air sampling device (small black box to the left of the computer), collecting aerosols in a home environment to provide information on the landscape of aerosols in the room. The concept is that our device can be placed in any environment (e.g., homes, schools, hospitals, playgrounds, and farms) and then sent back to a laboratory for analysis.

To date, a variety of passive[14] and active[15,16] sampling devices have been developed for the collection of bioaerosols, including filter collection, centrifugal collection, electrostatic precipitation, liquid impingement, impaction, and direct collection on growth media.[17–21] Information on aerosol concentration and size distribution can also be obtained in real time using aerosol particle counters;[22–24] however, these monitors neither collect particles nor retain viable samples for further specific identification and analysis.[25] With respect to direct personal exposure monitoring, some of the aerosol collection methods may not be practical; for example, filter collection and analysis is limited by high elution volumes, bulky setup, and high-power requirements. Due to the development in miniaturization of sampling pumps and electronics, exposure measurement methods including biological aerosol collectors[26–30] have rapidly advanced and gained popularity.[16,22,31–33] For non-spore-forming infectious bioaerosols (e.g., viruses and vegetative bacterial cells), desiccation during sampling is problematic for downstream viability analyses and infectivity studies.[34] Although bulk liquid and hydrated gel components integrated in established sampling devices have shown to improve viability and culturability,[35] their large collection volume and substantial power requirements limit their applicability in

personal samplers and analysis techniques where small collection volume and direct integration with microfluidic devices are desired.

An alternative to collection in bulk liquids is liquid droplet sprays similar to the ones used in wet scrubbers.[36] These systems have been most effective for removing aerosols larger than 1.0 μm from the air, but they are large (ranging from the size of a small appliance to an industrial smokestack) and have high energy consumption.[37] The physical phenomena governing the capture of aerosol by droplets in gas flows have been simulated for wet scrubbers[38–40] and have shown that it is possible to increase the capture efficiency of aerosols (including those smaller than 1.0 μm) by decreasing the droplet size and increasing droplet residence time in the scrubber.[40] The overall collection efficiency can be approximated by summing the modes of capture--diffusion, interception, inertial impaction, and gravitational settling[39]—although most of these require large timescales to operate effectively, which is difficult to achieve in a small-scale device. The relationship between the aerosol size and predominant mode of capture has previously been evaluated; impaction was found to be a predominant mode for the capture of aerosol sizes $d_p > 5.0$ μm, and diffusion was a predominant mode for the capture of aerosol sizes $d_p < 1.0$ μm.[38] At $d_p < 0.05$ μm, impaction and interception are negligible and diffusion can be considered as the sole mode of capture. Interception is unaffected by the flow rate, but changes with droplet size and packing.[41] Industrial wet scrubbers generate the required liquid droplets using large spray towers. Alternatively, an attractive method for generating liquid microdroplets is ultrasonic atomizers due to their compact size and use in existing consumer products such as home humidifiers. Recent studies using ultrasonic atomizers to generate sprays of liquid microdroplets showed a decrease in $PM_{2.5}$ and PM_{10} concentration over time when the microdroplets were injected near burning incense.[42]

In this work, we harnessed the benefits of microdroplet liquid sprays to fill the need for an accessible and portable at home air-sampling device that collects aerosols in a liquid compatible with downstream analysis methods. To our knowledge, our device is the first battery-powered air-

sampling device that uses aerosolized microdroplets to capture aerosols for analysis. We demonstrate the function and performance of the device using model fluorescent aerosol. Our results suggest how the approach can be used for bioaerosol collection. The portable air-sampling device generates a mist of 4.0 μm liquid droplets and mixes it with aerosols. The device guides the mixture in a non-linear path to keep microdroplets suspended in the open spaces of the device for as long as possible. The droplet residence time (time the droplet spends suspended in a gas flow) along with droplet packing (number of droplets present) has been shown to increase capture efficiency.[40] We demonstrate that aerodynamic features enable the capture of the generated mist in a reduced volume and present optimization criteria for device geometry. By leveraging the principles of open microfluidics, we created a pathway via horizontal and vertical open mesofluidic channels for the coalesced droplets to travel and collect for future downstream analysis.[43,44] We evaluate the effect of flow patterns on droplet retention efficiency and the model aerosol capture efficiency for a 0.5−3.0 μm size range. Finally, we demonstrate that the device can capture and keep a bioaerosol viable for downstream analysis.

5.2 Design considerations

We developed a portable air-sampling device, approximately the size of a small teapot, which can be placed in many environments (e.g., homes, schools, hospitals, playgrounds, and farms) for aerosol capture. Major considerations for the device included how to keep the device within a comfortable size to place on a desk, battery-powered to avoid the need of a power outlet, and simple to operate in a variety of environments. An additional consideration included maintaining the captured bioaerosols in liquid to ensure their viability and compatibility with rapid downstream analysis, a point of interest for future studies. Although we focused the demonstration herein on manipulating airflow for microdroplet retention, we also used model inert particles to demonstrate the capability of the air-sampling device with bioaerosol applications in mind. An air-sampling device based on aerosolized microdroplets has the potential to capture a wide range of aerosols[37]

and is amenable for use with a variety of liquid capture solutions (i.e., water, surfactant, media, and solvents). Given the efficacy of wet scrubbers, we chose to incorporate liquid droplets in our portable sampling device. Our air-sampling device consists of a small fan, an ultrasonic atomizer (droplet generator), and a 3D printed body (**Figure 5.2 a**). The fan draws in air from the environment, and an ultrasonic atomizer generates 4.0 μm liquid droplets which move in the same direction as the air flow; the goal for the liquid droplets is to capture aerosols that enter through the fan. In our device, the microdroplets have an initial velocity that is independent of the air flow generated using the fan. Although the fan flow rate is tunable by adjusting the voltage delivered to the fan, the aerosol experiments and simulations given in this article were conducted with a flow rate of 6.3 slpm. Additionally, the initial velocity of the microdroplets is constant due to the designed frequency of the ultrasonic atomizer. The microdroplets and aerosols are carried in a nonlinear path by the airflow generated using the fan and coalesce on fluidic baffles, which will be discussed further in **Figures 5.3** and **5.4**. The baffles contain open mesofluidic channels that guide the coalesced droplets to a collection reservoir at the bottom of the device (**Figure 5.2 b**). The clean liquid reservoir and sample collection reservoir were designed to hold up to 200 mL of

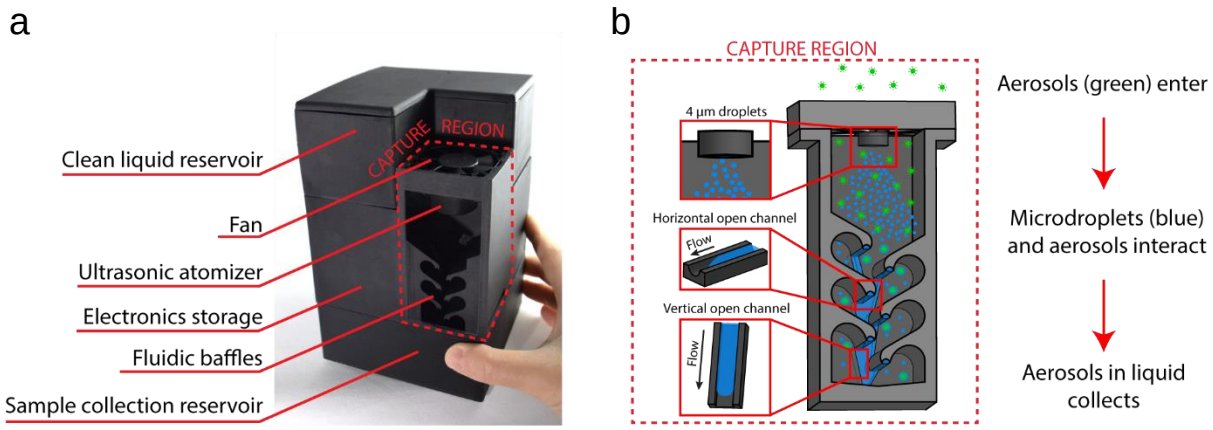

Figure 5.2. Portable droplet-based air-sampling device. (a) Photograph of the device. (b) Schematic of capture region workflow. An ultrasonic atomizer generates 4 μm droplets (top), and horizontal (middle) and vertical (bottom) open mesofluidic channels collect coalesced droplets and aerosols. Aerosols enter through the fan, microdroplets intercept the aerosols, and six-angled baffles guide the airflow to increase capture of aerosols. The front wall of the device has been removed for visualization of the device.

fluid each for an operation time of 1 h but the device is amenable to other volumes and operation times (**Figure 5.2 a**). Electronic components (fan and ultrasonic atomizer) were made compatible for battery operation to improve overall portability, but the battery also limits the operation time (**Figure C1**). Due to the low pressure drop of the flow path, the device can be operated using low-cost fans, that is, does not require pumps, typical for most of the widely used air-sampling devices today (e.g., Anderson cascade impactors, Burkard personal volumetric air sampler, Coriolis biological air sample, cyclones, and impingers).

5.3 Flow guiding baffles and open fluidic channels

The capture region of the air-sampling device was designed to increase interactions and mixing of microdroplets and aerosols. In traditional wet scrubbers, the droplet paths are linear; therefore, to increase microdroplet residence times, it is necessary to increase the height of the device. In order to minimize the device size and maintain portability, we designed fluidic baffles that generate recirculation zones with a longer residence time than the main airflow (**Figure 5.3 ai**). Air and droplets follow the flow paths and populate regions under each baffle due to a low Stokes number (< 0.03). Internal geometry of the flow channel consists of a series of horizontal open channels underneath the baffles, connected with a vertical open channel along the back wall (**Figure 5.2 b**). The constriction bends to form an impinging jet on the upper surface of each baffle (**Figure 5.3**). The behavior of impinging jets has been described in the literature,[45–47] and their comprehensive analysis is beyond the scope of this paper. However, for the purpose of this work, it is important to understand that the angled impinging jets create stagnation regions (**Figure 5.3 ai,** left).

In our device, the stagnation regions occur at the edge of the baffles; a portion of the jet follows the curve of the baffle (creating recirculation zones), and the remaining jet joins the bulk flow in the constriction (**Figure 5.3 ai,** right). Microdroplet growth and transition to liquid effluent is likely due to two complementary mechanisms: (i) microdroplet coalescence and (ii)

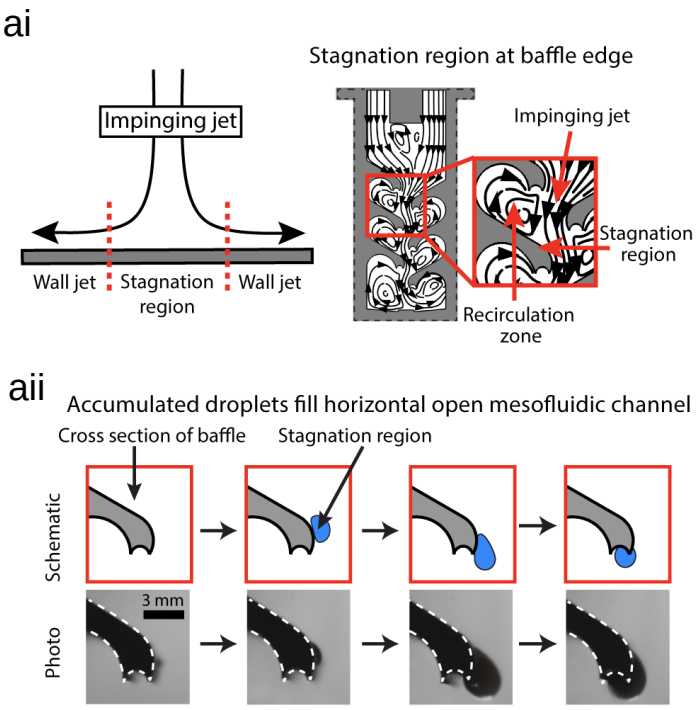

Figure 5.3. Impinging jet, stagnation region, and horizontal mesofluidic channels. (ai) Basic schematic representation of an impinging jet (left) and the stagnation region in the device (right). (aii) Droplets accumulate in a stagnation region on the baffle and migrate down the edge of the baffle, where it travels in the horizontal and vertical channels. Images were taken with a device that did not have a back wall, and water was colored dark blue to enable better visualization of the droplet. Video of droplet formation in the stagnation region is available in online (Video S1).

heterogeneous growth in a supersaturated environment. These are similar to the growth of combustion-generated particles, where recirculation leads to the formation of large super-aggregates.[48,49] While it is challenging to model these processes, the highest probability of droplet coalescence and heterogeneous growth occurs in regions with long residence time and high droplet concentration. In our geometry, these conditions are present in the stagnation regions and in the recirculation zone. Once larger droplets are formed, they either settle on the surface due to gravity or via inertial impaction associated with the impinging jet. On the surface, these larger droplets migrate to the edge under the aerodynamic load acting on the droplet[50–53] or by gravity and are collected in the horizontal open mesofluidic channel embedded in the edge of the baffle (**Figure 5.3 aii**). The horizontal open channel guides the aerosol-laden sample toward the back wall where it meets the vertical open channel; this vertical open channel connects all the baffles and drains the sample into a collection reservoir (**Figure 5.4**).

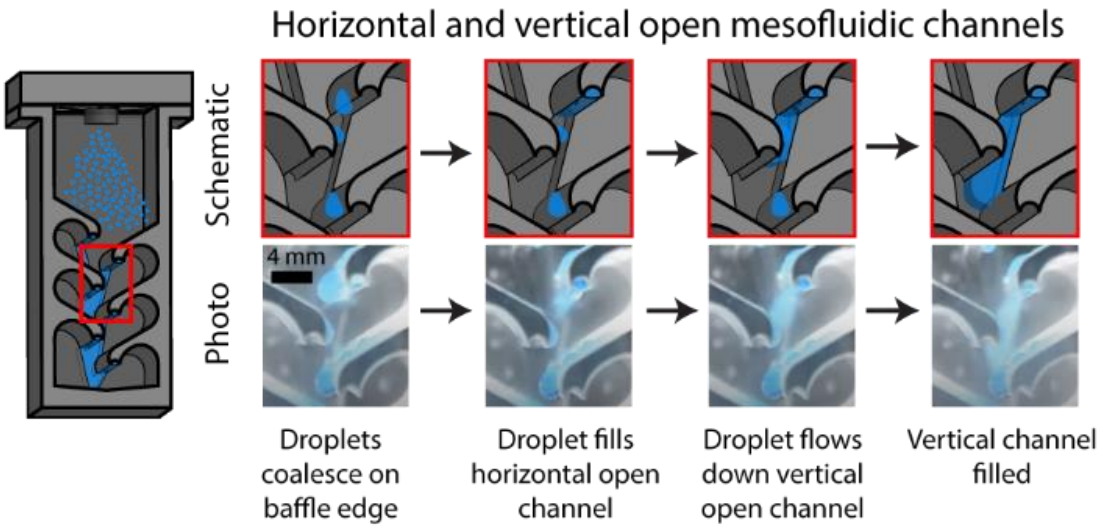

Figure 5.4. Schematic (top) and photograph (bottom) of progression of filling the mesofluidic channel at the edge of a baffle. Video was taken using a clear device to enable better visualization of the channel.

5.4 Computational modeling of airflow and effects of baffle geometry

Computational modeling aimed to (1) better visualize formation of recirculation zones and air flow around the baffles and (2) improve droplet retention within the device (reducing droplet loss through the outlet). The microdroplet−aerosol collisions were increased by incorporating baffles, thus promoting the formation of recirculation zones. The multiple impinging jet flow pattern enables inertial impaction of droplets on surfaces for capture. Using CFD (COMSOL Multiphysics), we performed a parameter space optimization of the features in the capture region, specifically looking at how they affected airflow (**Figure 5.5**), and ultimately improved droplet retention (**Figure 5.6**). We solved for a mean air velocity field and pressure in a steady state. We modeled a 2D cross-section to reduce computational load.[54] Recognizing the challenges associated with modeling and validation of aerosol-laden flow,[55] here, CFD was used as a comparative tool to inform device design iterations and not as an absolute or quantitative method. The full details of the model are presented in the experimental section. Briefly, the following boundary conditions were used: a fully developed flow rate profile was used for the inlet with a zero-pressure outlet; all other walls were modeled with a no-slip boundary condition.

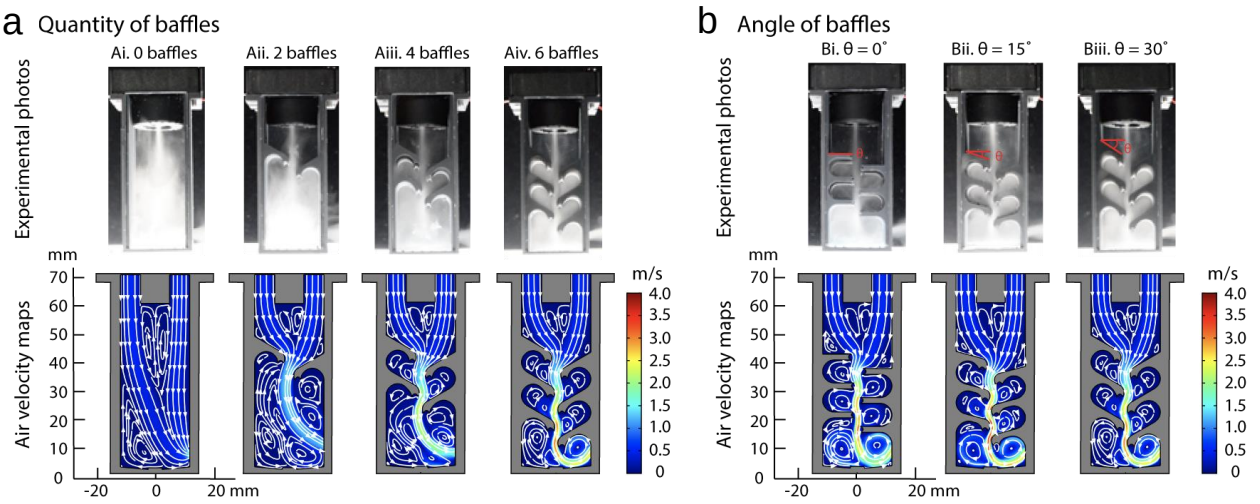

Figure 5.5. Effect of baffle quantity and angle on airflow. Experimental photographs showing droplets in the device and mean airflow velocity maps of a 2D cross-section of the device with (a) 0, 2, 4, and 6 baffles (all at a 30° angle) and (b) 0°, 15°, and 30° baffle angles. Images were taken at different time points and should not be compared with one another. Colors represent velocity and indicate the fluid flow (airflow) modeled. White lines and arrows represent direction of flow. Devices used in photographs do not have front or back walls to enable visualization of the droplets.

Experimentally, we observed droplets accumulating on all surfaces in the device, coalescing to form larger droplets, and being shuttled away by the mesofluidic channels to the collection area (supporting Videos S1 and S2 can be found online). Modeling the mean airflow in the device enabled us to extract details such as the direction and pattern of the airflow; the flow within the device is laminar with a calculated Reynolds number < 1200. To understand the effect of baffle geometry on recirculation zone formation and air flow, we varied the quantity and angle of the baffles (**Figure 5.5**). More recirculation zones were created with each additional set of baffles (**Figure 5.5 a**). The baffles also increased the probability of droplet capture due to (i) an increased surface to volume ratio and (ii) the greater number of impinging jet regions where the high velocity interacts with the wall. This is supported by experimental droplet retention results shown in **Figure 5.6**. Furthermore, each extra set of baffles constricts the main airflow, resulting in an increased velocity of the impinging jet and allowing for more effective liquid transport from the stagnation regions to the mesofluidic channel (**Figure 5.3**). The horizontal space between the baffles controls the airflow constriction, but if too small, it can also cause backflow in the device.

The number of stagnation regions increases with the quantity of baffles, providing more areas of high coalescence for droplets (**Figure 5.3 a**). Finally, the pressure above the top baffles increases with each additional set of baffles and decreases as the angle increases (**Figure C2**). Based on these observations, the six-baffle design was used in aerosol capture efficiency studies to be discussed in **Figure 5.7**.

5.5 Microdroplet retention efficiency

The microdroplets generated to capture aerosols in air must subsequently be captured by the device to perform analyses. The microdroplet capture process is challenging due to the high rate of air flow through the device and the need to not constrict that air flow. As the ultrasonic atomizer generates microdroplets and the fan draws aerosols into the device, an airflow exhaust must be designed to prevent flow exiting through the inlet in the case of high back pressure. An unobstructed geometry will lead to microdroplets flowing through the device without being captured. We sought to maximize the microdroplet retention while keeping an outlet to prevent backflow. The pressure drop associated with the impinging jet in stagnation regions helps coalesce the droplets on the baffles; however, it should not be high enough to cause backflow. We chose not to employ a mesh filter to increase microdroplet retention because recovering bio-aerosols from filters can be damaging.[56] Additionally, droplets clog the small apertures on mesh surfaces which blocks airflow.

Through various design iterations, we measured the percentage of liquid retained by weighing the ultrasonic atomizer filled with water and the aerosol capture region of the device before and after operating the ultrasonic atomizer. Microdroplet retention increased with the number of baffles with an 81% droplet retention in the six-baffle design (**Figure 5.6 a**). We also studied the effect of the angle of the baffle on microdroplet retention. There was an increase in microdroplet retention between the 0° and 15° baffle angle followed by a decrease between the 15° and 30° baffle angle. A 15° baffle angle had the largest microdroplet retention of 83%, while

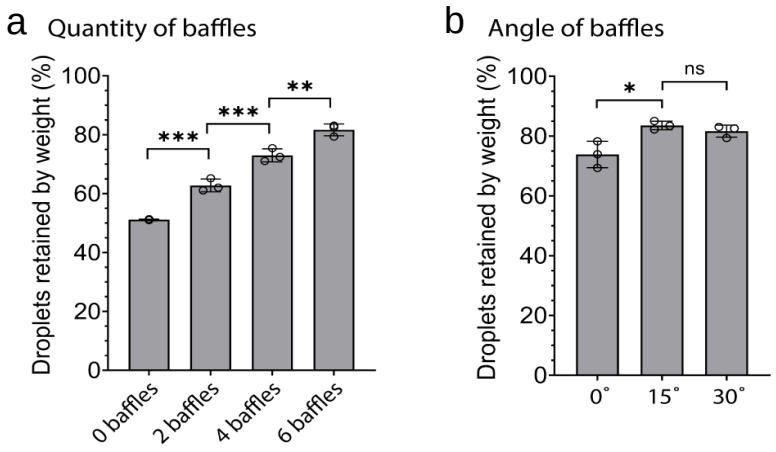

Figure 5.6. Effects of baffle quantity and angle on microdroplet retention. Microdroplet retention trends were determined by weighing the liquid retained in the device before and after running the ultrasonic atomizer. (a) Six-baffle design has the highest microdroplet retention (81.6 ± 1.6%) and was used for further device iteration studies. (b) 15° baffle angle design retained a higher percentage of microdroplets (83.5 ± 1.1%) than a 0° baffle angle (73.8 ± 3.6%). No significant difference (ns) was observed with an additional 15° baffle angle (30°; 81.6 ± 1.6%). The bar graph represents the mean ± SD of n = 3 experimental tests. One-way ANOVA with post hoc Tukey's multiple comparison test; *$p < 0.05$, **$p < 0.005$, and ***$p < 0.001$. Devices tested in (A) all had a 30° baffle angle.

the 0° and 30° baffle angle had a 73% and 81% microdroplet retention, respectively (**Figure 5.6 b**). Because there was not a statistically significant difference in microdroplet retention between the 15° and 30° baffle angle, we chose to move forward with the 30° baffle angle due to the reduced pressure near the fan inlet, which is favorable in reducing backflow as discussed previously (**Figure C2**).

5.6 Capture of model aerosols and a bioaerosol

An aerosol chamber[57] described previously was used to test the six-baffle, 30° baffle angle portable device for aerosol capture efficiency. Briefly, monodispersed fluorescent PSL spheres of varying sizes (0.5, 0.75, 1.0, 2.0, and 3.0 μm) were aerosolized in separate experiments using a nebulizer (**Table C1**). Two fans placed in opposite corners of the chamber were used to provide well-mixed conditions in the chamber. Three devices, co-located with reference filters, were tested in the chamber at the same time for 25 min. The reference filter flow rate matched the measured flow rate of our device (**Figure C3**). 25 mL of DI water was used to elute the particles from the

filter, and additional DI water was added to the device sample until the volume was also 25 mL. We measured the fluorescence of the liquid sample and used a ratio to determine aerosol collection efficiency. Particle sizes were selected based on model particles commonly used in bioaerosol research. The use of model PSL spheres for device testing was to avoid unnecessary exposure to bioaerosols (**Table C2**). It is important to note that we did not expect to reach 100% capture efficiency, nor was this required for analysis; furthermore, for bioaerosol detection, amplification steps [such as culture and polymerase chain reaction (PCR)] can be employed. The highest efficiency observed in our device was 17.5% with 0.5 µm particles and the lowest efficiency was 4.5% with 2.0 µm particles (**Figure 5.7**). Differences in aerosol capture efficiency were observed between the three devices tested likely due to heterogeneity in the microdroplets produced using the ultrasonic mist generators (**Figure C4**) and inherent differences in the 3D printing of the devices. The reproducibility across devices could be improved with more accurate fabrication methods. Importantly, we note that variability in capture efficiency was also observed in reference filters used likely due to the manual control of the flow rate and particle nebulization (**Table C3**). Based on the prior literature for other capture devices,[58–61] aerosol capture efficiency often varies with each particle size tested.

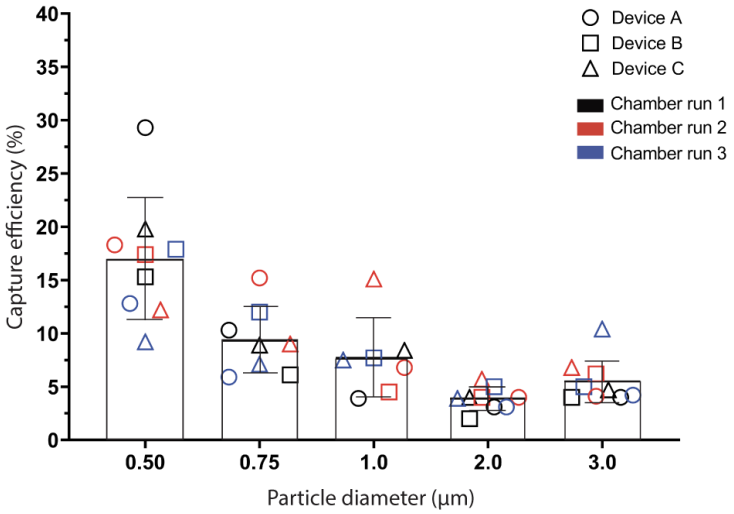

Figure 5.7. Capture efficiency of our portable air-sampling device (n = 3 devices) for 0.5, 0.75, 1.0, 2.0, and 3.0 µm polystyrene particles. The highest aerosol capture efficiency observed was 17.5% with 0.5 µm particles, and the lowest capture efficiency observed was 4.5% with 2.0 µm particles. Bar graphs represent mean ± SD of n = 3 independent chamber runs for each device. Symbol shape indicates different device A, B, or C; symbol color indicates independent chamber runs.

To demonstrate a potential application of our device in capturing bioaerosols while maintaining viability, we aerosolized a bacteriophage MS2 solution in a chamber with our device and analyzed the collected liquid from the device. MS2 is a virus that infects *E. coli* and is commonly used as a surrogate viral particle in aerosol studies for safety concerns.[62] Briefly, a solution of MS2 was nebulized in a closed aerosol chamber containing the device for a 25 min sampling period. As a control, we also performed a chamber run where no MS2 was nebulized. We then performed a plaque assay with the liquid samples collected from our device to determine if MS2 was present and viable. Plaque assays are used to quantify infectious viral particles.[63] The results from the control showed no MS2 (**Figure 5.8,** left). In comparison, samples from the chamber runs where MS2 was nebulized show that MS2 was captured using the device and able to infect *E. coli*; an indication that the MS2 remained viable (**Figure 5.8,** right).

To our knowledge, our device is the first battery-powered air-sampling device that uses microdroplets to capture aerosols for analysis. The high-humidity environment generated within the device coupled with storage of the captured aerosols in a fluid through the duration of the

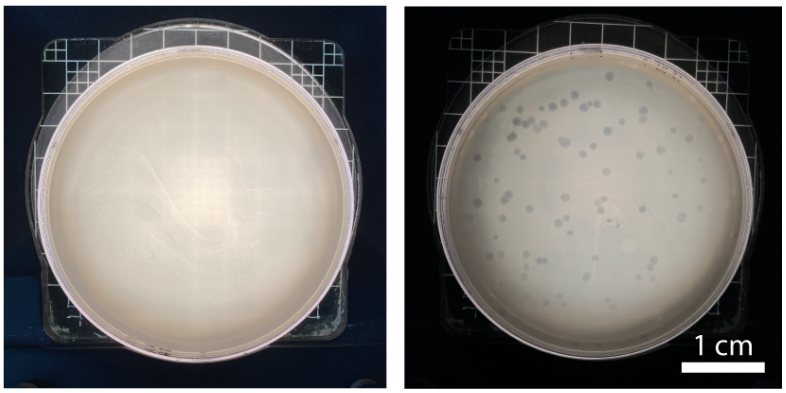

Figure 5.8. Bacteriophage MS2 captured in our air-sampling device remains viable. A plaque assay was performed using the liquid samples obtained from our device. A control liquid sample obtained from our device (no MS2 aerosolized in the chamber) showed no plaques (left) when cultured with *E. coli*, demonstrating MS2 absence from the sample. In contrast, when MS2 was aerosolized in the chamber, plaques formed (dark gray circles; right) as a result of MS2 infecting *E. coli*, indicating MS2 presence in the sample. Representative images of n = 2 independent chamber runs with one device.

sampling period has the potential to keep bioaerosols viable for downstream culture and analysis; in this case, high capture efficiency is not critical to the identification of the captured bio-aerosol because the sample can be amplified via culture (or detection methods like PCR). Additionally, the results were obtained with off-the-shelf low-cost components that can be further optimized to achieve higher efficiencies; however the device in its current state can be used in real-world environments. The bulk fluid also enables seamless integration with existing downstream analysis methods. To collect a sample from their environment, the only steps required by the user are: fill the reservoir with an appropriate fluid, flip the power switch, and put a cap on the collection reservoir after sampling. They would then mail the sample to a laboratory for analysis. Future work includes developing the sample preservation and analysis pipeline for bio-aerosols of interest. We note that there are numerous considerations and validation steps required in future work including selection of media; considerations will vary based on the analysis goal [e.g., simple detection of the presence of a microbe (yes/no) vs quantification]. The platform introduced in this article opens many avenues for future investigation.

5.7 Conclusion

In this work, we presented a portable air-sampling device that utilizes aerosolized microdroplets for aerosol capture. Future studies will focus on capture of bioaerosols for downstream analysis, viability studies, and infectivity assays. Our device is also well-positioned to be compatible with other low-viscosity fluids due to the working principles of the ultrasonic atomizer. Maximizing the capture of the liquid droplets after aerosolization using the ultrasonic atomizer will be part of future investigations to ensure the safety of expanding the use of potentially harmful fluids, such as organic solvents, as the capturing fluid. Ultimately our vision is that our air sampling platform will enable people who typically do not have access to or cannot afford services or products that measure environmental exposures (e.g., those in lower socio-economic groups or high-risk

environments) to collect air samples and determine the levels of environmental exposure in their daily lives.

5.8 Materials and Methods

Device Fabrication: The body of the device and ultrasonic atomizer cup were designed in Solidworks 2017 and 3D printed out of black resin (RS-F2-GPBK-04) using a Form 2 or Form 3 stereolithography 3D printer (Formlabs). The parts were cleaned with isopropyl alcohol (IPA) for 10 min in a FormWash (Formlabs) and rinsed with clean IPA to remove excess uncured resin. The devices were dried with compressed air and cured under a 395−405 nm 20 W UV lamp (Quans) for 1 h. A 1.3 mm PS thick window was milled (Datron neo) to enable visual access to the capture region of the device.

Portable Electronics (**Figures 5.2A, 5.7,** and **5.8**): An ultrasonic atomizer (Comidox) with a frequency of 113 kHz and 730 apertures each 5 μm in diameter was adhered to the floor of the ultrasonic atomizer cup with 100% silicone caulk (Gorilla Glue). A 40 mm square computer fan (model OD4010-05HB55, Orion Fans) was used to generate airflow. The voltage delivered to the fan was controlled using a microcontroller (Arduino Micro, Arduino). A darlington transistor (TIP122, STMicroelectronics), 100 Ohm resistor (SparkFun Electronics), 22 and 24 AWG jumper wires (OSEPP Electronics LTD), and 2.1 mm male and female barrel jacks (Centropower) were used. The device was powered using a 9 V battery (Zeus Battery Products).

Non-portable Electronics (**Figures 5.3-5.6**): The ultrasonic atomizer (Comidox) with a frequency of 113 KHz and 730 apertures 5 μm in diameter was adhered to the floor of the ultrasonic atomizer cup with super glue (Ultra Gel Control, Loctite) or 100% silicone caulk (Gorilla Glue). A 40 mm square computer fan (Model AB4010M12**,** HK Fan) was used to generate airflow. The voltage delivered to the fan was controlled by a microcontroller (Arduino Uno, Arduino) and L298N transistor (Qunqi). Two power supplies and 2.1 mm male and female barrel jacks (Centropower) were required.

Simulations (**Figure 5.5**): A computational fluid dynamics (CFD) module in COMSOL Multiphysics v5.5 software was used to simulate the air flow and pressure in different device geometries in a stationary study. A 2D cross-section of our 3D device was modeled. The laminar flow physics interface, governed by the Navier−Stokes equations, was selected to model air flow in the device based on the estimated Reynolds number (Re < 1200). Two fan inlets with a fully developed flow profile, initial flow rate = 6.3 slpm, and an entrance thickness of 0.02 m were used. An outlet boundary was defined by P = 0 Pa with backflow suppressed. No slip boundary conditions were applied to all remaining boundaries. A fine quadrilateral element mesh with extra fine element boundary refinement at the baffles was used.

Fan flow rate measurement (**Figure C3**): The device was attached to a 1 ft long pipe and a hot-wire anemometer (AN-1005) was used to measure the velocity profile at the outlet of the pipe. These velocity measurements were also used for calculations of the sampling flow rate. TSI 1213-20 hot wire probe connected to an anemometer was positioned at the outlet. The anemometer was calibrated for the range of 0.2 m/s - 7 m/s using the standard calibration procedure. The data from the anemometer was collected at a frequency of 10 kHz with a data acquisition module (National Instruments, myRIO-1900) for a sampling time of 30 sec. The experiments showed the maximum velocity was located at the centerline; the profile decays with radial distance. The maximum velocity of the device was ~0.28 m/s for both devices/ fans and flowrate is ~6.3+/-0.7 slpm. Data in **Appendix C, Figure C3**.

Droplet Retention Gravimetric Analysis Using a NonPortable Electronic Setup (**Figure 5.6**): Droplet retention was measured by weighing the ultrasonic atomizer cup filled with water and the 3D printed body separately using an analytical balance (Mettler Toledo ME103E) before and after operating the device for 30 sec with the fan operating at 25% voltage for an airflow rate of 6.3 slpm.

Aerosol Capture Efficiency (**Figure 5.7**): A testing chamber (0.56 × 0.52 × 0.42 m) was used to determine the capture efficiency of our device using fluorescent polystyrene latex (PSL) particles

(Fluoresbrite YG Microspheres, Polysciences Inc.); particle sizes tested: 0.5, 0.75, 1.0, 2.0, and 3.0 μm. The particles were diluted in DI water and aerosolized using a VixOne Nebulizer (Westmed Inc.); each particle size had a dedicated nebulizer to prevent contamination of other particles sizes. An aerodynamic particle sizer (APS 3321, TSI Inc.) was used to monitor the aerosolized particle size and particle concentration during experimental runs. Particle concentration varied with size; see **Table C1** for more information. Three open-face aerosol reference filter holders (EMD Millipore, model #XX5004710) with 0.2 μm PTFE Omnipore membrane filters (Millipore Sigma, product #JGWP04700) were co-located with our air-sampling devices in the chamber to collect particles; filter membranes were collected for analysis. Flow rates for reference filters placed in the chamber were calibrated using a mass flow meter (TSI Inc., model #4140) to 3.15 slpm (half the flow rate of our device due to limitations in the flow controller). A humidity monitor (Extech Instruments, model #SD700; AcuRite, model #01083M) and a dry airline in the chamber were used to keep the humidity between 60% and 70%. The interchangeable particle capture regions were pre-wetted before placing the fully assembled devices in the chamber; the sampling region in the device was replaced between chamber runs. Devices and reference filters captured particles for 25 min followed by a 3 min chamber purge before devices were removed from the chamber. A 1 oz polystyrene cup collected the sample (Uline, product #S-14487) and was weighed (Smart Weigh Pro Pocket Scale TOP500, Amazon) before and after chamber runs. Sampling regions were rinsed with approximately 5 mL of DI water after chamber runs. All samples were diluted to 25 g (25 mL) using DI water which matched the volume of water used for the reference filters. Reference filters were carefully placed in 50 mL polypropylene centrifuge tubes (Thermo Fisher, product #339652) with 25 mL of DI water.

Fluorescence Measurements (**Figure 5.7**): Capture efficiency was calculated as 100 × (fluorescence of samples from our device/fluorescence of the co-located reference filter). Fluorescence measurements were performed using a fluorometer set to a gain of 200 (Sequoia-Turner model 450). Sample cups and centrifuge tubes containing the reference filters were

vortexed (Vortex-Genie 2, Scientific Industries, Inc.) for at least 8 min at 1800 rpm and remained vortexing until analysis. A 5 mL aliquot of the sample was transferred to a 12 × 75 mm borosilicate disposable culture tube (Fisherbrand, cat no. 14-961-26) and discarded to rinse the tube of any previous sample. The sample was re-aliquoted into the test tube, measured, and then discarded for a total of three measurements. Between each aliquot, the pipette was used to resuspend the particles in the sample cup once before measurement. A new glass test tube was used for each particle size on any given day. Blank measurements were always taken when switching to a new glass test tube. Calibration curves for each particle size are available in **Figure C5**. Blank measurement values were subtracted from sample and reference fluorescent values prior to additional calculations and statistical analyses.

Bacteriophage MS2 propagation (**Figure 5.8**): *Escherichia coli* bacteriophage MS2 was propagated using the Adam's Overlay method.[64] Briefly, Tryptic Soy Agar (TSA) plates were prepared and stored at RT overnight. A 2 mL aliquot of an overnight culture of the host species (*E. coli* Famp) was inoculated with 100 µL bacteriophage MS2 and incubated for 1 h at 37 ºC with shaking. An additional 2-3 mL of overnight host culture was then mixed with the 1 h phage MS2 culture and top agar before being poured onto prepared TSA plates for an overnight incubation at 37 ºC. Plates were then washed with 5-10 mL PBS for 5-10 min before top agar was collected, rinsed with chloroform, and centrifuged (4000 x g for 15 min at 4 ºC). Supernatant was then collected and mixed with glycerol for a final composition of 20% glycerol, 80% bacteriophage MS2 before being aliquoted. 1 mL aliquots were stored at -80 ºC until use.

MS2 Aerosolization and Analysis (**Figure 5.8**): A testing chamber operating similarly as the one described previously was used to determine if our device was capable of capturing a bioaerosol (bacteriophage MS2 ATCC #15597-B1). 1 mL of MS2 solution (1.9 × 1011 PFU) was aerosolized (VixOne nebulizer) in a closed chamber. An aerodynamic particle sizer (APS 3321, TSI Inc.) was used to monitor the particle concentration during experimental runs. A 25 min sampling period followed by a 5 min purge was used. Device samples collected in the 1 oz polystyrene cups were

collected with no further dilution. A double-agar layer plaque assay was performed to assess MS2 viability in a bacterial host (*Escherichia coli*). Briefly, tryptic soy agar (TSA) (BD Difco #236950) was prepared following manufacturer's directions, added to Petri dishes (Fisherbrand 100 × 15 mm #FB0875712), and allowed to cool at room temperature. A 10-fold serial dilution was performed using 1X phosphate buffered saline (PBS) for all samples. 100 µL of diluted sample and 100 µL of E. coli Famp (ATCC #700891) suspension were added to 7 mL of top agar (0.5% [w/v] NaCl [Fisher Scientific #S271-500] and 0.7% [w/v] Bacto Agar [BD #214010]) in a borosilicate glass tube (Fisherbrand #14-961-27), after which the solution was mixed by rolling tube between hands and subsequently poured on the prepared TSA plates; top agar was cooled before plates were inverted and incubated overnight at 37 °C. The plaques were counted the following day. The assay was performed in duplicate for all sample dilutions, including undiluted samples. Additionally, a negative control (only *E. coli*) and PBS control (PBS added in place of the sample) were also included.

Data Analysis: All data and statistical analyses were performed using Prism v9.0 (GraphPad) software.

5.9 References

1. J. H. Ware, J. D. Spengler, L. M. Neas, J. M. Samet, G. R. Wagner, D. Coultas, H. Ozkaynak and M. Schwab, Respiratory and irritant health effects of ambient volatile organic compounds. The Kanawha County Health Study, *Am. J. Epidemiol.*, 1993, **137**, 1287–1301.
2. G. P. Pappas, R. J. Herbert, W. Henderson, J. Koenig, B. Stover and S. Barnhart, The respiratory effects of volatile organic compounds, *Int. J. Occup. Environ. Health*, 2000, **6**, 1–8.
3. J. E. Thompson, Airborne Particulate Matter: Human Exposure and Health Effects, *J. Occup. Environ. Med.*, 2018, **60**, 392–423.
4. I. Manisalidis, E. Stavropoulou, A. Stavropoulos and E. Bezirtzoglou, Environmental and Health Impacts of Air Pollution: A Review, *Front. Public Heal.*, 2020, **8**, 14.
5. E. R. Tovey, M. D. Chapman, C. W. Wells and T. A. E. Platts-Mills, The distribution of dust mite allergen in the houses of patients with asthma, *Am. Rev. Respir. Dis.*, 1981, **124**, 630–635.
6. B. J. Apelberg, L. M. Hepp, E. Avila-Tang, L. Gundel, S. K. Hammond, M. F. Hovell, A. Hyland, N. E. Klepeis, C. C. Madsen, A. Navas-Acien, J. Repace, J. M. Samet and P. N. Breysse, Environmental monitoring of secondhand smoke exposure, *Tob. Control*, 2013, **22**, 147–155.
7. C. A. Pope and D. W. Dockery, Health effects of fine particulate air pollution: lines that

connect, *J. Air Waste Manag. Assoc.*, 2006, **56**, 709–742.
8. J. Y. Choi, J. Zemke, S. E. Philo, E. S. Bailey, M. Yondon and G. C. Gray, Aerosol Sampling in a Hospital Emergency Room Setting: A Complementary Surveillance Method for the Detection of Respiratory Viruses, *Front. Public Heal.*, 2018, **6**, 174.
9. R. E. Stockwell, E. L. Ballard, P. O'Rourke, L. D. Knibbs, L. Morawska and S. C. Bell, Indoor hospital air and the impact of ventilation on bioaerosols: a systematic review, *J. Hosp. Infect.*, 2019, **103**, 175–184.
10. C. Alonso, P. C. Raynor, S. Goyal, B. A. Olson, A. Alba, P. R. Davies and M. Torremorell, Assessment of air sampling methods and size distribution of virus-laden aerosols in outbreaks in swine and poultry farms, *J. Vet. Diagnostic Investig.*, 2017, **29**, 298–304.
11. M. Śmiełowska, M. Marć and B. Zabiegała, Indoor air quality in public utility environments-a review, *Environ. Sci. Pollut. Res. Int.*, 2017, **24**, 11166–11176.
12. Y. Wu, A. Calis, Y. Luo, C. Chen, M. Lutton, Y. Rivenson, X. Lin, H. C. Koydemir, Y. Zhang, H. Wang, Z. Göröcs and A. Ozcan, Label-Free Bioaerosol Sensing Using Mobile Microscopy and Deep Learning, *ACS Photonics*, 2018, **5**, 4617–4627.
13. P. Srikanth, S. Sudharsanam and R. Steinberg, Bio-aerosols in indoor environment: composition, health effects and analysis, *Indian J. Med. Microbiol.*, 2008, **26**, 302–312.
14. J. Namieśnik, B. Zabiegała, A. Kot-Wasik, M. Partyka and A. Wasik, Passive sampling and/or extraction techniques in environmental analysis: a review, *Anal. Bioanal. Chem. 2004 3812*, 2004, **381**, 279–301.
15. I. Lee, Y. Seok, H. Jung, B. Yang, J. Lee, J. Kim, H. Pyo, C. S. Song, W. Choi, M. G. Kim and J. Lee, Integrated Bioaerosol Sampling/Monitoring Platform: Field-Deployable and Rapid Detection of Airborne Viruses, *ACS sensors*, 2020, **5**, 3915–3922.
16. J. Volckens, C. Quinn, D. Leith, J. Mehaffy, C. S. Henry and D. Miller-Lionberg, Development and evaluation of an ultrasonic personal aerosol sampler, *Indoor Air*, 2017, **27**, 409–416.
17. T. Reponen, Sampling for microbial determinations, *Expo. to Microbiol. Agents Indoor Occup. Environ.*, 2017, 85–96.
18. J. Kesavan and J. L. Sagripanti, Evaluation criteria for bioaerosol samplers, *Environ. Sci. Process. Impacts*, 2015, **17**, 638–645.
19. C. H. Wang, B. T. Chen, B. C. Han, A. C. Y. Liu, P. C. Hung, C. Y. Chen and H. J. Chao, Field evaluation of personal sampling methods for multiple bioaerosols, *PLoS One*, , DOI:10.1371/JOURNAL.PONE.0120308.
20. S. A. Grinshpun, M. P. Buttner, G. Mainelis and K. Willeke, Sampling for Airborne Microorganisms, *Man. Environ. Microbiol.*, 2015, 3.2.2–1.
21. V. Aizenberg, T. Reponen, S. A. Grinshpun and K. Willeke, Performance of Air-O-Cell, Burkard, and Button Samplers for total enumeration of airborne spores, *AIHAJ*, 2000, **61**, 855–864.
22. G. E. Duncan, E. Seto, A. R. Avery, M. Oie, G. Carvlin, E. Austin, J. H. Shirai, J. He, B. Ockerman and I. Novosselov, Usability of a Personal Air Pollution Monitor: Design-Feedback Iterative Cycle Study, *JMIR mHealth uHealth*, , DOI:10.2196/12023.
23. M. Gao, J. Cao and E. Seto, A distributed network of low-cost continuous reading sensors to measure spatiotemporal variations of PM2.5 in Xi'an, China, *Environ. Pollut.*, 2015, **199**, 56–65.
24. E. Seto, E. Austin, I. Novosselov and M. Yost, in *International Congress on Environmental Modelling and Software*, 2014.
25. J. Burkart, G. Steiner, G. Reischl, H. Moshammer, M. Neuberger and R. Hitzenberger, Characterizing the performance of two optical particle counters (Grimm OPC1.108 and OPC1.109) under urban aerosol conditions, *J. Aerosol Sci.*, 2010, **41**, 953–962.
26. J. M. Roux, R. Sarda-Estève, G. Delapierre, M. H. Nadal, C. Bossuet and L. Olmedo, Development of a new portable air sampler based on electrostatic precipitation, *Environ. Sci. Pollut. Res. Int.*, 2016, **23**, 8175–8183.

27. T. T. Han, N. M. Thomas and G. Mainelis, Design and development of a self-contained personal electrostatic bioaerosol sampler (PEBS) with a wire-to-wire charger, 2017, **51**, 903–915.
28. T. G. Foat, W. J. Sellors, M. D. Walker, P. A. Rachwal, J. W. Jones, D. D. Despeyroux, L. Coudron, I. Munro, D. K. McCluskey, C. K. L. Tan and M. C. Tracey, A prototype personal aerosol sampler based on electrostatic precipitation and electrowetting-on-dielectric actuation of droplets, *J. Aerosol Sci.*, 2016, **95**, 43–53.
29. I. V. Novosselov, R. A. Gorder, J. A. Van Amberg and P. C. Ariessohn, Design and Performance of a Low-Cost Micro-Channel Aerosol Collector, 2014, **48**, 822–830.
30. J. He, N. K. Beck, A. L. Kossik, J. Zhang, E. Seto, J. S. Meschke and I. Novosselov, Evaluation of micro-well collector for capture and analysis of aerosolized Bacillus subtilis spores, *PLoS One*, , DOI:10.1371/JOURNAL.PONE.0197783.
31. K. A. Koehler and T. M. Peters, New Methods for Personal Exposure Monitoring for Airborne Particles, *Curr. Environ. Heal. reports*, 2015, **2**, 399–411.
32. R. Chartier, M. Phillips, P. Mosquin, M. Elledge, K. Bronstein, S. Nandasena, V. Thornburg, J. Thornburg and C. Rodes, A comparative study of human exposures to household air pollution from commonly used cookstoves in Sri Lanka, *Indoor Air*, 2017, **27**, 147–159.
33. J. Cai, B. Yan, J. Ross, D. Zhang, P. L. Kinney, M. S. Perzanowski, K. H. Jung, R. Miller and S. N. Chillrud, Validation of MicroAeth® as a Black Carbon Monitor for Fixed-Site Measurement and Optimization for Personal Exposure Characterization, *Aerosol air Qual. Res.*, 2014, **14**, 1–9.
34. Z. Wang, T. Reponen, S. A. Grinshpun, R. L. Górny and K. Willeke, Effect of sampling time and air humidity on the bioefficiency of filter samplers for bioaerosol collection, *J. Aerosol Sci.*, 2001, **32**, 661–674.
35. W. D. Griffiths, I. W. Stewart, J. M. Clark and I. L. Holwill, Procedures for the characterisation of bioaerosol particles. Part II: Effects of environment on culturability, *Aerobiologia (Bologna).*, 2001, **17**, 109–119.
36. J. R. Kastner and K. C. Das, Wet scrubber analysis of volatile organic compound removal in the rendering industry, *J. Air Waste Manag. Assoc.*, 2002, **52**, 459–469.
37. D. Mussatti and P. Hemmer, in *EPA Air Pollution Control Cost Manual*, United States Environmental Protection Agency, North Carolina, 6th edn., 2002.
38. C. H. Jung and K. W. Lee, Approximated Solution for The Most Penetrating Particle Size in Multiple Fluid Sphere Systems, 2007, **24**, 257–266.
39. T. Gemci and F. Ebert, Prediction of the particle capture efficiency based on the combined mechanisms (turbulent diffusion, inertial impaction, interception, and gravitation) by a 3-D simulation of a wet scrubber, *J. Aerosol Sci.*, 1992, **23**, 769–772.
40. H. T. Kim, C. H. Jung, S. N. Oh and K. W. Lee, Particle Removal Efficiency of Gravitational Wet Scrubber Considering Diffusion, Interception, and Impaction, 2004, **18**, 125–136.
41. K. W. Lee, Maximum penetration of aerosol particles in granular bed filters, *J. Aerosol Sci.*, 1981, **12**, 79–87.
42. J. Kim, J. J. Kim and S. J. Lee, Efficient removal of indoor particulate matter using water microdroplets generated by a MHz-frequency ultrasonic atomizer, *Build. Environ.*, 2020, **175**, 106797.
43. E. Berthier, A. M. Dostie, U. N. Lee, J. Berthier and A. B. Theberge, Open Microfluidic Capillary Systems, *Anal. Chem.*, 2019, **91**, 8739–8750.
44. B. P. Casavant, E. Berthier, A. B. Theberge, J. Berthier, S. I. Montanez-Sauri, L. L. Bischel, K. Brakke, C. J. Hedman, W. Bushman, N. P. Keller and D. J. Beebe, Suspended microfluidics, *Proc. Natl. Acad. Sci. U. S. A.*, 2013, **110**, 10111–10116.
45. L. J. Clancy, Aerodynamics, 1975, 610.
46. P. Fillingham, H. Murali and I. V. Novosselov, Nondimensional Parameter for Characterization of Wall Shear Stress from Underexpanded Axisymmetric Impinging Jets, *J.*

Fluids Eng. Trans. ASME, , DOI:10.1115/1.4037035/372470.
47. P. Fillingham and I. V. Novosselov, Wall jet similarity of impinging planar underexpanded jets, *Int. J. Heat Fluid Flow*, 2020, **81**, 108516.
48. R. K. Chakrabarty, I. V. Novosselov, N. D. Beres, H. Moosmüller, C. M. Sorensen and C. B. Stipe, Trapping and aerogelation of nanoparticles in negative gravity hydrocarbon flames, *Appl. Phys. Lett.*, 2014, **104**, 243103.
49. J. Davis, K. Tiwari and I. Novosselov, Soot Morphology and Nanostructure in Complex Flame Flow Patterns via Secondary Particle Surface Growth, *Fuel (London, England)*, 2019, **245**, 447–457.
50. J. W. Cleaver and B. Yates, Mechanism of detachment of colloidal particles from a flat substrate in a turbulent flow, *J. Colloid Interface Sci.*, 1973, **44**, 464–474.
51. M. E. O'Neill, A sphere in contact with a plane wall in a slow linear shear flow, *Chem. Eng. Sci.*, 1968, **23**, 1293–1298.
52. P. Fillingham, K. Kottapalli, X. Zhan and I. V. Novosselov, Characterization of adhesion force in aerodynamic particle resuspension, *J. Aerosol Sci.*, 2019, **128**, 89–98.
53. P. Fillingham, R. S. Vaddi, A. Bruning, G. Israel and I. V. Novosselov, Drag, lift, and torque on a prolate spheroid resting on a smooth surface in a linear shear flow, *Powder Technol.*, 2021, **377**, 958–965.
54. J. Blazek, *Computational Fluid Dynamics: Principles and Applications*, Elsevier, 3rd edn., 2015.
55. R. C. Petersen, A. G. Hallar, I. B. McCubbin, J. A. Ogren, E. Andrews, D. Lowenthal, R. Gorder, R. Purcell, D. Sleeth and I. Novosselov, Numerical, wind-tunnel, and atmospheric evaluation of a turbulent ground-based inlet sampling system, 2019, **53**, 712–727.
56. W. G. Lindsley, B. J. Green, F. M. Blachere, S. B. Martin, B. F. Law, P. A. Jensen and M. P. Schafer, in *NIOSH Manual of Analytical Methods*, 5th edn., 2017, pp. 2–115.
57. J. He and I. V. Novosselov, Design and Evaluation of an Aerodynamic Focusing Micro-Well Aerosol Collector, *Aerosol Sci. Technol.*, 2017, **51**, 1016–1026.
58. J. Gordon, P. Gandhi, G. Shekhawat, A. Frazier, J. Hampton-Marcell and J. A. Gilbert, A simple novel device for air sampling by electrokinetic capture, *Microbiome*, 2015, **3**, 79.
59. H. R. An, G. Mainelis and M. Yao, Evaluation of a high-volume portable bioaerosol sampler in laboratory and field environments, *Indoor Air*, 2004, **14**, 385–393.
60. S. E. Mischler, E. G. Cauda, M. Di Giuseppe and L. A. Ortiz, A multi-cyclone sampling array for the collection of size-segregated occupational aerosols, *J. Occup. Environ. Hyg.*, 2013, **10**, 685–693.
61. H. J. Walls, D. S. Ensor, L. A. Harvey, J. H. Kim, R. T. Chartier, S. V. Hering, S. R. Spielman and G. S. Lewis, Generation and sampling of nanoscale infectious viral aerosols, *Aerosol Sci. Technol.*, 2016, **50**, 802–811.
62. G. T. Machado, C. R. de C. Pinto, L. A. V. da Fonseca, T. C. dos S. Ramos, T. F. P. Paggi and B. Spira, Bacteriophages as surrogates for the study of viral dispersion in open air, *Arch. Microbiol.*, 2021, **203**, 4041–4049.
63. Manual of Environmental Microbiology, *Man. Environ. Microbiol.*, DOI:10.1128/9781555815882.
64. M. H. Adams, *Bacteriophages*, Interscience Publishers, 1959.

Chapter 6 | Conclusions and Outlooks

Analytical tools and methods will always be needed to study biological processes in several applications ranging from general discovery in basic science to answering targeted questions about specific interactions. This dissertation describes the addition of new tools for the bioanalytical toolbox. The technologies and methods discussed have been developed with the end-user in mind, with ease of use being a primary consideration without compromising the overall elegance or effectiveness of the methodology. Thus, the hope for the material presented in this dissertation is ultimately its translation and use in uncovering new knowledge in the human health and environmental fields of study.

All biological processes are driven by cell signaling whether the cue is mechanical, electrical, chemical, or some combination. Of the three, chemical cues in paracrine signaling are challenging to measure and characterize as they are transient and often have a short half-life. Additionally, since chemical signals can impact multiple pathways, it can be difficult to understand what the primary role of a signal is and how that signal is contributing to physiological and function changes in biological processes. Chapter 2 introduced the development and characterization of a new bead-based immunoassay approach in which dual-functionalized beads enabled localized cell-surface sampling of a monoculture. This approach showed the protection of a cell-secreted analyte in the presence and absence of a neutralization factor. Chapter 3 builds upon this work and investigates the trafficking of a cell-secreted molecule between two cell types, showing its application in monitoring paracrine signaling. These two chapters taken together highlight how dual-functionalized beads can be used to potentially discover new knowledge in cell signaling by taking a closer look at how chemical signals move within cell culture models.

With the arrival of new manufacturing techniques like 3D printing, injection molding, or micromilling, unique cell culture platforms have been possible to create on faster timelines. Chapter 4 explores the adaptation of injection-molded inserts for cell culture in several biological applications. Furthermore, it outlines engineering and non-engineering controls for the practical

use of these well-plate inserts; this has helped facilitated its translation and use to different research groups. More importantly, this work added to the currently available tools researchers have for studying cell signaling by enabling added complexity of 2D culture systems. Chapter 4 also introduced a new approach for creating free-standing lumen structures as an alternative to using animal-derived counterparts (e.g., excised animal vessels). Not only is this method user-friendly, but the dimensions can be altered, different biologically relevant materials can be utilized (e.g., designer hydrogels, extracellular matrix components, polymers), and it helps reduce the reliance on animal models which are not always relevant to human health.

In some cases, questions cannot be answered because the technologies do not exist or are insufficient to fully investigate the questions which leads to the development of new technologies. Chapter 5 details the development of a new air sampling device for investigating the impact of environmental exposures on human health. Current methods for sampling bioaerosols require trained professionals to collect samples which is inaccessible to a wide range of society. By incorporating fluidic features, the new sampling technology maintains the viability of bioaerosols for further study. Future work will need to dive deeper into investigating a wider range of bioaerosols as well as improve upon the overall design of the device to make it more efficient.

The methodologies described in this dissertation are well poised to expand the types of questions researchers can ask and study. These tools aim to highlight innovations in the analytical and measurement science fields and demonstrate how our bioanalytical toolbox can be updated as new advancements become available. Further progress in fully characterizing these methods should be conducted, with continuous updates to protocols and use as needed. Finally, methods such as these should be translated into other interdisciplinary fields where new strategies and approaches can hopefully be used to explore a wide range of questions.

Appendix

A. Supplementary Information for Chapter 2

Reproduced in part from T.L. van Neel, S.B. Berry,* E. Berthier, and A.B. Theberge, "Localized cell-surface sampling of a secreted factor using cell-targeting beads." Analytical Chemistry,* **2020***, 92, 13634-13640.*
** Equal contribution*

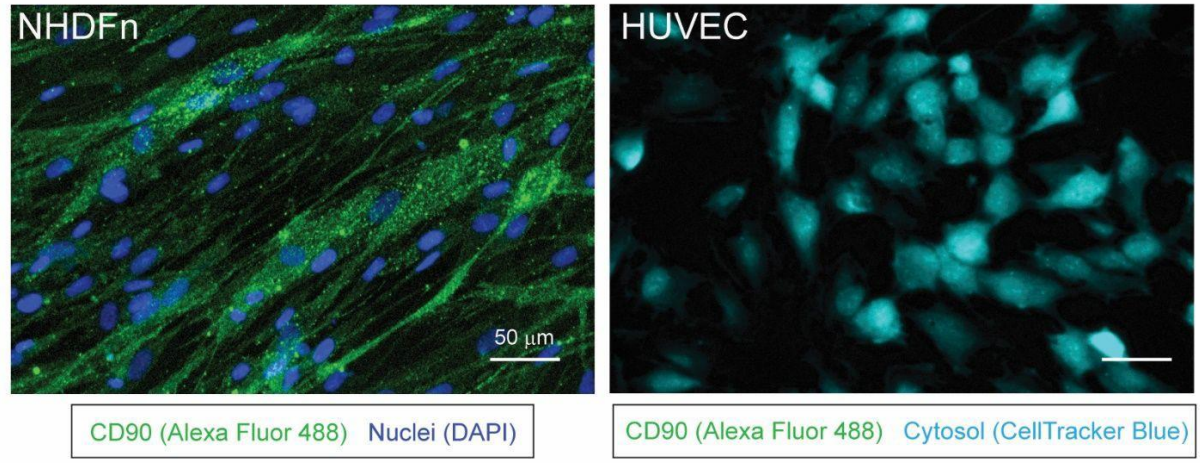

Figure A1. Validation of CD90 expression by NHDFn cells using immunocytochemistry. CD90 expression (green) was confirmed in NHDFn ($CD90^+$ cells) using standard immunocytochemistry techniques. HUVECs ($CD90^-$ cells) were stained with CellTracker Blue (light blue) and did not show CD90 expression (no green signal observed). Scale bar is 50 μm.

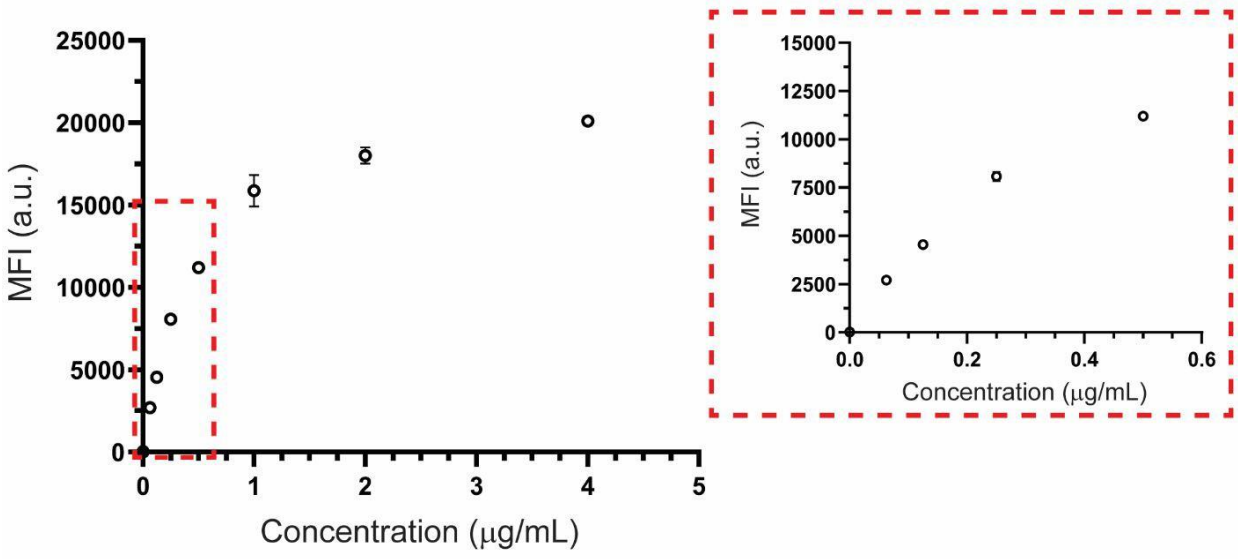

Figure A2. Validation of antibody functionalization on MagPlex bead surface. Antibodies (CD90 and HGF) were covalently coupled to the bead surface and then incubated with a range of fluorescent secondary antibody concentrations to demonstrate successful coupling of antibodies to bead surface (see Materials and Methods for details). The plot reflects an expected response based on the manufacturer's (Luminex) protocol.[1] Data points are the average of duplicate measurements with error bars representing standard deviation. The graph on the right is an inset of the 0-0.5 μg/mL concentration range.

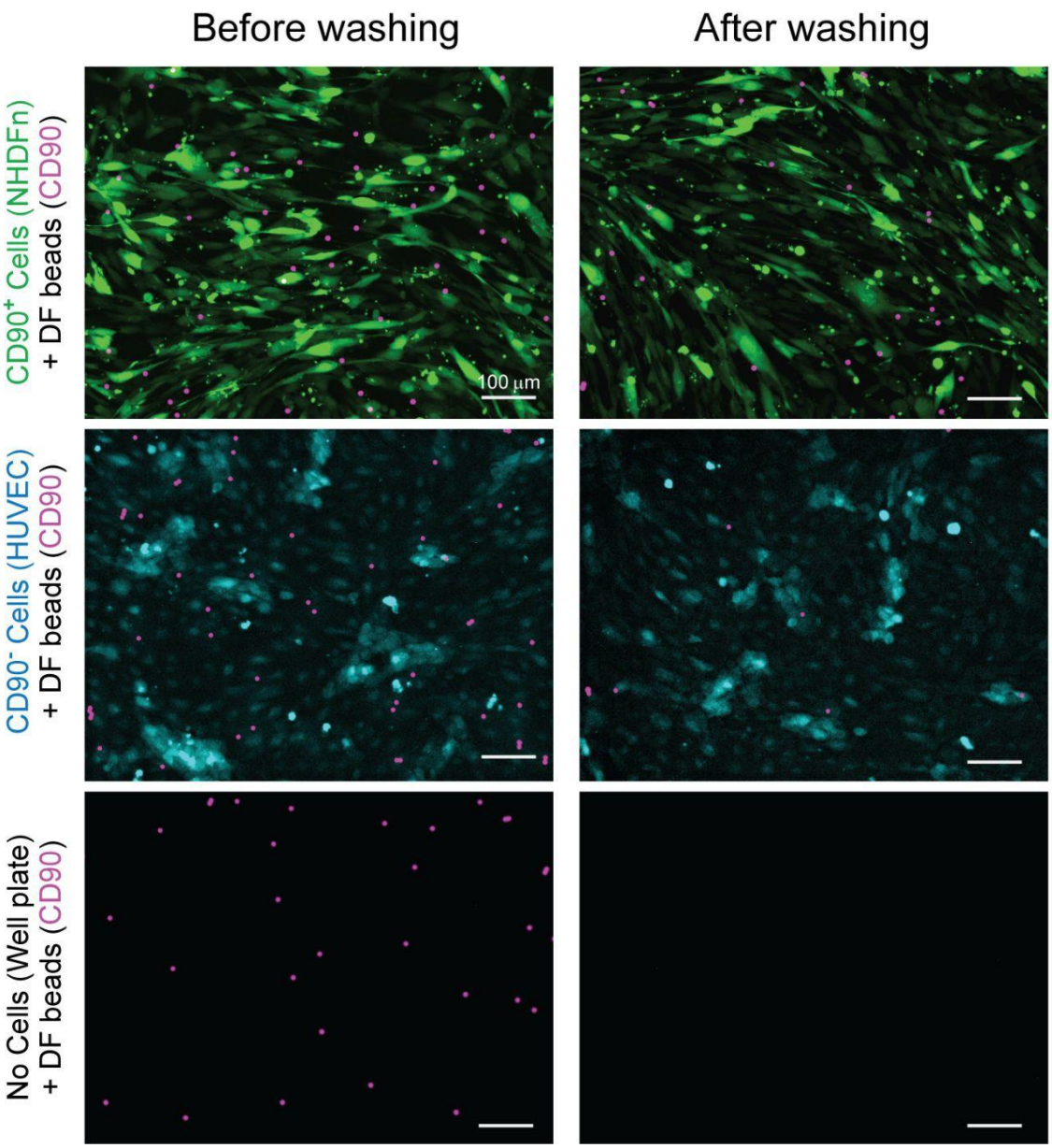

Figure A3. Validation of dual-functionalized (DF) bead binding to the surface of targeted CD90^{+} cells (NHDFn). Representative images from n=3 independent experiments demonstrating DF bead [(anti-CD90, anti-HGF) (pink)] tethering to NHDFn cells (green) after multiple washing steps. Bead retention was also quantified in two negative control conditions where bead retention after washing is not expected: anti-CD90, anti-HGF DF beads with CD90^{-} cells [(HUVECs) (blue)]; anti-CD90, anti-HGF DF beads in a well plate with no cells. All negative conditions showed negligible bead retention on the cell/well plate surface. Images are representative of 3 independent experiments. Bead retention data is quantified in **Figure 2.3C** and **Table A1**. Scale bar is 100 µm.

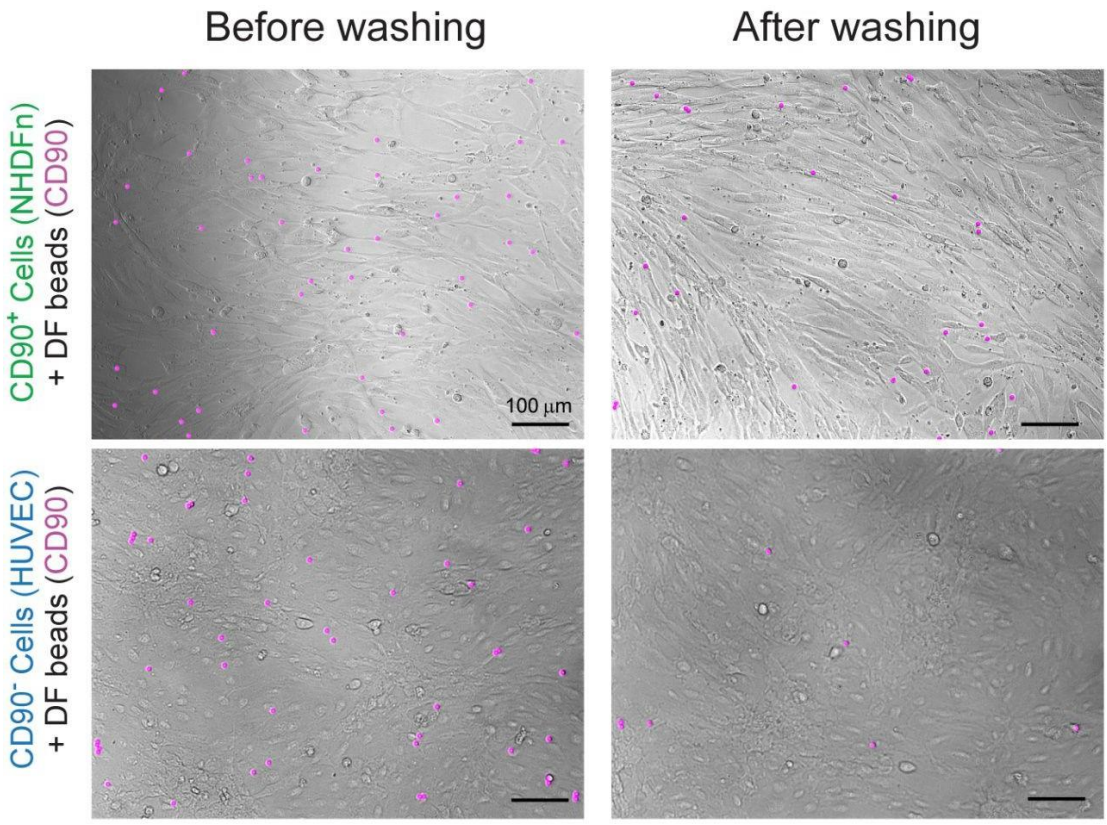

Figure A4. Phase contrast imaging of dual-functionalized beads binding to the surface of targeted $CD90^+$ cells (NHDFn). Here we can see DF beads remaining after washing are bound to the surface of targeted $CD90^+$ cells. In the non-targeted $CD90^-$ cell condition, remaining beads are mostly on the well plate surface. Fields of view correspond to the images shown in **Figure A3** and were taken at 10X magnification. A fluorescence microscopy overlay of the DF beads (pink) was used for better visualization. Higher magnification (20X) images are shown in **Figure A5**. Scale bar is 100 µm.

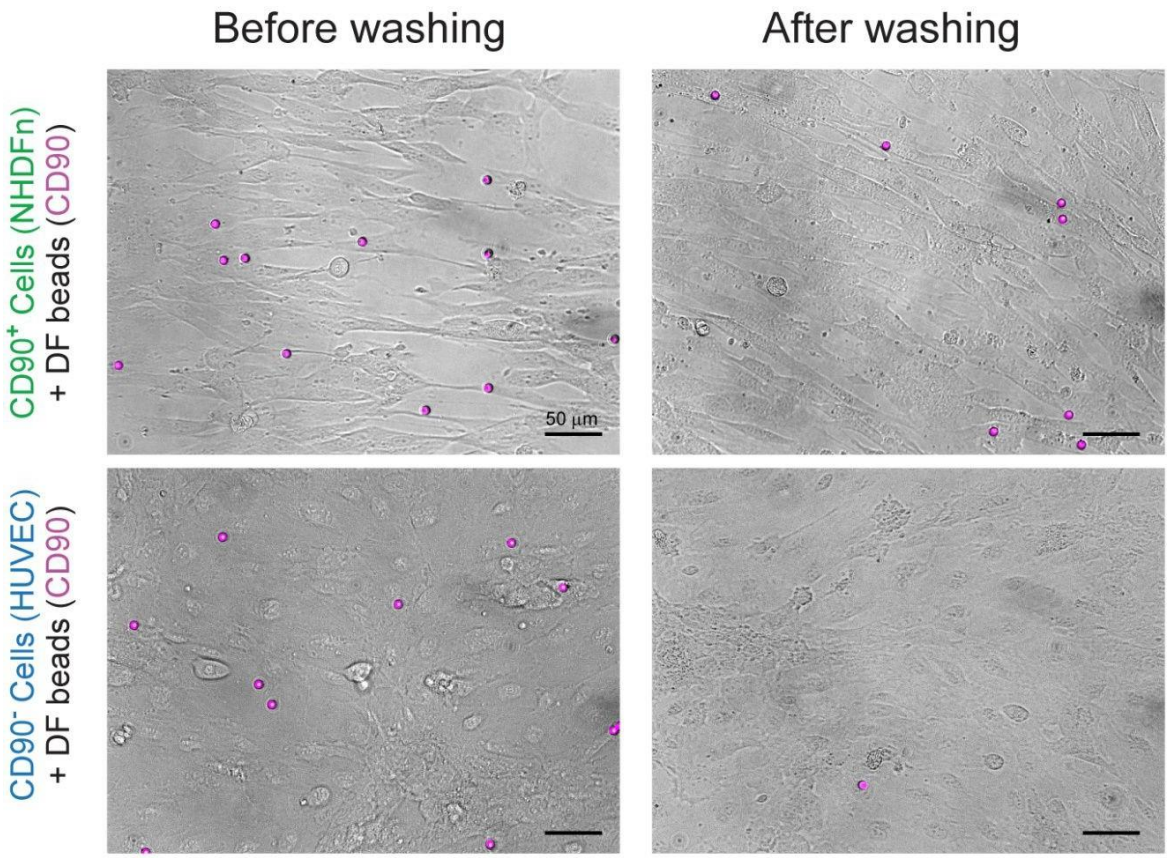

Figure A5. 20X magnification phase contrast imaging of dual-functionalized beads binding to the surface of targeted $CD90^+$ cells (NHDFn). Fields of view are insets of the images shown in **Figure A4**. A fluorescence microscopy overlay of the DF beads (pink) was used for better visualization. Scale bar is 50 µm.

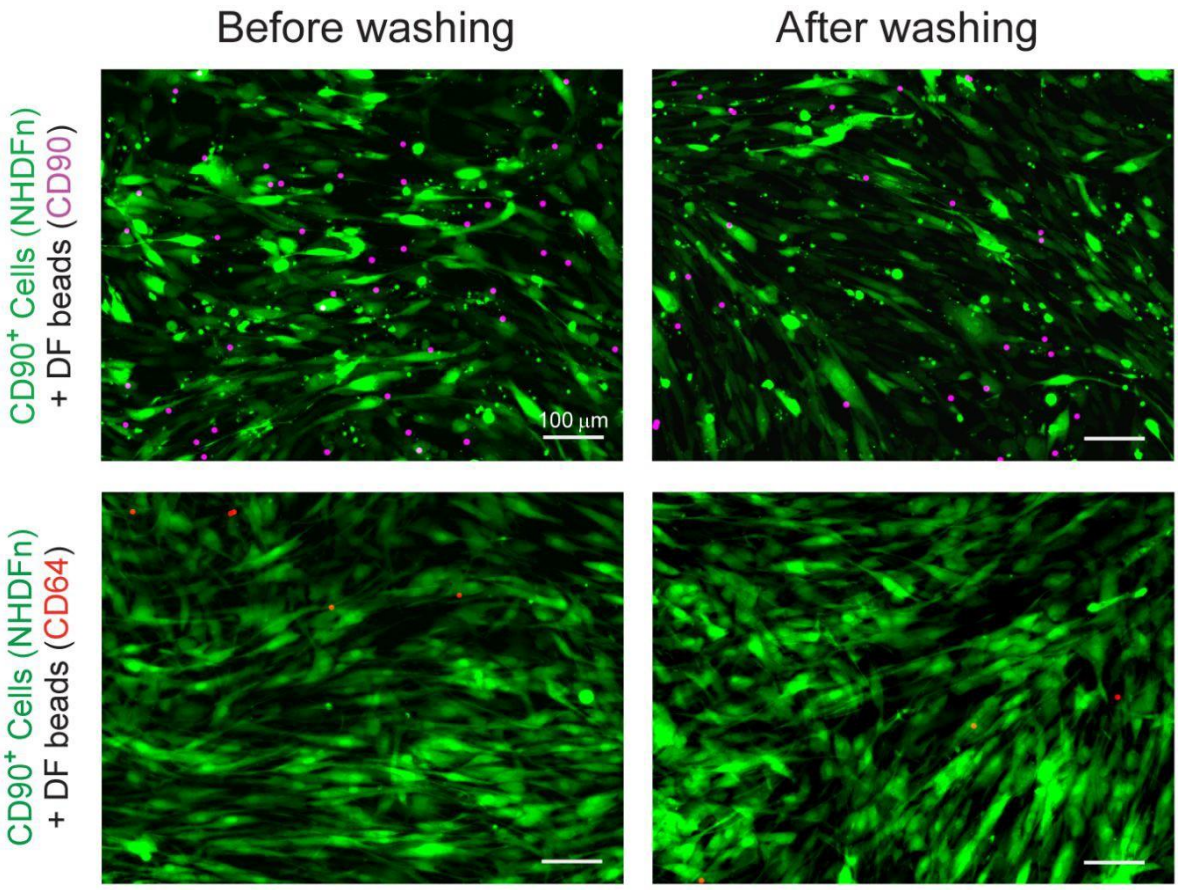

Figure A6. Validation of CD90$^+$ cells (NHDFn) selectively binding anti-CD90, anti-HGF DF beads. Representative images from n=3 independent experiments demonstrating DF bead [(anti-CD90, anti-HGF) (pink)] tethering to NHDFn cells (green) after multiple washing steps. Bead retention was also quantified in a DF bead negative control condition using beads functionalized with anti-CD64 and anti-MMP12 (red). Bead retention on NHDFn of anti-CD64, anti-MMP12 after washing is not expected. Images and bead quantification data showed negligible bead retention on the cell/well plate surface (**Table A1**). Scale bar is 100 µm.

Table A1. Total bead counts for bead-cell binding validation. The table shows the average bead count ± standard deviation (SD) for the representative images used in **Figure 2.3**, **A3**, and **A6**. Each condition included n=9 images for n=3 independent experiments.

Condition	Before washing (average ± SD)	After washing (average ± SD)
$CD90^+$ Cells (NHDFn) + DF beads (CD90)	29.4 ± 6.6	21.0 ± 4.7
$CD90^+$ Cells (NHDFn) + DF beads (CD64)	8.4 ± 2.8	1.6 ± 1.3
$CD90^-$ Cells (HUVEC) + DF beads (CD90)	29.3 ± 3.6	3.3 ± 2.4
No Cells (Well plate) + DF beads (CD90)	27.6 ± 6.2	1.2 ± 1.5

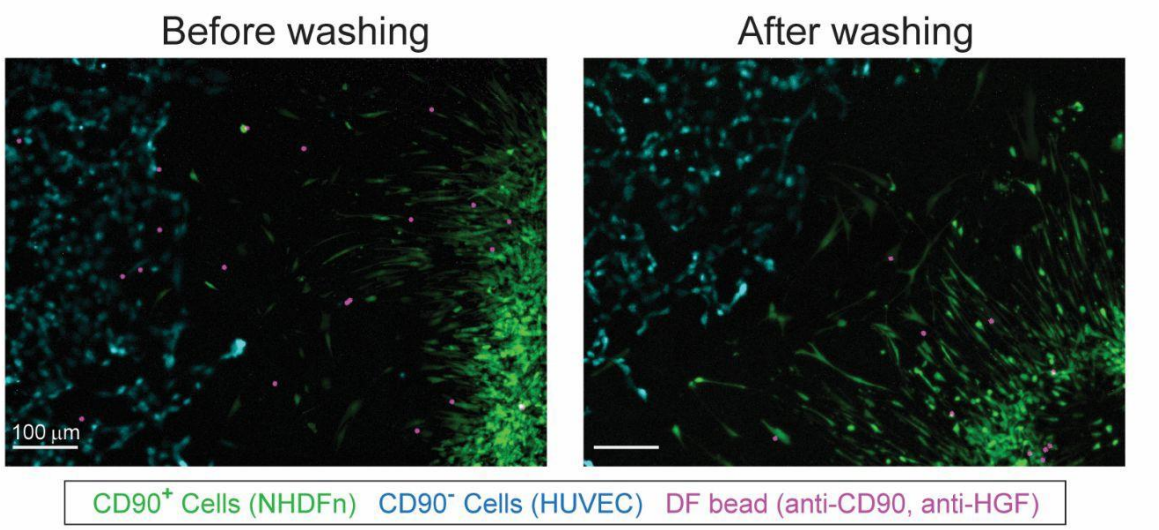

Figure A7. Dual-functionalized (DF) beads (anti-CD90, anti-HGF) remain tethered to targeted $CD90^+$ cells (NHDFn) in coculture with $CD90^-$ cells (HUVEC). DF beads (pink) were added to a patterned coculture of NHDFn (green) and HUVEC (blue) cells for a 2-hour incubation followed by multiple wash steps. Beads remain tethered to $CD90^+$ cells (green), while being removed from $CD90^-$ cells (blue) after washing. Scale bar is 100 µm.

Table A2. Experimental reproducibility of mono- and dual-functionalized (MF and DF, respectively) bead methods. The table includes the relative standard deviation (RSD) for each experiment plotted in **Figure 2.4**. More variability exists within the MF bead system (traditional method), while the DF bead system (our new method) is consistently below 15%.

	Control (- anti-HGF)		Treated (+ anti-HGF)	
	MF bead	DF bead	MF bead	DF bead
Experiment	RSD (%)			
1	37.6	14.4	28.9	11.6
2	14.3	8.6	15.7	12.5
3	7.7	1.1	12.6	11.7
4	61.4	4.6	53.9	13.2

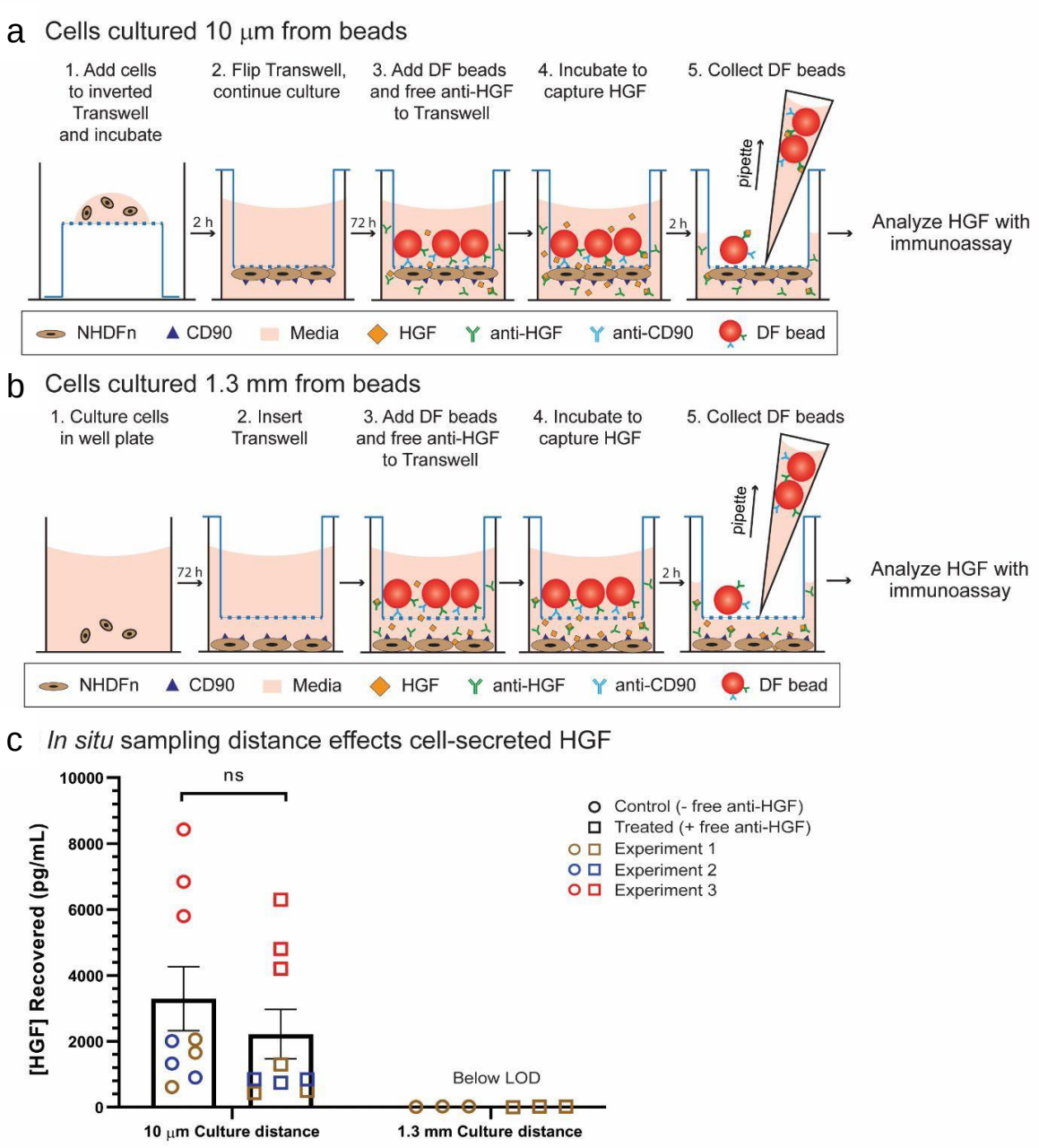

Figure A8. Increased in situ HGF recovered concentration results from bead proximity to cells. Schematic showing steps for culturing cells (a) 10 μm from beads and (b) 1.3 mm from beads. In both conditions, DF beads are spatially separated from cells and are not attached to the cells. These two distances were chosen to probe the effect of bead sampling distance on HGF capture. When beads were cultured 10 μm from cells there was (c) no statistical significance between the control (- free anti-HGF) and treated (+ free anti-HGF) groups. This same trend was observed when beads were tethered to the cell surface via CD90 (see **Figure 2.3**). In contrast, beads cultured 1.3 mm from the cells resulted in signals below the assay limit of detection (LOD) in both conditions. Three independent experiments with three replicates were performed for each experiment. Error bars are SEM. Unpaired, parametric t-test.

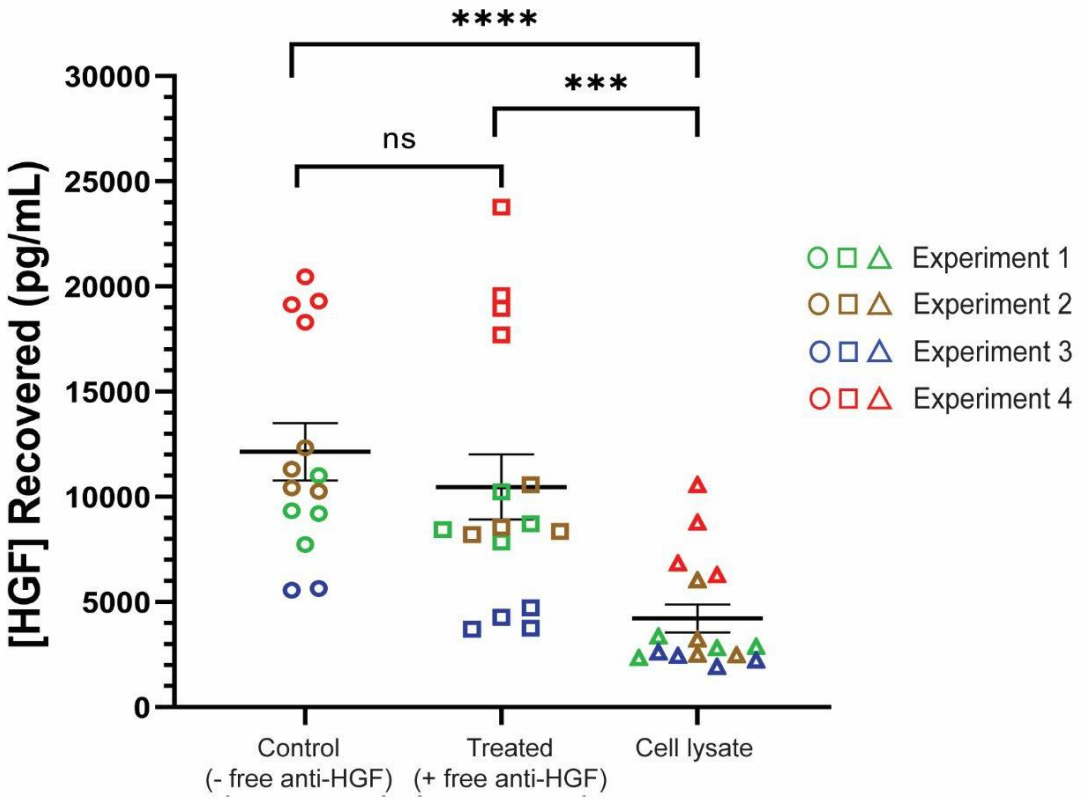

Figure A9. Quantification of HGF in cell lysate from the cell lysis step to remove DF beads tethered on cell surface. To determine the contribution of intracellular HGF to total recovered HGF signal, we quantified the amount of HGF present during the 15 min lysing period used in the localized cell-surface sampling method workflow by simultaneously adding DF beads and lysis buffer to cells. While signal is observed in the cell lysate, the HGF concentration is significantly less than the recovered HGF from either localized cell-surface sampling condition (control and treated). Control and treated conditions were replotted from **Figure 2.3**. Each data point plotted represents one technical replicate, with typically 4 replicates per independent experiment. Error bars are SEM. Unpaired, parametric t-test. *** $p < 0.001$, **** $p < 0.0001$.

References:

1. Angeloni, S.; Das, S.; Dunbar, S.; Stone, V.; Swift, S. *XMAP Cookbook: A Collection of Methods and Protocols for Developing Multiplex Assays with XMAP Technology*, 4th ed. **2018**, Austin (TX), Luminex.

B. Supplementary Information for Chapter 4

a. 4.1. Freestanding hydrogel lumens for modeling blood vessels and vasodilation

Reproduced in part from A.M. Dostie, H.G. Lea*, U.N. Lee*, T.L. van Neel, E. Berthier, A.B. Theberge "Freestanding hydrogel lumens for modeling blood vessels and vasodilation." SLAS Technologies,* ***2022****, 27, 344-349.*
** Equal contribution*

Additional discussion for Method 2 and vasoactivity experiments

We evaluated the reproducibility of this method in two separate experiments with two devices of the same design (12 total collagen rings per experiment) in each experiment. While the rings can fit in a 96- well plate as shown in **Figure 4.1.1 b**, the light from the imaging set up used to measure the rings reflects off the bottom of the concave meniscus, causing a glare over the collagen ring and impeding proper imaging. In a larger well plate, such as the 24-well plate, a glare was still present when imaging; however due to the larger diameter of the well relative to the collagen ring, the glare does not cover the ring (**Figure B1 a**). This is important because when measuring the ring with ImageJ, the glare and white color of the collagen ring appear the same color which prevents the imaging software from differentiating the two areas.

The designed dimensions for the collagen rings were 3 mm outer diameter and 1 mm inner diameter. Overall, the actual inner diameter, outer diameter, and wall thickness were smaller than designed (**Figure B1 bi** and **B1 bii**). The average outer diameter for each device ranged from 2.48 to 2.73 mm, a difference of 250 μm and the average inner diameter ranged from 0.76 to 0.81 mm, a difference of 40 μm. The difference can be attributed to the measurement technique (described in the Methods section). Additionally, standard deviations can be attributed to the measurement technique and inherent differences that occur in 3D printed devices. However, ultimately it is not critical to minimize the standard deviation across hydrogel rings because when an assay is performed with the rings the measurement made is the percent change in outer and inner diameter or area over time.

While Method 1 (**Figure 4.1.1**) works well for arrayed generation of hydrogel rings, we also sought to develop a method to make individual hydrogel rings with a simpler setup, avoiding the need to use F127 and multiple pieces (spacer, Teflon tubes, etc.). Method 2 uses a commercially available syringe that has been adapted to form collagen rings by cutting off the tip of the syringe and inserting a 3D printed core. Collagen laden with smooth muscle cells was then pipetted into the syringe and incubated to allow the collagen to gel. The 3D printed core was then pushed upwards (**Figure B1 a**), revealing the collagen ring, and the ring was transferred to a well plate with cell culture media for storage. Following 5 days in culture, cell-laden hydrogel rings were submerged in a buffer (Tyrode's Solution) and treated with either a control (additional Tyrode's Solution) or a vasodilator (fasudil). The collagen rings were recorded for 20 min using a stereoscope to monitor any change in geometry and size. This imaging setup is cost effective (<$500 USD) and does not require specialized training to record the collagen rings. Images obtained from these recordings were analyzed using ImageJ, a free imaging processing software, to determine the change in percent area of the rings over time (**Figures B1** and **B3**). A significant difference in ring area was observed when hydrogel rings were treated with a control (buffer) compared to the vasodilator (fasudil). We note that as the cells interact with the hydrogel, the mechanical stress experienced by the cells offers cues for cellular behavior and thus may affect the overall size change.[1,2]

Additional Materials and Methods

Fabrication of device to mold hydrogel rings in Method 2 (**Figure B1**): Cores were prepared using the same printing and sterilization protocols as Method 1. After posts were UV sterilized in the biosafety cabinet for 20 min, posts were soaked in 1% bovine serum albumin (BSA) for 40 min to prevent the collagen from sticking to the post, enabling easier removal of the hydrogel ring, and left to air dry before use. 1 mL syringes (COVIDIENTM) were trimmed at the 0.8 mL mark and the core was replaced with the 3D-printed posts.

Hydrogel ring fabrication using Method 2 (**Figure B1**): For Method 2 the trimmed syringes and BSA soaked 3D printed cores were combined to form the mold. The cell-laden collagen solution was then carefully pipetted into the mold to avoid bubbles; depending on the tubing size, roughly 20–30 µL of cell-laden collagen solution was used per ring. After addition of hydrogel mixture, the molds were placed in a BioAssay Dish that was lined with Kimwipes soaked in 1X PBS. The BioAssay Dish containing molds was then transferred to an incubator to allow the collagen to gel at 37°C. For the first 10 min, the BioAssay Dish was carefully flipped 180° every 2 min to ensure distribution of cells throughout the collagen. After 1.5 h of incubation, the BioAssay Dish containing hydrogel ring molds was removed from the incubator and brought into a biosafety cabinet. The Teflon tubing was lowered and the hydrogel rings were transferred to individual wells in a 96-well plate. 100 µL of cell culture media was added to each well, and the surrounding wells were filled with 100 µL of 1X PBS to prevent evaporation of media. The hydrogel rings were then incubated at 37°C with 5% CO2 until experimentation, with growth media replaced every 24 h.

Measurement of hydrogel rings (**Figure B1**): Images were obtained using an Amscope MU1403B High Speed Microscope Camera mounted on an Amscope SM-3TZ-80S stereoscope (Amscope, Irvine, CA) and processed in FIJI (ImageJ). All images were thresholded between 40 and 255 prior to obtaining measurements. The outer diameter was measured manually by drawing a line across the image at 0, 45, 90, and 135 degrees and averaging those values; the same procedure was used for the inner diameter.

Dilation experiments (**Figure B3**): After 5 days in culture, cell-laden hydrogel rings were used for vasodilation experiments. Two hydrogel rings were transferred to individual wells of a new 96-well plate, and submerged in 60 µL Tyrode's Solution (T2397, Sigma-Aldrich). After 5 min of equilibration the solution was removed and replaced with fresh Tyrode's Solution. 6 µL of either additional Tyrode's Solution (control) or fasudil (vasodilator) (HA-1077 dihydrochloride, Sigma-Aldrich) was then added. The well plate was then placed under a stereoscope and recorded for 20 min after which hydrogel rings were transferred to a new well plate containing cell media for

staining and imaging. This process was repeated with additional hydrogel rings until the desired number of replicates had been tested.

Imaging of vasodilation experiments and processing: Top-view images of hydrogel rings were recorded using an Amscope MU1403B High Speed Microscope Camera mounted on an Amscope SM3TZ-80S stereoscope. Stills were obtained from video recordings for every 60 sec (i.e., 21 stills were obtained for a 20 min recording). These images were then processed using FIJI (ImageJ) to calculate the total hydrogel area.

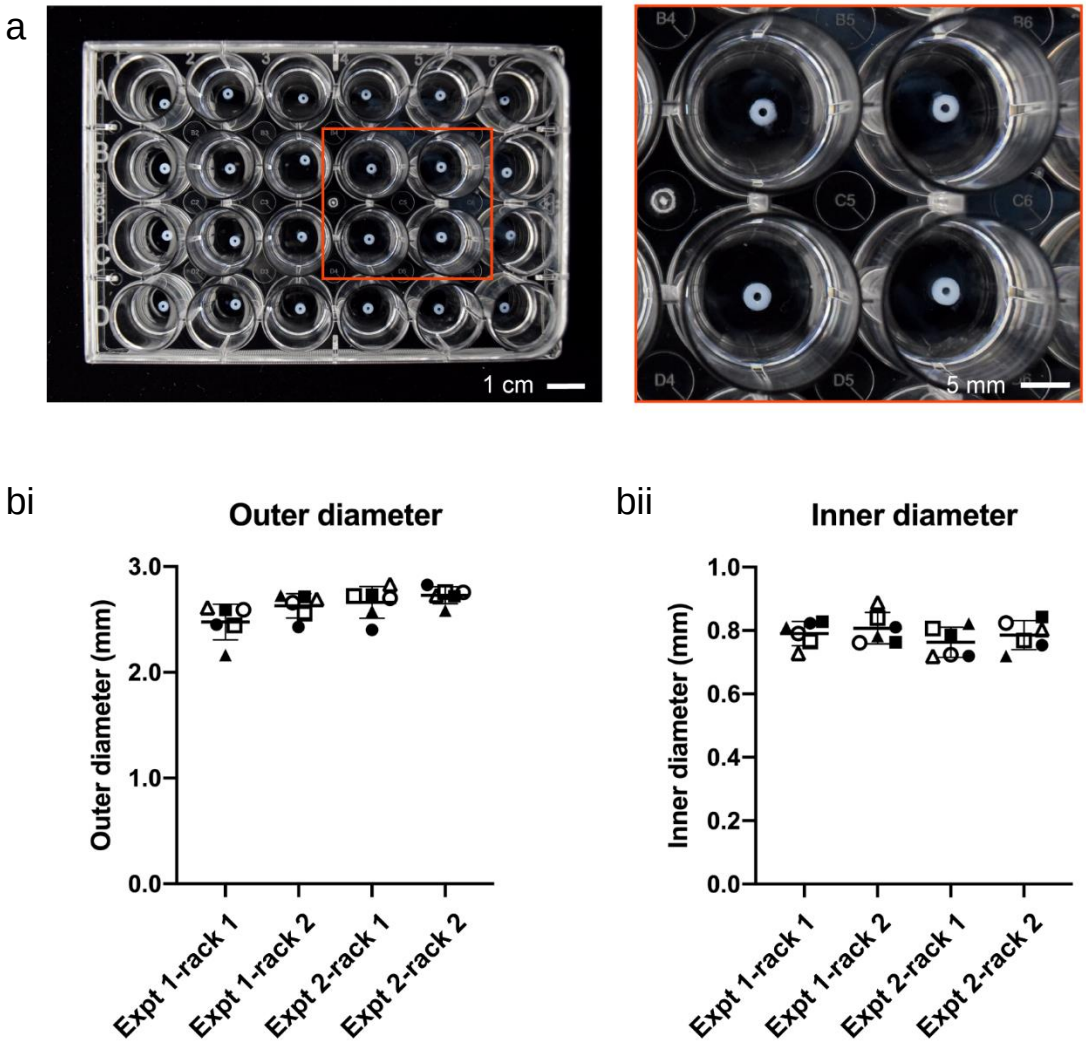

Figure B1. Reproducibility of collagen I rings designed with an outer diameter of 3.0 mm and inner diameter of 1.0 mm. (a) Collagen rings of equal size in a 24-well plate. (bi) The average outer diameter from each device was 2.48±0.17 mm, 2.63±0.12 mm, 2.66±0.15 mm, 2.73±0.08 mm and (bii) their respective inner diameters were 0.79±0.04 mm, 0.81±0.05 mm, 0.76±0.05 mm, and 0.79±0.05 mm. Each symbol pairs the OD measurements to ID measurements across bi and bii. Results are plotted from two independent experiments, each with two racks (one rack is an array of 6 lumens). Error bars are mean ± SD.

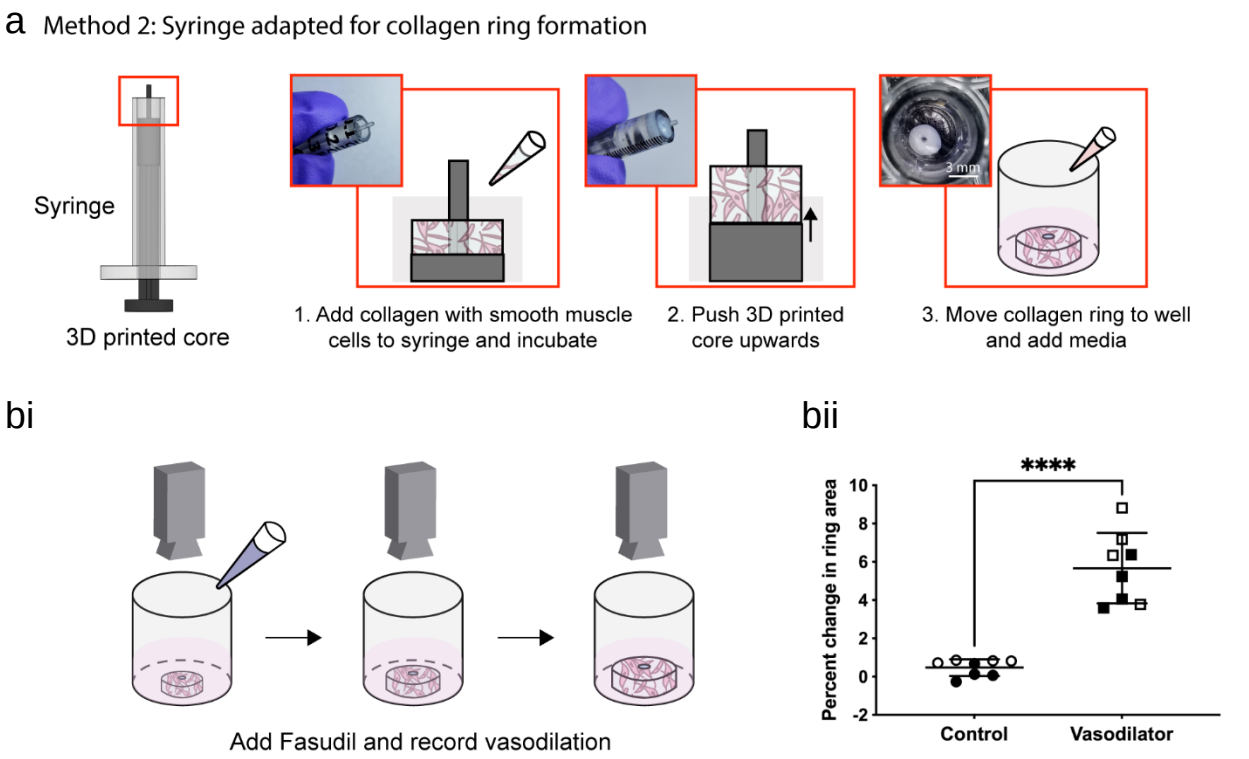

Figure B2. Percent change in ring area when human umbilical artery smooth muscle cells seeded in hydrogel rings were treated with a vasodilator (fasudil). (a) Method 2 workflow using a commercially available syringe with a 3D printed insertable core that has been adapted to make cell laden collagen rings. (bi) The hydrogel rings were recorded for 20 min after addition of fasudil, and their percent change in area was calculated using ImageJ. (bii) Percent change in ring area data for hydrogel rings treated with buffer (control) or vasodilator (fasudil). Data points are from 8 rings across 2 independent experiments, where the 2 experiments are denoted by filled or hollow circles/squares; error bars are mean ± SD. A two-sample unpaired t-test (two-tailed) was used. $^{****}p < 0.0001$.

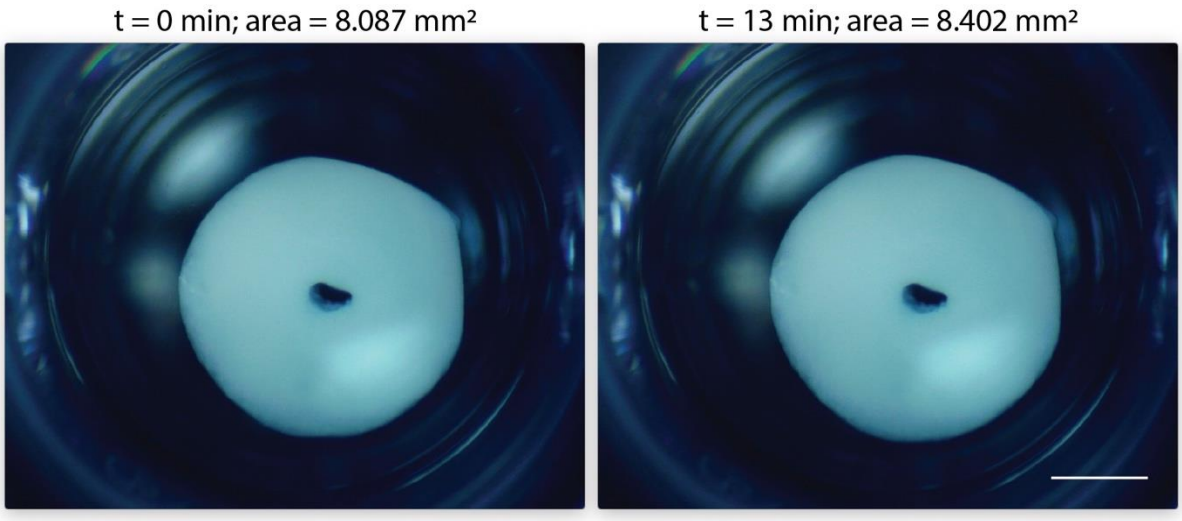

Figure B3. Images of smooth muscle cell laden collagen I rings during experimentation with a vasodilator (fasudil). Images are at t = 0, addition of fasudil, and at t = 13 min. Change in ring area is not visible by eye; it is quantifiable using image processing software (see methods section). Scale bar is 1 mm.

Table B1. Comparison of general features of excised animal tissue models, standard closed microfluidic lumen models, and our freestanding method

	Excised Animal Tissue[3,4]	Standard Closed Channel Microfluidic Lumen Models[5,6]	Our Freestanding Method
Freestanding	Yes	No	Yes
Requires Animal Tissue	Yes	No	No
Tissue Layers Are Possible	Yes	Yes	Yes
Human Cells Can Be Incorporated	No	Yes	Yes

References

1. Q. Wei, S. Wang, F. Han, H. Wang, W. Zhang, Q. Yu, C. Liu, L. Ding, J. Wang, L. Yu, C. Zhu, and B. Li, Cellular modulation by the mechanical cues from biomaterials for tissue engineering, *Biomater. Transl.*, 2021, **2**, 323.
2. S. Il Murtada, Y. Kawamura, G. Li, M. A. Schwartz, G. Tellides and J. D. Humphrey, Developmental origins of mechanical homeostasis in the aorta, *Dev. Dyn.*, 2021, **250**, 629–639.
3. N. Robbins, A. Thompson, A. Mann and A. L. Blomkalns, Isolation and excision of murine aorta; a versatile technique in the study of cardiovascular disease, *J. Vis. Exp.*, 2014, e52172.
4. F. Marceau, D. deBlois, E. Petitclerc, L. Levesque, G. Drapeau, R. Audet, D. Godin, J. F. Larrivée, S. Houle, T. Sabourin, J. P. Fortin, G. Morissette, L. Gera, M. T. Bawolak, G. A. Koumbadinga and J. Bouthillier, Vascular smooth muscle contractility assays for inflammatory and immunological mediators, *Int. Immunopharmacol.*, 2010, **10**, 1344–1353.
5. Y. Zheng, J. Chen, M. Craven, N. W. Choi, S. Totorica, A. Diaz-Santana, P. Kermani, B. Hempstead, C. Fischbach-Teschl, J. A. López and A. D. Stroock, In vitro microvessels for the study of angiogenesis and thrombosis, *Proc. Natl. Acad. Sci. U. S. A.*, 2012, **109**, 9342–9347.
6. J. A. Jiménez-Torres, S. L. Peery, K. E. Sung and D. J. Beebe, LumeNEXT: A Practical Method to Pattern Luminal Structures in ECM Gels, *Adv. Healthc. Mater.*, 2016, **5**, 198–204.

b. 4.2. Injection molded open microfluidic well plate inserts for user-friendly coculture and microscopy

Reproduced in part from J.H. Day, T.M. Nicholson*, X. Su, T.L. van Neel, I. Clinton, A. Kothandapani, J. Lee, M.H. Greenberg, J.K. Amory, T.J. Walsh, C.H. Muller, O.E. Franco, C.R. Jefcoate, S.E. Crawford, J.S. Jorgensen, A.B. Theberge, "Injection molded open microfluidic well plate inserts for user-friendly coculture and microscopy." Lab on a Chip,* ***2020****, 20, 107.*
** Equal contribution*

Design considerations for injection molding open microfluidic devices

Our open microfluidic cell culture devices were designed for manufacture with injection molding. Injection molding is a fabrication method in which the geometry of a plastic device is cut as the negative space inside a metal mold. Molten thermoplastic is injected into the negative space of the mold through an opening called a gate. Once the plastic cools, the mold is separated, the plastic device is ejected, and the mold is reused to make more devices.

Rapid injection molding companies impose relatively stringent design constraints on parts in order to keep the mold simple and the price low. The most important of these constraints is that every face of the device must be visible from either the top or the bottom of the part. This necessitates every vertical face of a device to be drafted (i.e., angled slightly). When this criterion is met, the device can be fabricated with a two-sided mold. Importantly, because our devices use open microfluidics rather than closed channels, the entire device is fabricated as a single injection molded part without subsequent bonding steps. **Figure B5** shows the devices presented here. After the device is molded, the molten plastic is allowed to cool. The cooling process can cause shrinking in thicker areas of the device due to differential cooling time between thick and thin areas in the device. Shrinking manifests as sunken areas in a device, where surfaces of the device that were designed to be flat come out as concave and sunken into the device. Coring out thick areas of the device creates more uniformity in the thickness of the device, mitigating shrinkage anomalies. Once the device is cooled and the two sides of the mold are separated, the device must be ejected from the mold. This is accomplished with ejector pins, which push the device out of the mold after the molding process is complete. The placement of ejector pins in the mold is

important so that an even force is applied across the entire device. Devices that are fabricated with injection molding must be designed with space for these ejector pins to push against, which manifest as small circles in the final device. This informed our decision to design the ejector pins to be located on the top ("A" side) of the device so that they would not interfere with the open microfluidic hydrogel patterning that occurs on the bottom ("B" side) (**Figure B5**).

Device removal workflow for high resolution microscopy:

High resolution imaging is an important readout for biomedical researchers, as the intracellular location of the substance of interest (e.g., protein, mRNA) has important implications for function. Immunocytochemistry is a common molecular technique used to localize protein antigens of interest in cells by binding of a specific antibody. In situ hybridization is an analogous technique to localize nucleic acids in cells to discover both temporal and spatial information about gene expression. Single molecule fluorescence in situ hybridization (smFISH) detects a specific mRNA transcript with multiple short oligonucleotide probes and offers improved resolution and quantitation compared to traditional in situ hybridization and immunocytochemistry.[1] It is a powerful tool for understanding the spatial and temporal patterns of gene expression at the level of the individual cell. For high resolution imaging, such as smFISH, cells are typically cultured on glass coverslips, rather than plastic cultureware since plastic cultureware limits high resolution imaging due to thickness, autofluorescence, and defects in the plastic surface. A common workflow for immunocytochemistry or smFISH sample preparation involves fixing and processing cells on a glass coverslip and then mounting the coverslip on a glass slide such that the sample is sandwiched between the coverslip and the slide. Often, samples are mounted using "mounting media", and the coverslip is sealed to the glass slide, enabling the samples to be stored long term. Since this method is commonplace in many biology labs, many products have been developed around this workflow including holders that enable staining and chemical processing of multiple coverslips at a time, microscope stages designed to hold a standard glass slide, and boxes designed to hold glass slides that biology labs routinely use to archive samples for many years.

In our prior work we showed that hydrogel patterning works on glass surfaces, such as well plates with integrated glassbottoms;[2] here we developed procedures to use our devices on top of a glass coverslip within a well, remove the device from the coverslip after the culture period, and mount the coverslip on to a glass slide. This is also important because some specialty microscopes used for smFISH require the use of proprietary coverslips with specific thickness tolerances.

We designed devices that are compatible with two standard coverslip sizes: round coverslips (20 mm in diameter) that fit in a 12-well plate and square coverslips (22 × 22 mm) that fit in a 6-well plate. The Monorail1 and Monorail2 devices fit in a 12-well plate and are compatible with 20 mm diameter coverslips. In all designs, the placement of the hydrogel loading port was an important consideration; in contrast to our prior designs,[2] where the loading port was at the perimeter of the well, here we moved the loading port away from the edge of the well to prevent hydrogel from creeping between the coverslip and the bottom of the well plate. **Figure B6** shows a schematic workflow of how samples are prepared for high resolution imaging, as well as images of cells cultured in the microscale devices. These images show no visual distortion of immunostained cells by the hydrogel residue, supporting the compatibility of the Monorail devices with high resolution imaging.

Additionally, single molecule fluorescent in situ hybridization (smFISH) performed on cultured MA-10 cells was used to detect transcription of the genes encoding steroidogenic acute regulatory protein (Star) and cholesterol side-chain cleavage enzyme (Cyp11a1) followed by cAMP stimulation for 3 h. Single mRNA transcripts are visualized as discreet spots (red or green) in the cytoplasm and are used to accurately quantify the number of transcripts for each gene. The power of this method is that it can be used to compare transcriptional responses from external signals, thereby enabling quantitative mechanistic studies.[1,3] **Figure B7** compares smFISH images of MA-10 cells cultured on coverslips in the presence and absence of the Monorail1 device.

Additional Materials and Methods

Cell culture for imaging and viability (**Figures 4.2.2, 4.2.3**, and **B6**): Human lung microvascular endothelial cells (HLMVEC) (Cell Applications, 540–05a) were cultured in EGM™-2 endothelial cell growth media (Lonza, CC3162). MA-10 cells (ATCC, CRL-3050)[4] were cultured in DMEM/F12 (Gibco, 11330–032) media containing 5% horse serum (Gibco,16050), 2.5% fetal bovine serum (FBS) (HyClone, SH3039603), and 1.5 g/L sodium bicarbonate. BHPrS1 cells (benign human prostate stromal cells, from Simon Hayward's lab at NorthShore HealthSystems) were cultured in RPMI-1640 medium (Gibco, 22400–089) with 5% FBS (HyClone, SH3039603).[5] In addition, both MA-10 and BHPrS1 cell culture media were also supplied with penicillin (100 units/ml)/streptomycin (100 µg/ml) (Gibco, 15140122). Cells were cultured at 37 °C under 5% CO2. Cells were trypsinized (Gibco, 12604021), resuspended at 3.8×10^5 cells/mL and seeded into devices at cell seeding density of 250–300 cells/mm^2. For 6-well plate experiments (**Figure B6 a,e**), 200 µL of sterile water was added to the edges of 6-wells containing devices; care was taken to prevent this added water from reaching the device in the center of the well. 6-well plates were placed in a bioassay dish (245 mm x 245 mm) containing about 50 mL of sterile water and incubated. For 12-well plate experiments using the Monorail1 device, 1 mL of sterile water was added in the interwell spaces (**Figure 4.2.2 a**), and 2 mL of sterile water was added to any wells that did not contain a device. 11 µL of media was loaded into each culture chamber in the device, followed by an addition of 11 µL of cell suspension. Cell culture media was changed partially (approximately half of the media was exchanged for fresh media in each chamber) each day, and external water for evaporation control was replenished when a reduction in volume was visible. For 12-well plate experiments using the Monorail2 device, 8 and 20 µL of cell suspension were loaded into the center and outer chambers of the device, respectively, followed by 500 µL of media to the media reservoir (**Figure 4.2.3 aii**). Cells were fixed with 4% paraformaldehyde (Fisher Scientific, AA433689M) prior to staining.

Proliferation and viability assays: For the proliferation assay shown in **Figure B6**, 5-Ethynyl-2′-deoxyuridine (EdU, Invitrogen) was prepared according to the manufacturer's specifications and diluted in cell culture media to 10 μM. EdU was added to cell culture and incubated for 6 h; then the cells were fixed with 4% paraformaldehyde. Cells treated with EdU were subjected to Click-iT reaction cocktail (Invitrogen), which was prepared according to the manufacturer's specifications and incubated with cells for 30 min. For assessment of cell viability shown in **Figures 4.2.2** and **4.2.3**, live/dead staining was performed by incubation of cells with 2 nM ethidium bromide (dead) and 10 μM Calcein AM (LIVE/DEAD® Viability/Cytotoxicity Kit for mammalian cells, Invitrogen, L3224) for 30 min at 37 °C.

Immunocytochemistry: For fluorescence images shown in **Figure B6**, cells were fixed, then devices were carefully removed from coverslips using forceps. Fixed MA-10 cells (**Figure B6 b**), HLMVECs (**Figure B6 c**), and BHPrS1 cells (**Figure B6 d**) on coverslips were permeabilized with 0.5% Triton X-100 for 30 min and blocked with 3% BSA, then incubated with 2 μg/mL anti-α-tubulin antibody raised in rat (Invitrogen, MA180017) overnight at 4 ºC. After washing 3–5 times with PBS containing 0.1% Triton X-100, goat anti-rat secondary antibody conjugated with Alexa Fluor 488 (Jackson ImmunoResearch, 112545167, 1.5 mg/mL) for MA-10 and BHPrS1 cells, or with Alexa Fluor 647 (Jackson ImmunoResearch, 112605167, 1.25 mg/mL) for HLMVECs, was added at a 1:200 dilution and incubated with cells for 1 h followed by a 20 min incubation with 5 μg/mL Hoechst 33342 (Invitrogen, H1399). Control stainings—using secondary antibodies only—were carried out to confirm negligible nonspecific binding of fluorescent tags. HLMVECs were stained for actin with phalloidin conjugated with Alexa Fluor 488 (ThermoFisher Scientific, A12379). Cells were washed as above. Coverslips were then placed on glass slides with VectaShield antifade mounting media (Vector Laboratories, H1000) and sealed with nail polish (Electron Microscopy Sciences, 72180). Fluorescence images were acquired using an Axiovert 200 Zeiss microscope equipped with Axiocam 503 mono camera. Phase contrast images were taken with Zeiss Primovert inverted microscope with a MU1403B camera (AmScope).

Single molecule fluorescence in situ hybridization (smFISH): The MA-10 cells shown in **Figure B6 e** were treated with 1 mM Br-cAMP (Axxora, BLGB007) for 3 h, washed in PBS and fixed with 4% formaldehyde for 15 min followed by permeabilization with 70% ethanol for 1 h. After washing the cells with wash buffer for 5 min (2x SSC and 10% formamide), 50 µL of hybridization solution containing the RNA probes was added. The RNA probe sets for Star and Cyp11a1 were generated with the Stellaris probe designer and the probes were dissolved in TE buffer, pH 8.0 (LGC Biosearch Technologies). A clean coverslip was placed over the sample to prevent drying of the hybridization solution during the incubation. The hybridization solution contained 10% dextran sulfate (Sigma, D8906), 10% deionized formamide (Ambion, AM9342) and 2x SSC (Ambion, AM9765). Samples were incubated in a dark humidified chamber at 37 °C overnight. After a 30 min wash in wash buffer, samples were incubated for 30 min in DAPI (wash buffer with 5 ng/ml DAPI) to counterstain the nuclei. After a brief incubation with 2x SSC for 5 min, antifade GLOX buffer (2x SSC, 10% glucose and 1M Tris, pH 8.0) was added without enzymes for equilibration followed by incubation with added glucose oxidase (Sigma, G2133) and catalase (Sigma, C3515) for 5 min. The samples were mounted with a drop of Prolong Gold antifade reagent (Invitrogen, P36930). Super-resolution imaging was performed with a Nikon-Structured Illumination Microscopy (N-SIM) system equipped with a SR Apo TIRF 100X objective and an iXon3 camera (Andor Technology). The images were acquired as 3D-SIM Z-stacks and analyzed using NIS-Elements software (Nikon).

Oil-Red-O stain: PC-3 and 3T3-L1 cells were grown in the Monorail1 device on glass coverslips coated with poly-L-lysine (Sigma, St. Louis, MO, USA) and cultured and treated as described above. Cells were then washed three times with PBS, fixed in 10% formalin (30 min at room temperature), and stained with Oil-Red-O (Oil-Red-O Stain, propylene glycol; Newcomer Supply, Middleton, WI, USA) to visualize neutral lipids. Cells were also counterstained with hematoxylin (Newcomer Supply, Part # 1180G) for 10 min and lithium carbonate (Sigma, L4283–100G) for ~5 sec to add contrast and highlight the nucleus. Coverslips were mounted on glass slides and

sealed with Permaslip Mounting Medium (Alban Scientific Inc.). Pictures were taken of representative fields for each treatment using a 100X objective to highlight intracellular lipid droplets.

Lipid droplet area: In slides stained with Oil-Red-O, positive intracytoplasmic lipid droplets were evaluated in 15 high power fields/experimental group. Area was calculated using Image J software (NIH, Bethesda, MD).

Statistical analysis: To determine differences between experimental groups, a Student's t-test was used, and findings were considered significant when $p < 0.05$. Graphs were made using GraphPad Prism, version 7.03.

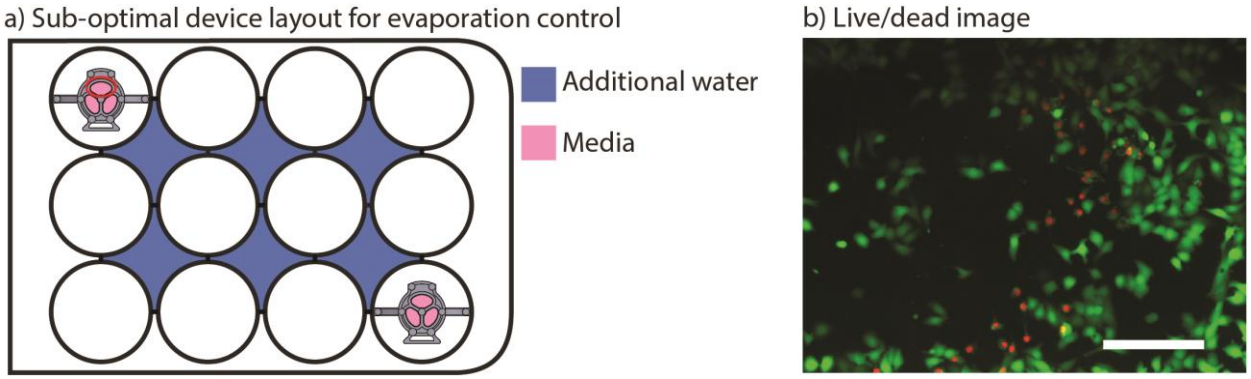

Figure B4. Cell viability in sub-optimal conditions for evaporation control. a) Well plate layout that leads to evaporation in cell culture chambers of monorail devices. b) Representative image of cell viability in top culture chamber of upper left monorail device from well plate layout (scale bar = 200 µm).

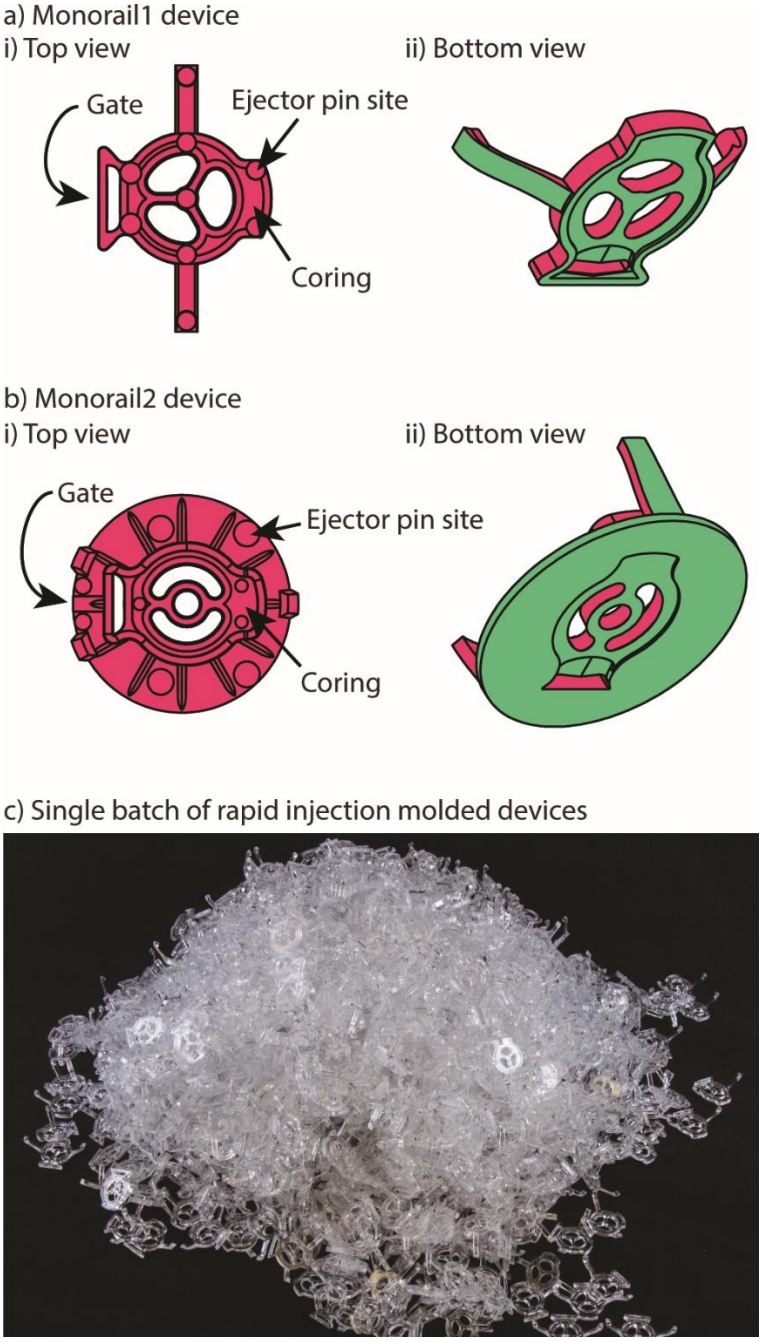

Figure B5. Monorail devices can be fabricated via rapid injection molding. a) Monorail1 device and b) Monorail2 device schematics showing location of coring, ejector pins (all small round circles), and gates from top (i) and bottom (ii) views. c) Photo of Monorail1 devices fabricated with rapid injection molding.

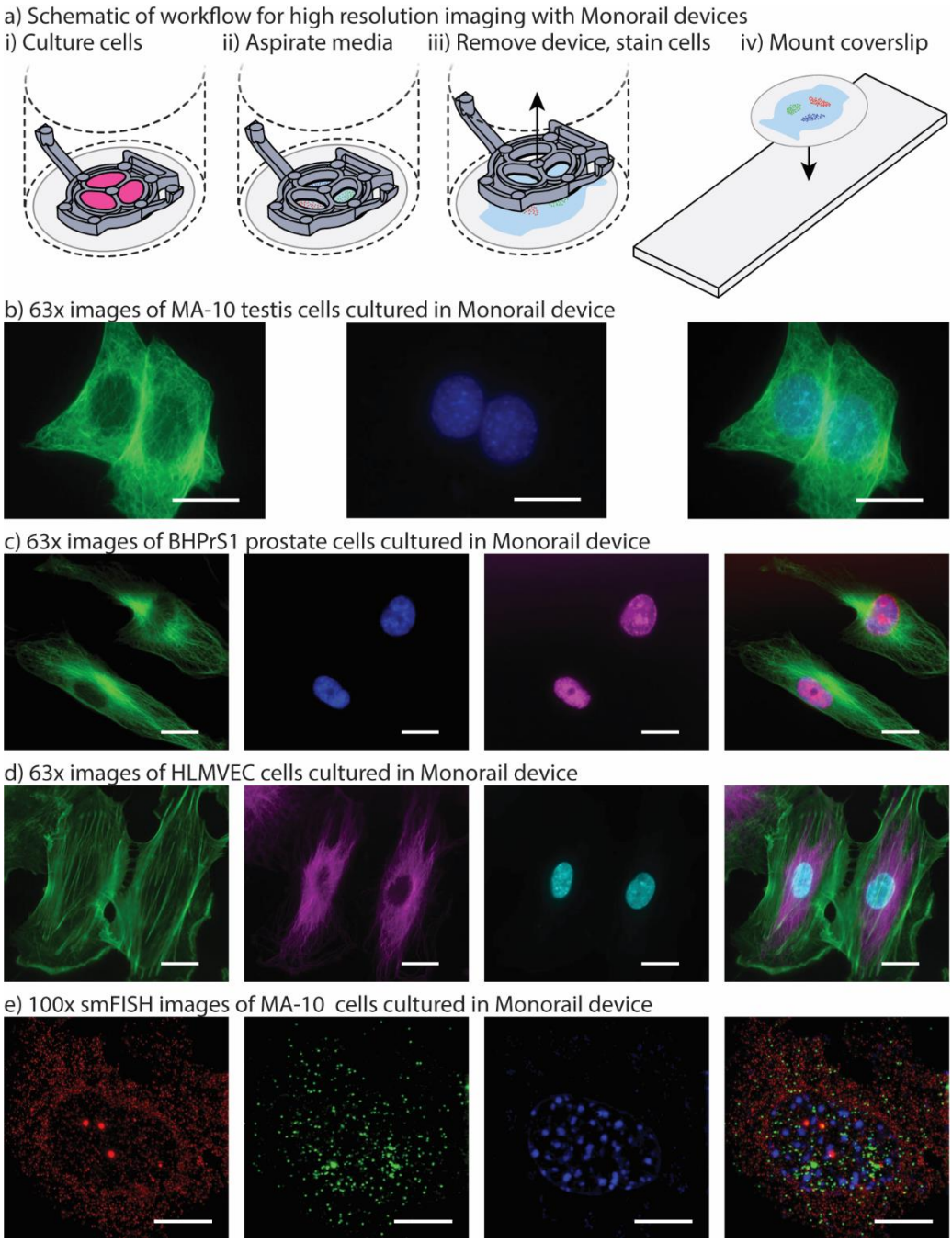

Figure B6. Monorail devices allow high resolution microscopy for coculture experiments. a) Schematic workflow for high resolution imaging with monorail devices. i) A glass coverslip is placed in the well of a well plate, a device is placed over the top, and cells are cultured. ii) At the conclusion of the cell culture experiment, the media is aspirated. iii) After fixing cells, the device is lifted gently from the coverslip and removed, with some hydrogel residue remaining on the coverslip; immunostaining is performed iv) The coverslip is removed from the well, inverted, and placed on a glass slide. Imaging is then performed directly through the glass coverslip by inverting the slide-coverslip assembly. This sample preparation was carried out for all high-resolution images. b) MA-10 testis cells were cultured in the milled Monorail2 device in a 6-well plate and

immunostaining was performed todetect α-tubulin (green) and nuclei (Hoechst, blue). Scale bars: 20 μm. c) BHPrS1 cells were cultured in the Monorail1 device in a 12-well plate and immunostaining was performed to detect α-tubulin (green), nuclei (Hoechst, blue) and proliferating nuclei (EdU, pink). Scale bars: 20 μm. d) HLMVECs were cultured in the Monorail2 device in a 12-well plate and immunostaining was performed to detect actin (green), α-tubulin (magenta), and nuclei (Hoechst, blue). Scale bars: 20 μm. e) N-SIM Z-stack (total 26 planes) images taken of smFISH probes designed to recognize Star (red) and Cyp11a1 (green) mRNA within MA-10 cells cultured in milled Monorail2 device. Nuclei are counterstained with DAPI (blue). Scale bars: 10μm.

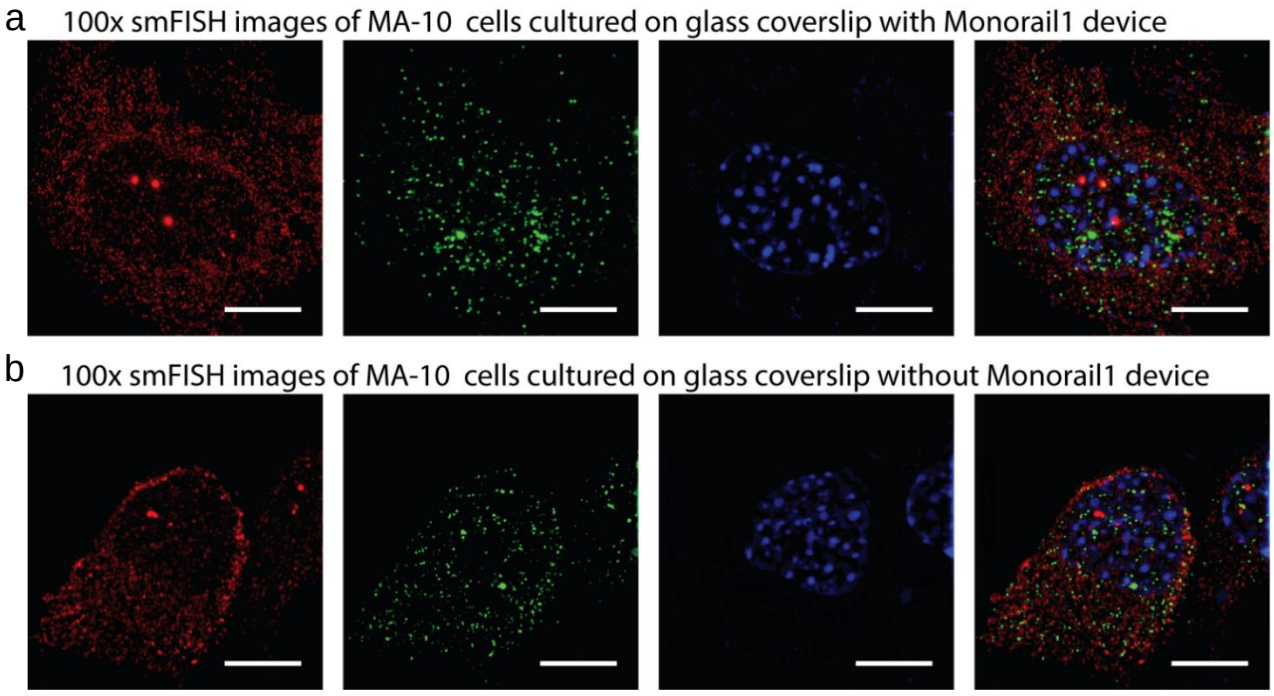

Figure B7. smFISH imaging comparison of MA-10 cells. Comparison between a) a 26-slice Z-stack image of an MA-10 cell cultured in Monorail (reproduced from Figure B6 e) and b) a 24-slice Z-stack image of an MA-10 cell culture in 12 well plate macro-culture shows the same subcellular features and resolution. Images show smFISH probes designed to recognize spliced Star (red) and Cyp11a1 (green), as well as DAPI (blue). Scale bars = 10 µm.

References

1. J. Lee, Y. H. Foong, I. Musaitif, T. Tong and C. Jefcoate, Analysis of specific RNA in cultured cells through quantitative integration of q-PCR and N-SIM single cell FISH images: Application to hormonal stimulation of StAR transcription, *Mol. Cell. Endocrinol.*, 2016, **429**, 93–105.
2. S. B. Berry, T. Zhang, J. H. Day, X. Su, I. Z. Wilson, E. Berthier and A. B. Theberge, Upgrading well plates using open microfluidic patterning, *Lab Chip*, 2017, **17**, 4253–4264.
3. J. Lee, T. Tong, H. Takemori and C. Jefcoate, Stimulation of StAR expression by cAMP is controlled by inhibition of highly inducible SIK1 via CRTC2, a co-activator of CREB, *Mol. Cell. Endocrinol.*, 2015, **408**, 80–89.
4. M. Ascoli, Characterization of several clonal lines of cultured Leydig tumor cells: gonadotropin receptors and steroidogenic responses, *Endocrinology*, 1981, **108**, 88–95.
5. O. E. Franco, M. Jiang, D. W. Strand, J. Peacock, S. Fernandez, R. S. Jackson, M. P. Revelo, N. A. Bhowmick and S. W. Hayward, Altered TGF-β signaling in a subpopulation of human stromal cells promotes prostatic carcinogenesis, *Cancer Res.*, 2011, **71**, 1272–1281.

C. Supplementary Information for Chapter 5

Reproduced in part from U.N. Lee, T.L. van Neel,* F.Y. Lim, JW. Khor, J. He, R.S. Vaddi, A.Q.W. Ong, A. Tang, J. Berthier, J.S. Meschke, I.V. Novosselov,§ A.B. Theberge,§ E. Berthier,§ "Miniaturizing wet scrubbers for aerosolized droplet capture." Analytical Chemistry, **2021**, 93, 11433–11441.*
** Equal contribution*
§ Co-corresponding authors

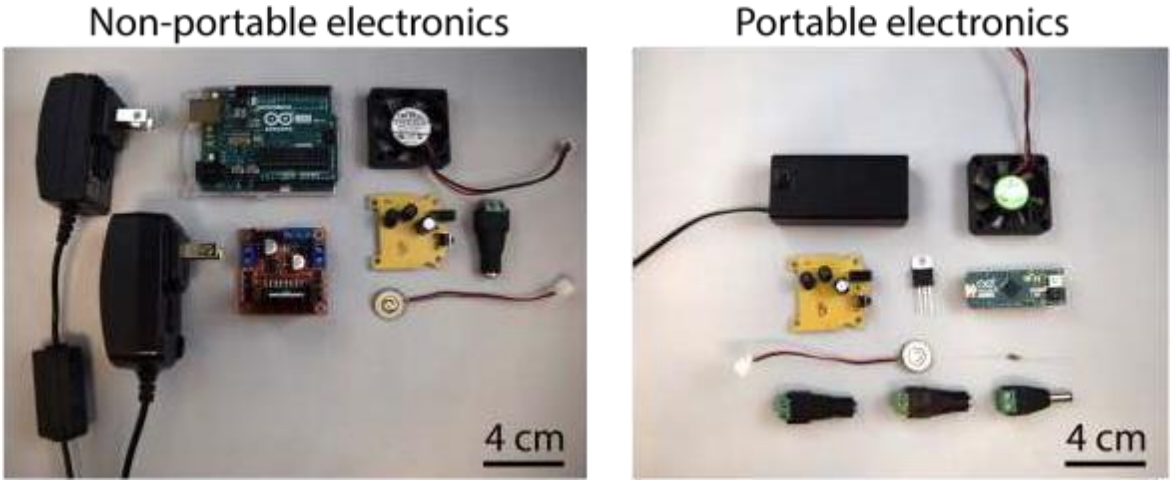

Figure C1. Photo of non-portable electronic components used for droplet retention measurements and videos (**Figures 5.3-5.6**) and portable electronics used for particle chamber experiments (**Figure 5.7** and **5.8**). Wires not pictured.

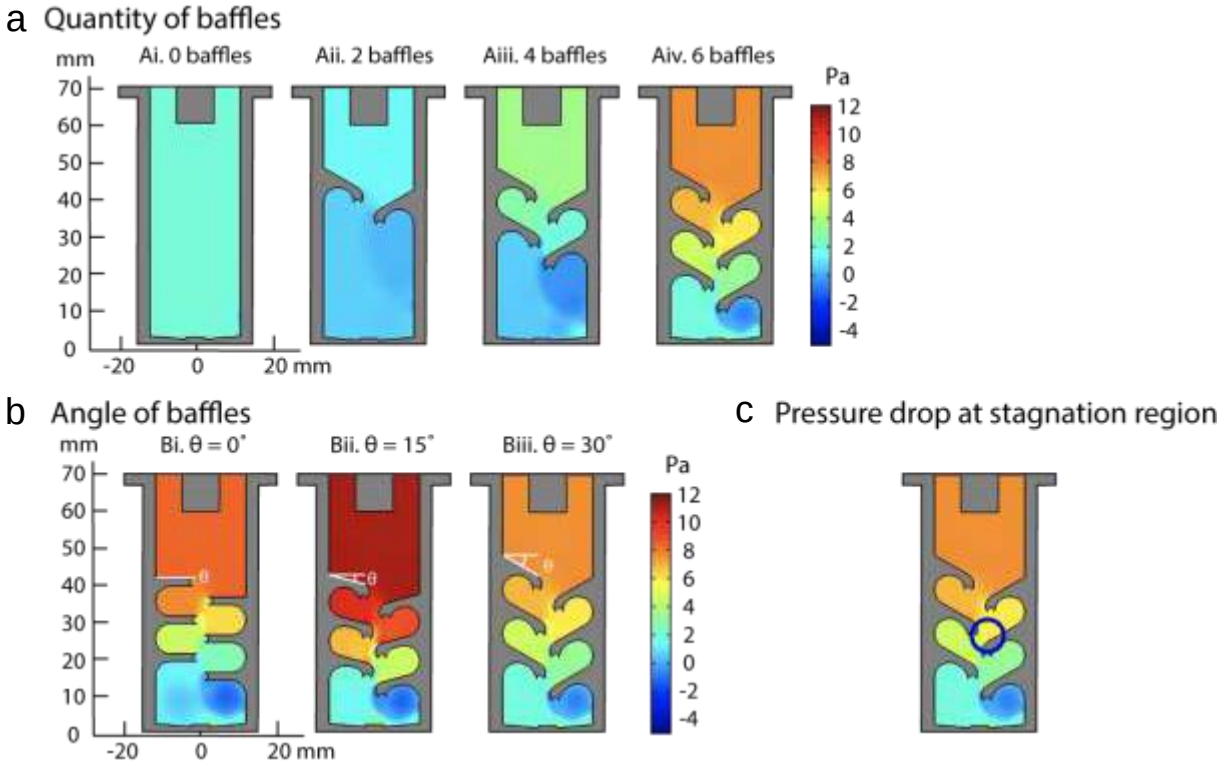

Figure C2. Pressure maps from simulations of device iterations pictured in **Figure 5.5**. (a) Pressure above the top baffles increases with each additional set of baffles. (b) When the angle of the baffle is changed from 0° to 15°, pressure increases before decreasing again at a 30° baffle angle. Reduced pressure is preferable to allow aerosol entrance into the device. (c) The pressure drop generated by impinging jets at stagnation regions increases droplet coalescence on baffle surfaces. Scale bar indicates the pressure above or below atmospheric pressure (i.e., 0 Pa = atmospheric pressure).

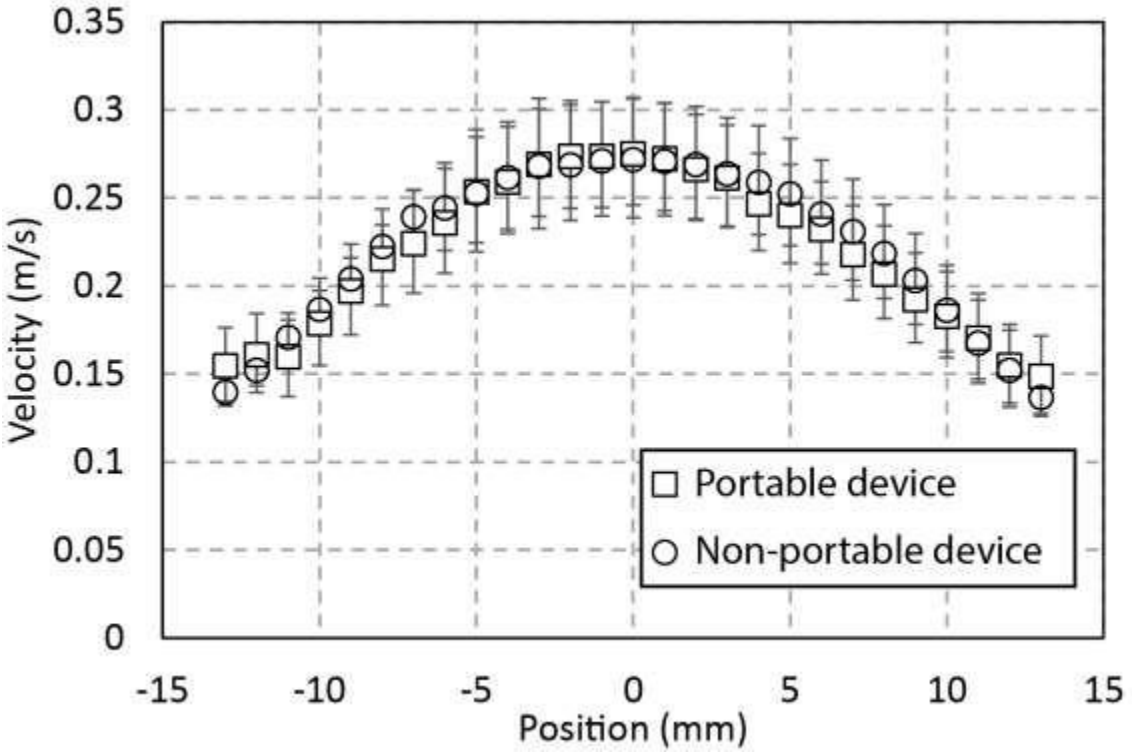

Figure C3. Plot of air flow velocity from the outlet of the device comparing the airflow rate between our non-portable device (**Figures 5.3-5.6**) and our portable device (**Figure 5.7** and **5.8**). The two devices used two different fans to accommodate voltage requirements for each electronics set up, but produced the same velocity and volumetric flow rate.

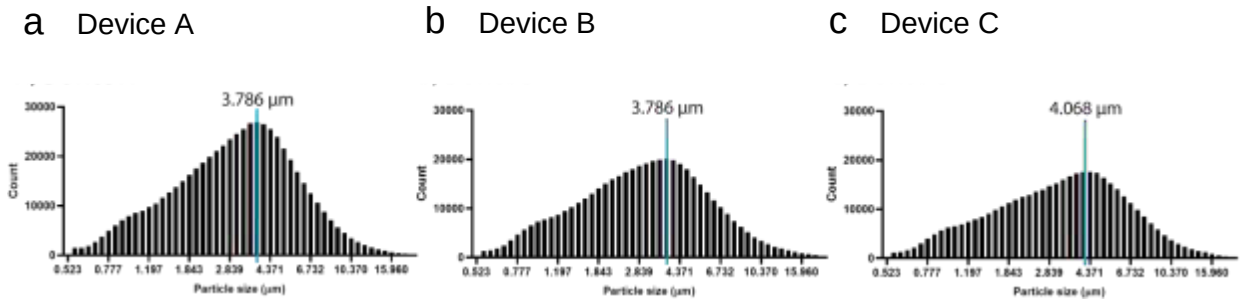

Figure C4. Droplet size distributions for each device as measured using an aerodynamic particle sizer. Average droplet size ± SD from n=3 devices is 3.88 ± 0.16 µm.

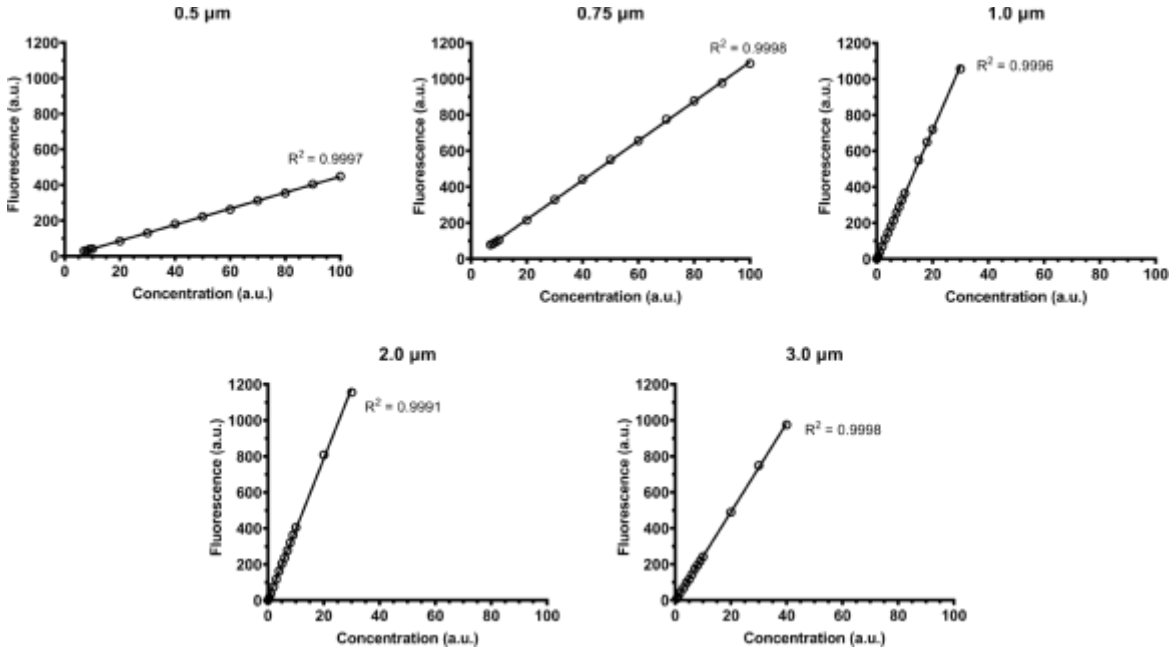

Figure C5. Calibration curves for each particle size used in **Figure 5.7**. Calibration curves were used to validate fluorescent signals of samples collected from devices and reference filters were in the linear range. Points represent mean ± SD of n=3. In all cases the standard deviation was smaller than the point plotted.

Table C1. Particle concentration used in the test chamber for each particle size. Particle concentrations used at each size varied to ensure adequate particles were aerosolized and available for capture in the test chamber as in prior work (He, J.; Novosselov, I. V., Design and evaluation of an aerodynamic focusing micro-well aerosol collector. *Aerosol Science and Technology* **2017,** *51* (9), 1016-1026). During each 25 min chamber run, 2-3 mL of solution was nebulized. Concentration reported here was measured with the aerodynamic particle sizer (APS) attached to the chamber exhaust.

Particle size (μm)	**Concentration (particle/cm^3)**
0.50	4500-5500
0.75	10000-13000
1.0	4200-5800
2.0	1200-1500
3.0	1200-1500

Table C2. Diameter of aerosolized biological particles of interest. To avoid unnecessary exposure to known biological pathogens in this initial characterization publication, we chose to use monodispersed fluorescent polystyrene latex spheres as a proxy. Sizes used were based on relevant bioaerosols that are known to adversely affect human health.

Diameter of inert particle proxy (μm)	**Diameter of relevant bioaerosol (μm)**	**Reference**	**Examples of human health impact**
0.5	SARS-CoV-2 aerosols 0.25 - 0.5	Liu, Y. et al., *Nature* **2020**, *582* (7813), 557–560.	COVID-19, respiratory complications
0.75	*Staphylococcus aureus* 0.5 - 1.0	Madsen, A. M. et al., *Annals of Work Exposures and Health* **2018**, *62* (8), 966–977.	Sepsis, pneumonia, infections
1.0	viral particle + respiratory droplet ≤ 1.0	Fennelly, K. P. *The Lancet Respiratory Medicine* **2020**, *8* (9), 914–924.	Flu, common cold
2.0	*Aspergillus fumigatus* 2 - 3.5	Kwon-Chung, K. J. et al., *PLoS Pathog* **2013**, *9* (12).	Pulmonary aspergillosis, allergic asthma
3.0	*Mycobacterium tuberculosis* 2 - 4	Kim, K.-H. et al., *Journal of Environmental Sciences* **2018**, *67*, 23–35.	Tuberculosis

Table C3. Relative standard deviation (RSD) of reference filters and devices across the three experimental test chamber runs. While variability is generally higher in our devices, it is important to note variability also exists within the reference filters used, likely due to the manual control of the flow rate and particle nebulization. The averages shown here were taken from n=3 devices or n=3 reference filters within a run of the test chamber.

A. 0.5 µm particles

	Device Avg (a.u.)	Device RSD (%)	Reference Avg (a.u.)	Reference RSD (%)
run 1	104.2	**23.9**	495.5	**8.8**
run 2	102.5	**9.2**	654.4	**14.8**
run 3	83.9	**13.9**	662.3	**23.4**

B. 0.75 µm particles

	Device Avg (a.u.)	Device RSD (%)	Reference Avg (a.u.)	Reference RSD (%)
run 1	164.7	**25.8**	1954.2	**5.4**
run 2	132.7	**17.8**	1138.3	**19.0**
run 3	107.0	**19.8**	1335.7	**16.8**

C. 1.0 µm particles

	Device Avg (a.u.)	Device RSD (%)	Reference Avg (a.u.)	Reference RSD (%)
run 1	68.3	**56.6**	1096.8	**5.1**
run 2	113.0	**77.3**	1206.0	**14.8**
run 3	66.7	**17.0**	880.2	**19.4**

D. 2.0 µm particles

	Device Avg (a.u.)	Device RSD (%)	Reference Avg (a.u.)	Reference RSD (%)
run 1	38.1	**38.7**	1237.1	**7.6**
run 2	55.3	**16.2**	1224.3	**4.6**
run 3	54.6	**18.7**	1366.9	**4.9**

E. 3.0 µm particles

	Device Avg (a.u.)	Device RSD (%)	Reference Avg (a.u.)	Reference RSD (%)
run 1	29.0	**17.4**	682.4	**10.1**
run 2	42.2	**26.1**	738.6	**1.6**
run 3	48.3	**51.7**	738.3	**0.7**

VITA

Tammi L. van Neel was born in Cape Town, South Africa and raised in California. She received her Bachelor of Science in Chemistry from Florida State University. While at Florida State University she participated in undergraduate research under the guidance of Dr. Michael Roper where she developed a love for (bio)analytical chemistry and method development. She continued her education by pursuing a doctoral degree at the University of Washington under the guidance of Dr. Ashleigh Theberge. While at UW, Tammi's research has focused on leveraging open microfluidic principles to develop user friendly biological platforms for tackling challenges in medicine and making translational technologies that enable unique studies. She achieved this by creating an environmental air sampling method to understand how personal exposures to harmful aerosols impacts health and developing a bead-based sampling approach to study cell signaling in cell culture model systems for understanding inflammation.